

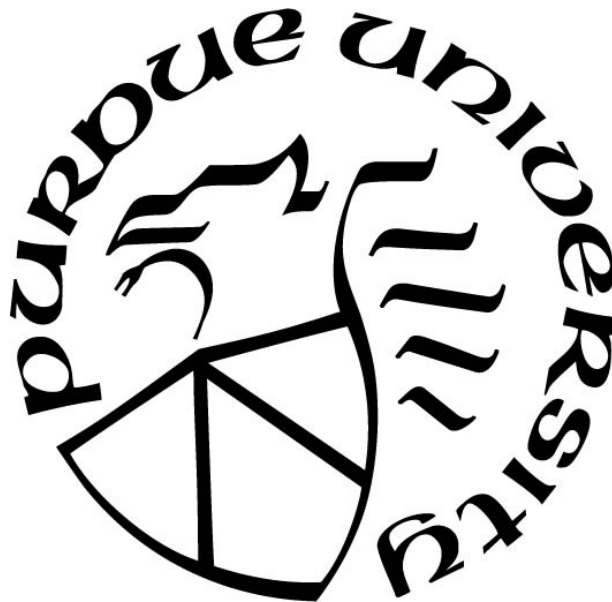
MULTI-PHYSICS MODELS TO SUPPORT THE DESIGN OF DYNAMIC WIRELESS POWER TRANSFER SYSTEMS

by
Anthony Agostino

A Thesis

*Submitted to the Faculty of Purdue University
In Partial Fulfillment of the Requirements for the degree of*

Master of Science in Electrical Engineering



School of Electrical and Computer Engineering
West Lafayette, Indiana
May 2022

THE PURDUE UNIVERSITY GRADUATE SCHOOL
STATEMENT OF COMMITTEE APPROVAL

Dr. Steven Pekarek, Chair

School of Electrical and Computer Engineering

Dr. Dionysios Aliprantis

School of Electrical and Computer Engineering

Dr. Konstantina Gkritza

School of Civil Engineering

Approved by:

Dr. Dimitrios Peroulis

Dedicated to my parents

ACKNOWLEDGMENTS

I would like to sincerely thank Dr. Steve Pekarek for advising me throughout the entirety of this research. I am very grateful for his guidance in formulating solutions to these research problems and for the knowledge I have gained from working with him.

I would also like to thank Dr. Dionysios Aliprantis for the many ideas he has contributed related to these efforts, and I would like to thank him and Dr. Nadia Gkritza for serving on my thesis committee.

I would also like to thank Dr. Aaron Brovont for his contributions to the DWPT system design and particularly for his work on the three-phase system.

Finally, I would like to thank my friends and family for their continuous encouragement during my time here.

TABLE OF CONTENTS

LIST OF TABLES	7
LIST OF FIGURES	10
ABSTRACT	13
1. Introduction.....	14
1.1 Literature Review.....	15
1.2 Thesis Outline	17
2. Component Models.....	18
2.1 Transmitter and Receiver Model	21
2.1.1 Core Volume and Mass Calculations	24
2.1.2 Inductance and Core Loss Models.....	26
2.1.3 Conductor Loss and Size Calculations	29
2.2 Compensation Circuit Inductor Model	31
2.2.1 Single-Turn Inductor Design	33
2.2.2 Multiple Turn Inductor Design.....	35
2.2.3 Inductor Fitness Calculations	37
2.2.4 Turns Comparison	39
2.2.5 Inductor Evaluation	43
2.3 Compensation Circuit Capacitor Metamodel.....	45
2.3.1 Previous Capacitor Types	45
2.3.2 Capacitor Arrangement Method	46
2.3.3 Custom Value Capacitors	50
2.3.4 Capacitor Thermal Performance.....	50
2.4 Power Electronics Models	52
2.4.1 Power Electronic Losses.....	53
2.4.2 Power Electronics Temperature.....	57
2.4.3 Power Electronic Mass and Volume.....	59
3. Transmitter Thermal Model.....	61
3.1 Transmitter Roadway Environment.....	63
3.2 Three-Phase Transmitter Model	68

3.2.1	Two-Dimensional Thermal Model	68
3.2.2	Three-Dimensional Thermal Model	71
3.2.3	Thermal Model Evaluation	74
3.3	Single-Phase Transmitter Model.....	79
3.3.1	Thermal Model Evaluation	82
3.4	Thermal Model Limitations	86
4.	Optimization Overview	88
4.1	Constraints	91
4.2	Optimization Studies.....	93
4.2.1	Core Material Comparison	95
4.2.2	Gap Distance Comparison	103
5.	System Validation.....	112
5.1	System Simulations.....	116
5.1.1	Full System Simulation.....	116
5.1.2	Isolated Transmitter and Receiver Simulation	119
5.1.3	Simulation of Transmitter and Receiver with Terminal Connections	121
5.1.4	Inductor Simulation	124
6.	Conclusion	128
	REFERENCES	129

LIST OF TABLES

Table 2.1: Single-Phase Transmitter and Receiver Geometric Variables.....	22
Table 2.2: Three-Phase Transmitter and Receiver Geometric Variables	23
Table 2.3: Core Material Densities	26
Table 2.4: Transmitter/Receiver Magnetic Parameters	29
Table 2.5: Toroidal Core Data	32
Table 2.6: Maximum Packing Factor Values	37
Table 2.7: Inductor Core Material Composition.....	38
Table 2.8: Inductor Core Loss Parameters.....	39
Table 2.9: Inductor Loss and Size Comparison	41
Table 2.10: Core Material Thermal Properties	42
Table 2.11: Litz Wire Thermal Properties	42
Table 2.12: Inductor Thermal FEA Results.....	42
Table 2.13: Sample Inductor Specifications	43
Table 2.14: Inductor Magnetic Validation Results	44
Table 2.15: Capacitor Bank Volume Comparison.....	46
Table 2.16: Capacitor Material Thermal Properties	51
Table 2.17: Capacitor Material Surface Properties.....	51
Table 2.18: Inverter Electrical Parameters.....	56
Table 2.19: Power Electronic Thermal Parameters	59
Table 2.20: Power Electronics Physical Parameters.....	60
Table 3.1: Cuboidal Element Label Descriptions	62
Table 3.2: Material Thermal Properties	64
Table 3.3: Thermal Model Boundary Properties	75
Table 3.4: Thermal Model Comparison and Validation for Concrete Roadway	77
Table 3.5: Thermal Model Comparison and Validation for Asphalt Roadway	79
Table 3.6: Concrete Roadway Thermal Model Comparison	84
Table 3.7: Asphalt Roadway Thermal Model Comparison	86

Table 4.1: Fitness Function Parameter Descriptions	89
Table 4.2: Fitness Metrics Weights	91
Table 4.3: Optimization Gene Ranges	94
Table 4.4: Material Comparison Sample Design Genes	100
Table 4.5: Sample Design Component Losses	101
Table 4.6: Sample Design Component Volumes	102
Table 4.7: Sample Design Compensation Circuit Values	102
Table 4.8: Sample Design Voltage and Current Ratings	103
Table 4.9: Gap Size Comparison Sample Design Genes	109
Table 4.10: Gap Size Comparison Component Losses	110
Table 4.11: Gap Size Comparison Component Volumes	110
Table 4.12: Gap Size Comparison Compensation Circuit Component Values	111
Table 4.13: Gap Size Comparison Voltage and Current Ratings	111
Table 5.1: Transmitter and Receiver Physical Design Parameters	113
Table 5.2: Capacitor Physical Layout Parameters	113
Table 5.3: Compensation Inductors Physical Parameters	115
Table 5.4: DWPT System Capacitance Matrices	118
Table 5.5: DWPT System Self-Inductance Matrices	118
Table 5.6: DWPT System Mutual Inductance Comparison	119
Table 5.7: Transmitter Self-Inductance Comparison	120
Table 5.8: Receiver Self-Inductance Comparison	121
Table 5.9: Mutual Inductance Comparison	121
Table 5.10: Effective Inductance Comparison	121
Table 5.11: Transmitter Self-Inductance Comparison with Connections	123
Table 5.12: Receiver Self-Inductance Comparison with Connections	123
Table 5.13: Mutual Inductance Comparison with Connections	123
Table 5.14: Effective Inductance Comparison	124
Table 5.15: Adjusted Compensation Circuit Component Values	124
Table 5.16: Compensation Inductor Inductance Matrices	125
Table 5.17: Effective Inductance Comparison	126

Table 5.18: Adjusted Inductance Matrices	126
Table 5.19: Adjusted Effective Inductance.....	127

LIST OF FIGURES

Figure 2.1: Single-Phase DWPT Circuit.....	18
Figure 2.2: Three-Phase DWPT Circuit.....	18
Figure 2.3: Single-Phase Transmitter and Receiver Geometry	21
Figure 2.4: Three-Phase Transmitter and Receiver Geometry	22
Figure 2.5: Single-Phase BEM Mesh.....	27
Figure 2.6: Three-Phase BEM Mesh	27
Figure 2.7: Toroidal Core Selection Chart [11]	32
Figure 2.8: AC Inductor Construction	33
Figure 2.9: Single-Turn Inductor Cross-Section.....	33
Figure 2.10: Single-Turn Inductor Flux Paths	34
Figure 2.11: Multiple Turn Inductor Cross-section	36
Figure 2.12: Pareto Fronts for 1 and 3 turn Inductors.....	40
Figure 2.13: 1 and 3 turn Sample Inductors.....	41
Figure 2.14: Sample Inductor Design 1 Flux Density	44
Figure 2.15: Capacitor Data [14]	45
Figure 2.16: Capacitor Type Volume Comparison.....	46
Figure 2.17: Capacitor Sub-group Layout	47
Figure 2.18: Capacitor Arrangement with Multiple Sub-groups	48
Figure 2.19: $C1$ and $Cf1$ Thermal Performance.....	52
Figure 2.20: Inverter Output under 180° Switching	52
Figure 2.21: Representation of Multiple Inverter Devices	53
Figure 2.22: Power Electronics Thermal Model [7]	57
Figure 3.1: TEC Cuboidal Element [16].....	61
Figure 3.2: Simplified TEC Cuboidal Element.....	62
Figure 3.3: TEC Structure.....	63
Figure 3.4: Transmitter Roadway Layout.....	64
Figure 3.5: TEC Material Homogenization [16].....	65

Figure 3.6: Expected Transmitter Duty Cycle	68
Figure 3.7: Two-Dimensional Transmitter Cuboidal Division	69
Figure 3.8: TEC Y-direction Cuboidal Division.....	69
Figure 3.9: TEC X-direction Cuboidal Division.....	70
Figure 3.10: Three-Dimensional Transmitter Sections.....	72
Figure 3.11: Transmitter Sections B and D Cuboidal Division	73
Figure 3.12: Transmitter Sections A and E Cuboidal Division	73
Figure 3.13: Transmitter Section F Cuboidal Division.....	74
Figure 3.14: FEA Results for Concrete Roadway under Standard Conditions.....	75
Figure 3.15: TEC Results for Concrete Roadway under Standard Conditions.....	75
Figure 3.16: FEA Results for Concrete Roadway under High Heat Conditions	76
Figure 3.17: TEC Results for Concrete Roadway under High Heat Conditions	76
Figure 3.18: FEA Results for Asphalt Roadway under Standard Conditions.....	77
Figure 3.19: TEC Results for Asphalt Roadway under Standard Conditions.....	78
Figure 3.20: FEA Results for Asphalt Roadway under High Heat Conditions	78
Figure 3.21: TEC Results for Asphalt Roadway under High Heat Conditions	78
Figure 3.22: Single-Phase Transmitter Cuboidal Distribution	79
Figure 3.23: Transmitter Sections.....	80
Figure 3.24: Sections B and D Cuboidal Distribution	81
Figure 3.25: Sections A and E Cuboidal Distribution	81
Figure 3.26: Section F Cuboidal Distribution.....	82
Figure 3.27: FEA Results for Concrete Roadway under Standard Conditions.....	83
Figure 3.28: TEC Results for Concrete Roadway under Standard Conditions.....	83
Figure 3.29: FEA Results for Concrete Roadway under High Heat Conditions	83
Figure 3.30: TEC Results for Concrete Roadway under High Heat Conditions	84
Figure 3.31: FEA Results for Asphalt Roadway under Standard Conditions.....	85
Figure 3.32: TEC Results for Asphalt Roadway under Standard Conditions.....	85
Figure 3.33: FEA Results for Asphalt Roadway under High Heat Conditions	85
Figure 3.34: TEC Results for Asphalt Roadway under High Heat Condition.....	86
Figure 4.1: System Optimization Fitness Function Overview	89

Figure 4.2: Core Material Comparison Pareto Fronts.....	95
Figure 4.3: Core Material Comparison Coupling Coefficient and System Efficiency	96
Figure 4.4: Core Material Comparison Receiver Footprint and Frequency	97
Figure 4.5: Core Material Comparison Compensation Circuit Volume	97
Figure 4.6: Core Material Comparison Winding Volumes.....	98
Figure 4.7: Sample Design with Magnetic Transmitter.....	99
Figure 4.8: Sample Design with Non-Magnetic Transmitter.....	99
Figure 4.9: Gap Size Comparison Pareto Fronts	104
Figure 4.10: Gap Size Comparison Coupling Coefficient and Efficiency.....	104
Figure 4.11: Gap Size Comparison Receiver Footprint and Frequency	105
Figure 4.12: Gap Size Comparison Compensation Circuit Volumes	106
Figure 4.13: Gap Size Comparison Winding Volumes	107
Figure 4.14: Sample Design with 18 cm Gap	108
Figure 4.15: Sample Design with 26 cm Gap	108
Figure 5.1: Transmitter and Receiver for System Validation	112
Figure 5.2: C_1 and C_{f1} Enclosure.....	114
Figure 5.3: C_2 and C_{f2} Enclosure.....	114
Figure 5.4: Prospective DWPT System Layout.....	115
Figure 5.5: Q3D Solution Settings.....	116
Figure 5.6: Q3D Model of Full System	117
Figure 5.7: Q3D Model of Isolated Transmitter and Receiver	119
Figure 5.8: Transmitter and Receiver End Turns.....	120
Figure 5.9: Q3D Model of Transmitter and Receiver with Terminals	122
Figure 5.10: Q3D Model of Compensation Inductors	125

ABSTRACT

Present barriers to electric vehicle (EV) adoption include cost and range anxiety. Dynamic wireless power transfer (DWPT) systems, which send energy from an in-road transmitter to a vehicle in motion, offer potential remedies to both issues. Specifically, they reduce the size and charging needs of the relatively expensive battery system by supplying the power required for vehicle motion and operation. Recently, Purdue researchers have been exploring the development of inductive DWPT systems for Class 8 and 9 trucks operating at highway speeds. This research has included the design of transmitter/receiver coils as well as compensation circuits and power electronics that are required to efficiently transmit 200 kW-level power across a large air gap.

In this thesis, a focus is on the derivation of electromagnetic and thermal models that are used to support the design and validation of DWPT systems. Specifically, electromagnetic models have been derived to predict the volume and loss of ferrite-based AC inductors and film capacitor used in compensation circuits. A thermal equivalent circuit of the transmitter has been derived to predict the expected coil and pavement temperatures in DWPT systems that utilize either single- or three-phase transmitter topologies. A description of these models, along with their validation using finite element-based simulation and their use in multi-objective optimization of DWPT systems is provided.

1. INTRODUCTION

As the desire to reduce carbon emissions becomes a greater worldwide priority, electric vehicle (EV) technology is growing as promising option to achieve this. Key benefits of EVs include higher efficiencies than traditional gas-powered vehicles and the ability to make use of clean, renewable energy sources, such as solar or wind. Further development and adoption of EVs would have a significant impact on supplanting the emissions caused by fossil fuel-burning vehicles, which makes up a substantial portion of global carbon emissions. However, there are still challenges that prevent EVs from being utilized to their fullest extent.

One deterrent to driving an EV is the limited battery capacity, which can severely limit the range one can drive. This is undesirable especially for highway transportation where there are large distances between charging stations. The high cost of large capacity batteries that are needed for EV's is also a concern for many, and it functions as a barrier to potential EV owners who cannot afford such an expense. In addition to energy capacity, the long recharge times for EV batteries is a significant inconvenience and another limiting factor in the widespread adoption of EVs.

Fortunately, research on dynamic wireless power transfer (DWPT) systems has been expanding notably in the past few years. DWPT allows for the charging of vehicles while in motion, which mitigates long charge times and battery capacity issues. Through a transmitter embedded in the roadway, enough power is supplied to the vehicle to maintain motion and additionally charge the onboard battery, which eliminates the need to stop to charge for extended periods of time and reduces the necessary battery size.

Much of the work in DWPT design has been focused on inductive power transfer (IPT) systems, in which coils in a transmitter transfer power by inducing currents in receiver coils that are placed on a vehicle. IPT systems can be classified into different topologies, and a broad distinction is made between single-phase and three-phase systems. In single-phase IPT systems, the currents in the transmitter coils operate in the same phase, whereas three-phase IPT systems feature three distinct transmitter coils with currents that are phase separated by 120° . A popular topology for single-phase systems is the double-d geometry, which has been considered in more detail in this and previous works.

Another characteristic of DWPT systems is a compensation circuit, which is appended to the transmitter and receiver to improve the efficiency of power transfer. Because the transmitter is

buried underneath pavement and the receiver is suspended from the underside of a moving vehicle, there is a rather large air gap between the coils, which results in weak magnetic coupling. If left unaddressed, it is infeasible to transfer large amounts of power across the gap; however, the compensation circuit solves this issue.

In order to design efficient and compact DWPT systems, multi-objective optimization approaches have been explored at the system level. At Purdue, continuing efforts have been made to develop comprehensive optimization-based design processes for DWPT systems that transfer 200 kW-level power. Primary objectives have been to minimize total loss and total volume of the system, which produces designs that have higher efficiencies and smaller volumes. The benefit of higher efficiency is apparent, although minimizing volume has multiple effects. Lower volume designs are less burdensome to implement in roadways and on vehicles, and volume additionally emulates the cost of the system to a certain degree.

To effectively design DWPT systems through the optimization process, reliable models for the loss and volume of all components are necessary. Models for the transmitter and receiver and the accompanying power electronic converters have been established through previous efforts. An emphasis in this work is deriving improved models for the compensation circuit inductors and capacitors for use in the system-level optimization. Thermal models of the transmitter are also developed and incorporated into the optimization to enforce temperature constraints upon potential designs.

Further evaluations of DWPT systems can be made through electromagnetic finite element-based simulations for all system components in a realistic setting. The stray inductances and capacitances of a proposed DWPT system can be examined, and attempts can be made to mitigate potential discrepancies between optimization models and the expected actualization of the system.

A review of previous developments in optimization based DWPT design is provided in the following subsection. The structure of the thesis is then outlined in subsection 1.2.

1.1 Literature Review

One earlier work in IPT optimization is presented in [1], wherein a single-phase rectangular transmitter and receiver were designed for stationary charging of public transportation vehicles. The system consisted of the transmitter and receiver, a series capacitor compensation circuit, and power electronic semiconductors. It was designed to transmit 50 kW at 85 kHz across a 16 cm air

gap, with three objectives considered in this optimization, namely power transfer efficiency, power density of the coils, and stray magnetic field. Thermal calculations of the coils were also developed to impose temperature constraints on designs. To calculate inductance and core loss, FEA calculations were utilized in the optimization, and validation of the models was provided through the construction of a prototype IPT system, which had a DC-DC efficiency of 95.8%. Lateral misalignment of coils was also assessed in the prototype system.

Multi-objective optimization was further developed for stationary IPT systems in [2]. Four distinct single-phase coil geometries were considered in the optimization, specifically circular, rectangular, double-d, and double-d quadrature. Capacitive compensation circuits and power electronics were incorporated into the system design, which was designed to transmit 7.2 kW at 85 kHz across a 20 cm air gap. A greater number of objectives were considered in this optimization, with the following four objectives employed: maximize system efficiency, maximize power density, minimize stray magnetic field, and maximize misalignment tolerance. 3D FEA simulations were integrated into this optimization to determine coil inductances and core losses. An IPT system with total efficiency of 93% was built as a prototype and used to validate the optimization models.

In [3], multi-objective optimization methods to design an isolated single-phase transmitter with double-d geometry were developed. The two objectives here were coupling coefficient and stray magnetic field. The receiver pad was determined for each transmitter design to reach the desired output power level, allowing coupling coefficient to be assessed with a focus on transmitter pad design. 3D FEA simulations were used to evaluate the inductances and magnetic flux within optimization, and designs from the optimization were constructed and examined in a lab to verify the models.

In [4], a focus was on optimizing the cost of the in-road DWPT components. In combination with a rectangular receiver, various single-phase transmitter shapes and grouping arrangements were considered, specifically elongated rails, lumped pads, and elongated pads. The considered DWPT system included compensation networks and multiple power electronic devices, and the loss and cost of all components were evaluated through a unique optimization algorithm. FEA models were implemented to determine inductances and core losses. The models were validated through the construction and testing of a 3.7 kVA DWPT system with 96% efficiency. Steps were also taken to assess effects of transmitter/receiver misalignment.

1.2 Thesis Outline

Chapter 2 begins with a discussion of the circuits used in the design of single- and three-phase DWPT systems. Models are provided to determine the power loss, volume, and mass of each component, which includes the transmitter and receiver, compensation circuit, and power electronics. Further discussion is presented on the development of the model for the AC inductors within the compensation circuit, which compares different inductor designs and validates analytical model through finite element analysis (FEA) simulations. The development of the capacitor model is also explained in detail.

Chapter 3 discusses the construction of a thermal model of the to evaluate peak conductor and peak road surface temperatures. The expected highway environment as well as transmitter operating conditions are first outlined. An approach that leverages thermal equivalent circuits is then detailed for the creation of models of both single- and three-phase transmitter geometries. The models are evaluated for different ambient conditions and roadway materials, and validation of the results is provided through FEA simulations.

Chapter 4 incorporates the models of the previous chapters into a system-level optimization and outlines the structure of the fitness function, including the genes used to define each design and the constraints that are imposed. Several optimization studies are performed to demonstrate the utility of the optimization method, comparing different core materials and different transmitter/receiver gap sizes. A detailed analysis of the study results is then presented to provide insight into the trade-offs of core material and gap size in DWPT systems.

In Chapter 5, the physical layout of a prospective three-phase DWPT system is described for a laboratory testing environment. Combined finite element/boundary element method simulations of the complete system are created to observe potential parasitic capacitances and inductances that might result from the proximity of different components. The isolated transmitter and receiver inductances are also validated. The added inductance of the connections between components is then addressed, and a technique to reduce added inductance in the compensation circuit inductors is discussed.

In the final chapter, the findings from previous sections are recounted, and the contributions to DWPT system optimization from this work are discussed. Potential areas for improvement and future research are also explored in this context.

2. COMPONENT MODELS

The following models are used to determine the fitness metrics for each component within the DWPT system. The circuit of the DWPT system is composed of the transmitter/receiver, compensation circuits, and power electronic converters, which is depicted in T-equivalent form for the single-phase topology in Fig. 2.1. The three-phase circuit is established in [5] and shown in Fig. 2.2. In the context of the optimization, the transmitter/receiver inductances are determined for each design, and the compensation circuit is designed based on those inductances using the method developed in [6].

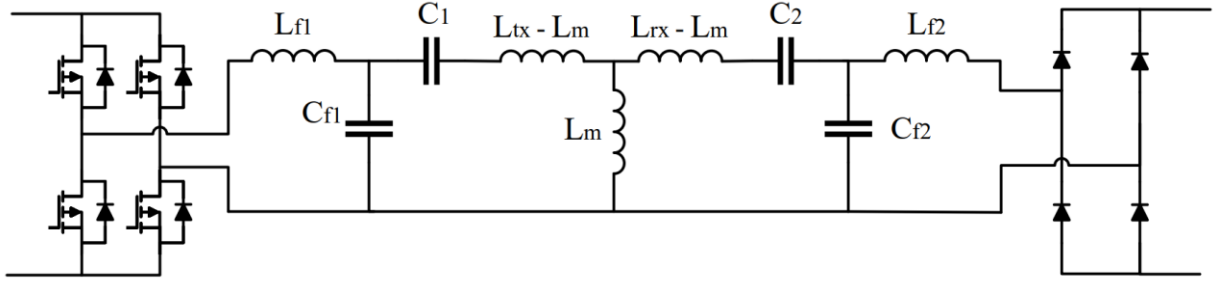


Figure 2.1: Single-Phase DWPT Circuit

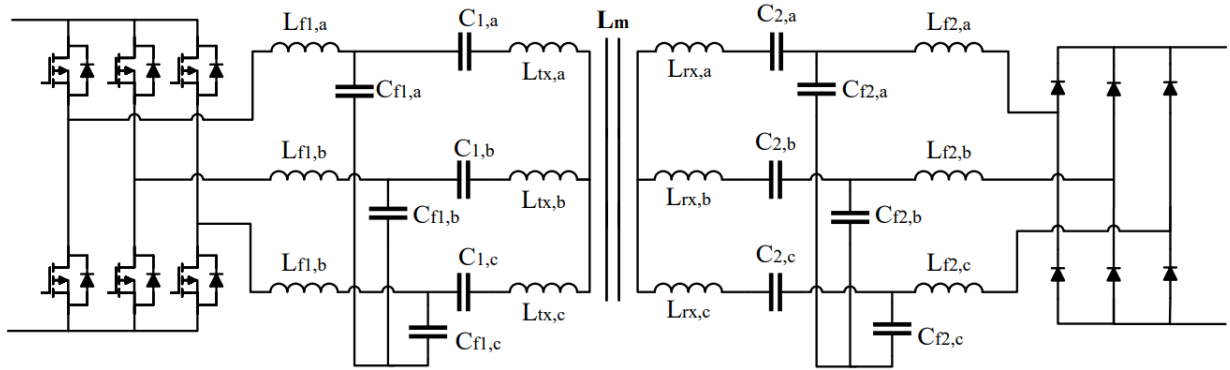


Figure 2.2: Three-Phase DWPT Circuit

To calculate the compensation circuit parameters, first the output power and input and output voltages are defined. The output power used in these calculations is dependent on the system topology, so the output power per phase $P_{out,ph}$ is used, which is defined as:

$$P_{out,ph} = \frac{P_{out}}{N_{ph}} \quad (2.1)$$

where P_{out} is the total output power, and N_{ph} is the number of phases in the system. The compensation circuit input voltage U_{AB} is the fundamental component of the AC inverter voltage, which is defined as:

$$U_{AB} = \frac{2\sqrt{2}}{\pi} V_{inv} \quad (2.2)$$

where V_{inv} is the DC inverter voltage. Similarly, the compensation circuit output voltage U_{ab} is the fundamental component of the AC rectifier voltage and is defined as:

$$U_{ab} = \frac{2\sqrt{2}}{\pi} V_{rec} \quad (2.3)$$

where V_{rec} is the DC rectifier voltage. The calculations for U_{AB} and U_{ab} assume that the AC voltages of the power electronics are square waves.

The compensation inductors are calculated first, with L_{f1} and L_{f2} defined as:

$$L_{f1} = \frac{U_{AB}}{I_{tx} \cdot \omega} \quad (2.4)$$

$$L_{f2} = \frac{U_{ab} \cdot I_{tx} \cdot L_m}{P_{out,ph}} \quad (2.5)$$

where I_{Tx} is the rms transmitter current. The values of the parallel connected capacitors C_{f1} and C_{f2} are then determined using the following expressions:

$$C_{f1} = \frac{I_{tx}}{U_{AB} \cdot \omega} \quad (2.6)$$

$$C_{f2} = \frac{P_{out,ph}}{\omega^2 \cdot U_{ab} \cdot I_{tx} \cdot L_m} \quad (2.7)$$

With those circuit parameters determined, the values of the remaining series connected capacitors C_1 and C_2 can be calculated by:

$$C_1 = \frac{1}{\omega^2 \cdot (L_{tx} - L_{f1})} \quad (2.8)$$

$$C_2 = \frac{1}{\omega^2 \cdot (L_{rx} - L_{f2})} \quad (2.9)$$

Because L_{tx} , L_{rx} , and L_m are each 3x3 inductance matrices in the three-phase system, a transformation is utilized to determine effective inductance values as defined by [5]. The effective inductances are calculated through a zero-sequence transformation, with transformation matrix A_{012} , where

$$A_{012} = \begin{bmatrix} 1 & 1 & 1 \\ 1 & e^{-\frac{j2\pi}{3}} & e^{\frac{j2\pi}{3}} \\ 1 & e^{\frac{j2\pi}{3}} & e^{-\frac{j2\pi}{3}} \end{bmatrix}$$

The zero-sequence inductance matrices are then calculated through the following matrix equation:

$$L_{012,i} = (A_{012})^{-1} L_{abc,i} A_{012} \quad (2.10)$$

for

$$i \in [tx, rx, m] \quad (2.11)$$

where $L_{abc,i}$ is the original inductance matrix with a, b, and c terms. The effective inductance terms are then calculated by averaging the 2nd and 3rd diagonal terms as in the following:

$$L_{eff,i} = \frac{1}{2} (L_{012,i}(2,2) + L_{012,i}(3,3)) \quad (2.12)$$

The three-phase compensation circuit values are then determined by (2.1)-(2.9) but with L_{tx} , L_{rx} , and L_m substituted for $L_{eff,tx}$, $L_{eff,rx}$, and $L_{eff,m}$. The transmitter and receiver are designed such that the inductances of each phase are symmetric to a certain degree, so the compensation circuit component values are uniform among each phase (i.e. $C_{1,a} = C_{1,b} = C_{1,c}$). The transformation essentially converts the three-phase circuit into a single-phase T-equivalent circuit as in Figure 2.1.

2.1 Transmitter and Receiver Model

The design of the transmitter and receiver is determined by a variety of geometric specifications for the core as well as the number of turns and size of conductors in the winding. Both single- and three-phase topologies are analyzed, which involve different sets of geometric parameters. Fig. 2.3 demonstrates the geometric parameters that define the single-phase transmitter and receiver, as established in [7], with Table 2.1 providing a description of each variable. It is noted that the receiver shape is slightly modified with tooth tips removed.

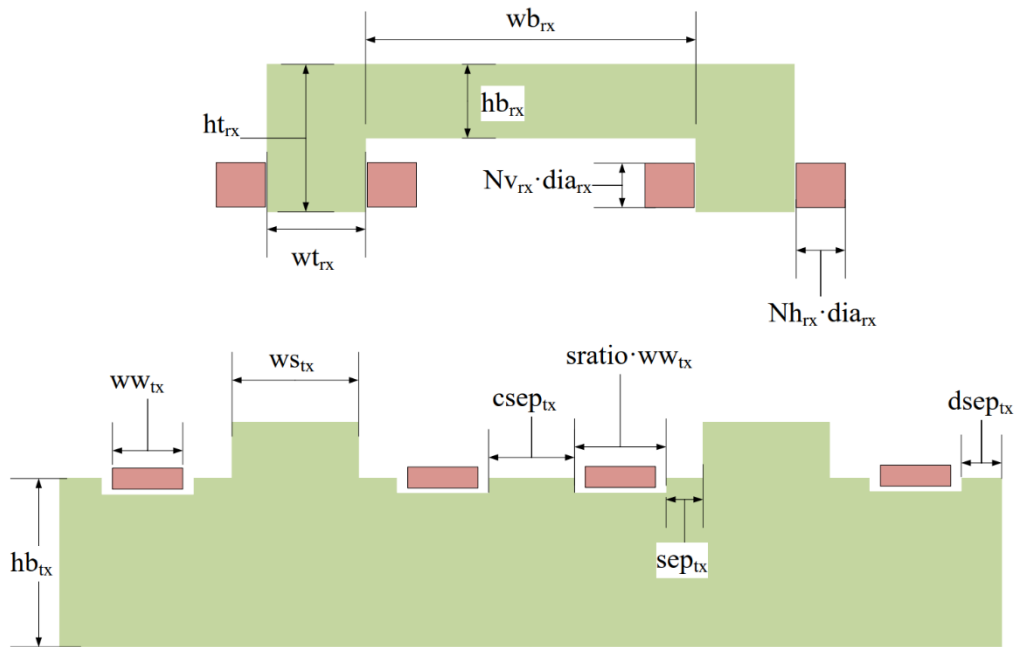


Figure 2.3: Single-Phase Transmitter and Receiver Geometry

The transmitter winding width ww_{tx} is not directly given as an input and is defined by multiple parameters:

$$ww_{tx} = N_{tx} \cdot dia_{tx} + (N_{tx} - 1) \cdot tsep_{tx} \quad (2.13)$$

Table 2.1: Single-Phase Transmitter and Receiver Geometric Variables

Variable	Description
hb_{tx}	Height of transmitter base
ws_{tx}	Width of transmitter stub
hs_{tx}	Height of transmitter stub
$sratio$	Ratio of transmitter slot width to winding width
sep_{tx}	Separation between winding slot and transmitter stub
$tsep_{tx}$	Separation between transmitter winding turns
$csep_{tx}$	Separation between center winding slots
$dsep_{tx}$	Separation between winding slot and transmitter end
dia_{tx}	Diameter of transmitter conductor
N_{tx}	Number of transmitter winding turns
wb_{rx}	Width of receiver base
hb_{rx}	Height of receiver base
wt_{rx}	Width of receiver tooth
ht_{rx}	Height of receiver tooth
dia_{rx}	Diameter of receiver conductor
Nh_{rx}	Number of horizontal receiver winding turns
Nv_{rx}	Number of vertical receiver winding turns

For the three-phase topology, the defining geometric assignments are depicted in Fig. 2.4 as established by [5], with variable descriptions included in Table 2.2.

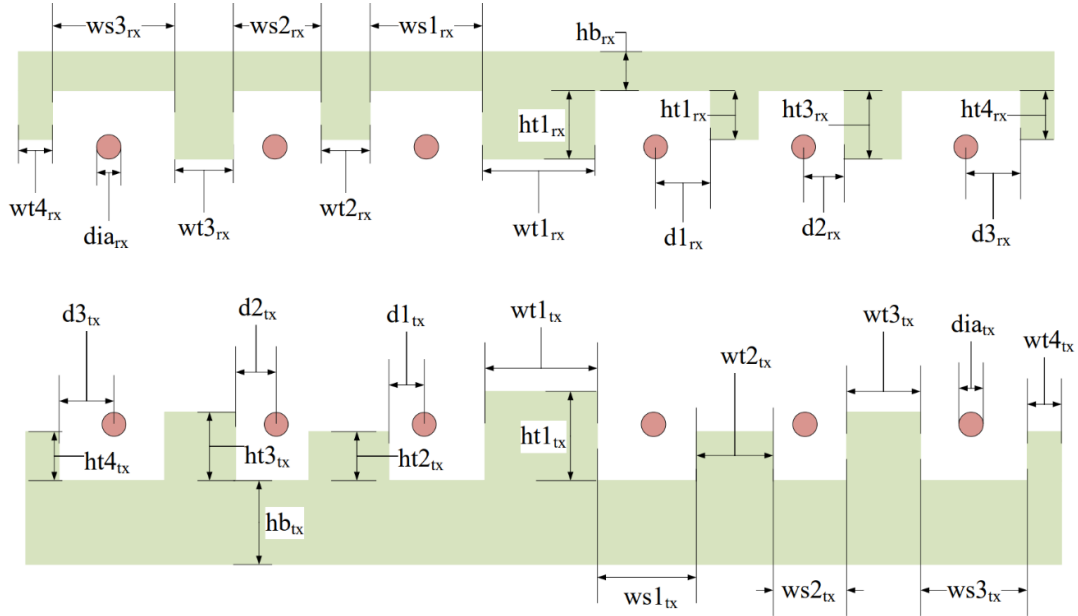


Figure 2.4: Three-Phase Transmitter and Receiver Geometry

Table 2.2: Three-Phase Transmitter and Receiver Geometric Variables

Variable	Description
hb_{tx}	Height of transmitter base
$wt1_{tx}$	Width of transmitter tooth 1
$wt2_{tx}$	Width of transmitter tooth 2
$wt3_{tx}$	Width of transmitter tooth 3
$wt4_{tx}$	Width of transmitter tooth 4
$ht1_{tx}$	Height of transmitter tooth 1
$ht2_{tx}$	Height of transmitter tooth 2
$ht3_{tx}$	Height of transmitter tooth 3
$ht4_{tx}$	Height of transmitter tooth 4
$ws1_{tx}$	Width of transmitter slot 1
$ws2_{tx}$	Width of transmitter slot 2
$ws3_{tx}$	Width of transmitter slot 3
$d1_{tx}$	Placement of conductor within slot 1
$d2_{tx}$	Placement of conductor within slot 2
$d3_{tx}$	Placement of conductor within slot 3
dia_{tx}	Diameter of transmitter conductor
hb_{rx}	Height of receiver base
$wt1_{rx}$	Width of receiver tooth 1
$wt2_{rx}$	Width of receiver tooth 2
$wt3_{rx}$	Width of receiver tooth 3
$wt4_{rx}$	Width of receiver tooth 4
$ht1_{rx}$	Height of receiver tooth 1
$ht2_{rx}$	Height of receiver tooth 2
$ht3_{rx}$	Height of receiver tooth 3
$ht4_{rx}$	Height of receiver tooth 4
$ws1_{rx}$	Width of receiver slot 1
$ws2_{rx}$	Width of receiver slot 2
$ws3_{rx}$	Width of receiver slot 3
$d1_{rx}$	Placement of conductor within slot 1
$d2_{rx}$	Placement of conductor within slot 2
$d3_{rx}$	Placement of conductor within slot 3
dia_{rx}	Diameter of receiver conductor

2.1.1 Core Volume and Mass Calculations

With the geometries of the transmitter and receiver defining the DWPT system design, the core volumes and masses can be directly determined without prior calculations. The widths of the cores are evaluated first, with the single-phase core widths $w_{tx,1ph}$ and $w_{rx,1ph}$ determined as:

$$w_{tx,1ph} = 4 \cdot (sratio \cdot ww_{tx} + sep_{tx}) + 2 \cdot (ws_{tx} + dsep_{tx}) + csep_{tx} \quad (2.14)$$

$$w_{rx,1ph} = wb_{rx} + 2 \cdot wt_{rx} \quad (2.15)$$

For the three-phase topology, the core widths $w_{tx,3ph}$ and $w_{rx,3ph}$ are calculated as:

$$w_{tx,3ph} = wt1_{tx} + \sum_{i=2}^4 2 \cdot wt(i)_{tx} + \sum_{i=1}^3 2 \cdot ws(i)_{tx} \quad (2.16)$$

$$w_{rx,3ph} = wt1_{rx} + \sum_{i=2}^4 2 \cdot wt(i)_{rx} + \sum_{i=1}^3 2 \cdot ws(i)_{rx} \quad (2.17)$$

The cross-sectional areas of the cores can then be calculated more easily. The single-phase areas $A_{tx,1ph}$ and $A_{rx,1ph}$ are calculated as:

$$A_{tx,1ph} = w_{tx} \cdot hb_{tx} + 2 \cdot ws_{tx} \cdot hs_{tx} - 2 \cdot sratio \cdot ww_{tx} \cdot dia_{tx} \quad (2.18)$$

$$A_{rx,1ph} = wb_{rx} \cdot hb_{rx} + 2 \cdot wt_{rx} \cdot ht_{rx} \quad (2.19)$$

and the three-phase core areas $A_{tx,3ph}$ and $A_{rx,3ph}$ are calculated as:

$$A_{tx,3ph} = wt1_{tx} \cdot ht1_{tx} + \sum_{i=2}^4 2 \cdot wt(i)_{tx} \cdot ht(i)_{tx} + w_{tx} \cdot hb_{tx} \quad (2.20)$$

$$A_{rx,3ph} = wt1_{rx} \cdot ht1_{rx} + \sum_{i=2}^4 2 \cdot wt(i)_{rx} \cdot ht(i)_{rx} + w_{rx} \cdot hb_{rx} \quad (2.21)$$

With the areas known, the volumes are simply calculated by multiplying those values by the lengths of each core l_{tx} and l_{rx} as in (2.22)-(2.25):

$$V_{C_{tx,1ph}} = A_{tx,1ph} \cdot l_{tx} \quad (2.22)$$

$$V_{C_{rx,1ph}} = A_{rx,1ph} \cdot l_{rx} \quad (2.23)$$

$$V_{C_{tx,3ph}} = A_{tx,3ph} \cdot l_{tx} \quad (2.24)$$

$$V_{C_{rx,3ph}} = A_{rx,3ph} \cdot l_{rx} \quad (2.25)$$

While l_{rx} is given as an input for each design, l_{tx} is set to a constant value, typically 12 ft. The masses are then calculated based on the core volumes and densities as in (2.26)-(2.29):

$$M_{C_{tx,1ph}} = V_{tx,1ph} \cdot \rho_{tx} \quad (2.26)$$

$$M_{C_{rx,1ph}} = V_{rx,1ph} \cdot \rho_{rx} \quad (2.27)$$

$$M_{C_{tx,3ph}} = V_{tx,3ph} \cdot \rho_{tx} \quad (2.28)$$

$$M_{C_{rx,3ph}} = V_{rx,3ph} \cdot \rho_{rx} \quad (2.29)$$

where ρ_{tx} and ρ_{rx} are the densities of the transmitter and receiver core materials. The considered materials in this DWPT system design are magnetized concrete Magment and MN80C ferrite, whose densities are listed in Table 2.3, with the values for Magment taken from [8].

Table 2.3: Core Material Densities

Material	Density $\left(\frac{kg}{m^3}\right)$
Magment	3750
Ferrite	4612

2.1.2 Inductance and Core Loss Models

To model the inductance and core loss of the transmitter and receiver, the boundary element method (BEM) presented in [9] is utilized. A key benefit of BEM for modeling the DWPT system is that non-magnetic materials do not need to be meshed, which eliminates computation time for the substantial air-gap between the transmitter and receiver. It is also not necessary to impose an external boundary, further improving the computational efficiency of this method. The BEM simulation evaluates integral expressions to create a model with the following form:

$$\mathbf{S} \begin{bmatrix} \mathbf{A}_z \\ \mathbf{B}_t \end{bmatrix} = \mathbf{J} \quad (2.30)$$

where \mathbf{A}_z is the magnetic vector potential, \mathbf{B}_t is the tangent flux density on the boundaries, and \mathbf{S} is an analog to the stiffness matrix from FEA methods. The vector \mathbf{J} is proportional to the current densities.

An example BEM mesh of the single-phase transmitter and receiver is shown in Fig. 2.5, and for the three-phase transmitter and receiver in Fig. 2.6. The surface meshes of the magnetic materials and the conductors are clearly outlined for both topologies.

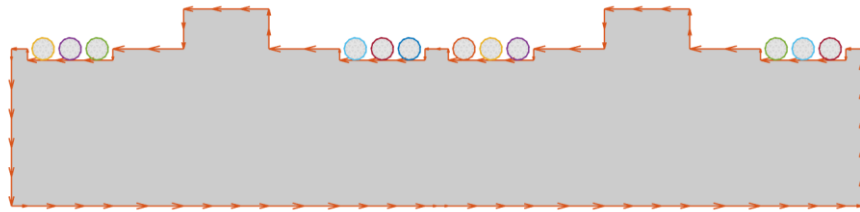


Figure 2.5: Single-Phase BEM Mesh

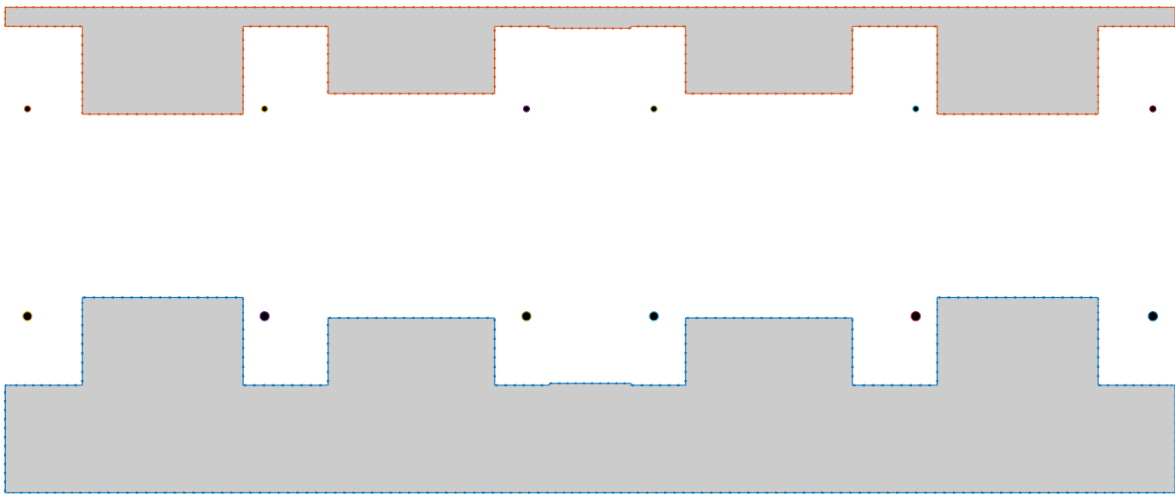


Figure 2.6: Three-Phase BEM Mesh

To determine the inductances, the fields are simulated through BEM for a current of 1 A in all conductors. Post-processing computations then determine the inductance values. For the single-phase system, the inductance matrix \mathbf{L}_{1ph} is returned:

$$\mathbf{L}_{1ph} = \begin{bmatrix} L_{tx,1} & L_{m,1} \\ L_{m,1} & L_{rx,1} \end{bmatrix}$$

The value of $L_{tx,1}$ is assigned to L_{tx} in the circuit of Fig. 2.1, $L_{rx,1}$ is assigned to L_{rx} , and $L_{m,1}$ is assigned to L_m .

For the three-phase geometry, a 6x6 matrix \mathbf{L}_{3ph} is returned:

$$\mathbf{L}_{3ph} = \begin{bmatrix} \mathbf{L}_{tx,3} & \mathbf{L}_{m,3}^T \\ \mathbf{L}_{m,3} & \mathbf{L}_{rx,3} \end{bmatrix}$$

where

$$\mathbf{L}_{tx,3} = \begin{bmatrix} L_{tx,a} & L_{tx,ab} & L_{tx,ac} \\ L_{tx,ab} & L_{tx,b} & L_{tx,bc} \\ L_{tx,ac} & L_{tx,bc} & L_{tx,c} \end{bmatrix}$$

$$\mathbf{L}_{rx,3} = \begin{bmatrix} L_{rx,a} & L_{rx,ab} & L_{rx,ac} \\ L_{rx,ab} & L_{rx,b} & L_{rx,bc} \\ L_{rx,ac} & L_{rx,bc} & L_{rx,c} \end{bmatrix}$$

$$\mathbf{L}_{m,3} = \begin{bmatrix} L_{m,a} & L_{m,ba} & L_{m,ca} \\ L_{m,ab} & L_{m,b} & L_{m,cb} \\ L_{m,ac} & L_{m,bc} & L_{m,c} \end{bmatrix}$$

The values of $L_{tx,a}$, $L_{tx,b}$, $L_{tx,c}$, $L_{rx,a}$, $L_{rx,b}$, and $L_{rx,c}$ correspond directly to the inductances noted in the circuit of Fig. 2.2, whereas \mathbf{L}_m in that circuit is a shorthand for all remaining mutual inductance terms. The transformation in (2.10)-(2.12) is performed on the matrices $\mathbf{L}_{tx,3}$, $\mathbf{L}_{rx,3}$, and $\mathbf{L}_{m,3}$ to produce the effective inductance terms that are used in (2.1)-(2.9).

With the transmitter/receiver inductances known, it is possible to calculate the values of the compensation circuit and therefore the currents in each component. To determine the core loss, the

BEM simulates the fields using the expected transmitter and receiver currents. The core loss is then computed using the modified Steinmetz form:

$$p_c = K_h \left(\frac{f}{f_b} \right)^\alpha \left(\frac{B_{pk}}{B_b} \right)^\beta \quad (2.31)$$

where p_c is the core loss density, B_{pk} is the peak flux density of a given element in the mesh, and f is the system frequency. The parameters K_h , α , β , f_b , and B_b are specific to the core material. For the considered core materials, Magment and MN80C ferrite, the magnetic parameters are listed in Table 2.4, which include the relative permeability and the core loss parameters.

Table 2.4: Transmitter/Receiver Magnetic Parameters

Parameter	Magment	Ferrite
μ_r	40	6377
$K_h \left(\frac{W}{m^3} \right)$	1794	21.80
α	1.10	1.01
β	2.95	2.70
$f_b (Hz)$	1	1
$B_b (T)$	1	1

2.1.3 Conductor Loss and Size Calculations

The single-phase conductor size and loss is calculated first. The transmitter winding length $lw_{tx,1ph}$ is calculated first, using the method in [7].

$$lw_{tx,1ph} = 2 \cdot \left(\sum_{k=1}^{N_{tx}} 2\pi(r_1 + (k-1)s_t) + 2N_{tx}(l_{tx} - 2h) \right) \quad (2.32)$$

where:

$$r_1 = 0.5 \cdot ws_{tx} + sep_{tx} + 0.5 \cdot dia_{tx} \quad (2.33)$$

$$s_t = tsep_{tx} + dia_{tx} \quad (2.34)$$

$$h = \sqrt{(0.5 \cdot ws_{tx} + sep_{tx})^2 - 0.5 \cdot ws_{tx}^2} \quad (2.35)$$

The volume can then be calculated as:

$$Vw_{tx,1ph} = \frac{\pi}{4} dia_{tx} \cdot lw_{tx,1ph} \quad (2.36)$$

The mass is then calculated as:

$$Mw_{tx,1ph} = mpm_{tx} \cdot lw_{tx,1ph} \quad (2.37)$$

where mpm_{tx} is the mass per meter of the Litz wire, taken from [10].

The resistance of the single-phase transmitter winding is then calculated as:

$$r_{tx,1ph} = rpm_{tx} \cdot lw_{tx} \quad (2.38)$$

where rpm_{tx} is the resistance per meter of the Litz wire, which is determined from [10]. Finally, the conduction loss can be calculated as:

$$Pw_{tx,1ph} = r_{tx,1ph} \cdot I_{tx}^2 \quad (2.39)$$

For the single-phase receiver, the volume of the winding is calculated first, using:

$$Vw_{rx,1ph} = (2(l_{rx} \cdot Nh_{rx} \cdot dia_{rx}) + 2(wt_{rx} \cdot Nh_{rx} \cdot dia_{rx}) + \pi(r_o^2 - r_i^2)) \cdot Nv_{rx} \cdot dia_{rx} \quad (2.40)$$

where:

$$r_o = r_i + Nh_{rx} \cdot dia_{rx} \quad (2.41)$$

and r_i is set to 0.001 m as the spacing between the receiver tooth and winding. The length of the receiver winding is determined by:

$$lw_{rx,1ph} = \frac{2 \cdot Vw_{rx,1ph}}{dia_{rx}^2} \quad (2.42)$$

The mass and resistance are calculated using (2.37) and (2.38).

For the three-phase topology, the same calculations are used for the transmitter and receiver winding size and loss. The length of the winding lw is calculated by:

$$lw_{i,3ph} = 2 \cdot \sum_{k=1}^3 l_i + wc_k - (4 - \pi)br_i \quad (2.43)$$

for

$$i \in [tx, rx] \quad (2.44)$$

where

$$br_i = 5 \cdot dia_i \quad (2.45)$$

and wc_k is the spacing between the conductors of each phase.

The conductor volume is then calculated with (2.36) and the winding mass with (2.37). The resistance and loss calculations are also repeated, with resistance calculated by (2.38) and conduction loss calculated by (2.39).

2.2 Compensation Circuit Inductor Model

For the compensation circuit inductors (L_{f1} , L_{f2}), the following AC inductor model determines the loss, mass, and volume of a selected inductor design given a desired inductance L_{des} , current I_L , wire radius r_w , and fundamental frequency of the system. The value of r_w is the same as in the transmitter/receiver winding, such that the wire is the same for L_{f1} and the transmitter, and the same for L_{f2} and the receiver. Toroidal ferrite-powder cores are used, which have relatively low losses and high saturation flux density. The ferrite-powder cores are also rated for frequencies up to 1 MHz, making them well-suited for this DWPT system. From a catalog of commercially available cores, appropriately sized cores can be selected using the chart in Fig. 2.7 which is taken from [11]. The term LI^2 , which is proportional to the energy in the core, is used to determine this, and a large range of cores are considered due to the varying current and inductance requirements. A section of the core data is shown in Table 2.5, which lists the LI^2 term, relative permeability, outer diameter OD , inner diameter ID , core length l_c , and core thickness t_c . It is noted that the value of LI^2 is typically an overestimate for any given inductor design since the inductors are composed of multiple cores.

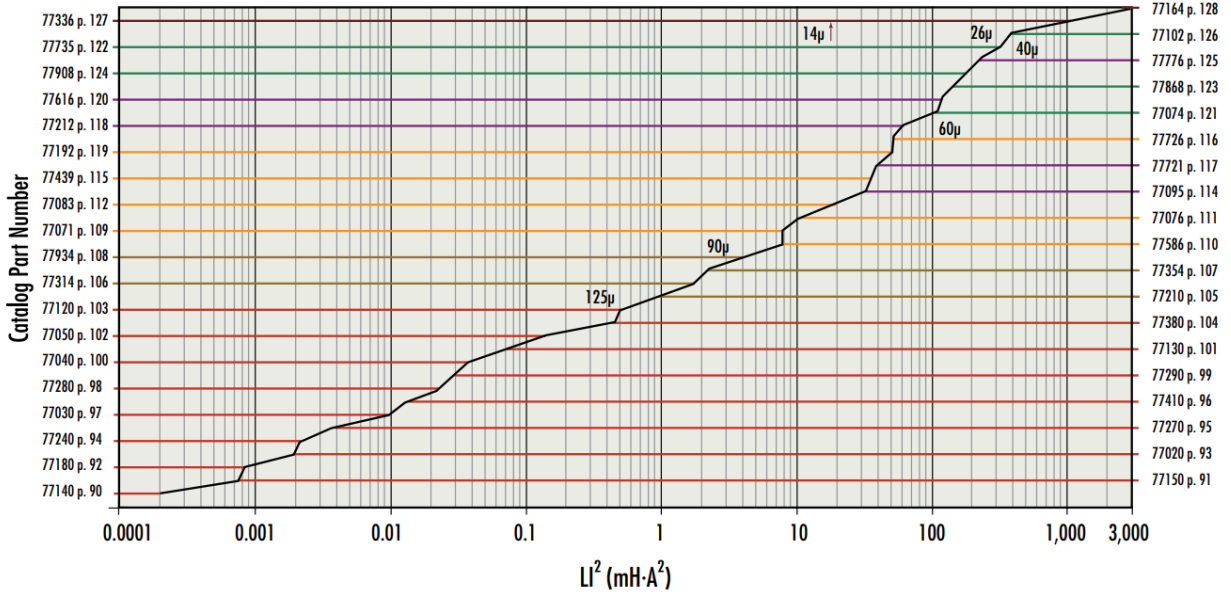


Figure 2.7: Toroidal Core Selection Chart [11]

Table 2.5: Toroidal Core Data

Part No.	$LI^2 \text{ (mH} \cdot \text{A}^2)$	μ_r	OD (mm)	ID (mm)	l_c (mm)	t_c (mm)
77071	7	60	32.79	20.09	10.67	6.35
77076	10	60	35.81	22.35	10.46	6.73
77083	20	60	39.88	24.13	14.48	7.88
77095	31	40	46.74	28.70	15.24	9.02
77439	35	60	46.74	24.13	18.03	11.31
77721	40	40	50.80	31.75	13.46	9.53
77192	50	60	57.15	26.39	15.24	15.38
77726	51	60	50.55	24.77	20.83	12.89
77212	60	40	57.15	35.56	13.97	10.80
77074	100	26	68.00	35.99	19.99	16.01
77616	110	40	61.98	32.59	24.99	14.70
77868	120	26	77.80	49.23	12.70	14.29
77908	150	26	77.80	49.23	15.88	14.29
77776	220	40	77.80	39.34	25.86	19.23
77735	300	26	74.09	45.29	35.00	14.40
77102	400	26	101.60	57.15	16.51	22.23

To construct the inductor core, a series of ferrite-powder toroidal cores are stacked, as depicted in Fig. 2.8, with l_c denoting the length of a single toroidal core, l_T denoting the total length of the stacked cores, and t_c denoting the thickness of the core. A single-turn inductor is

shown, but the model allows multiple turns of Litz wire, which can decrease the size of the component.

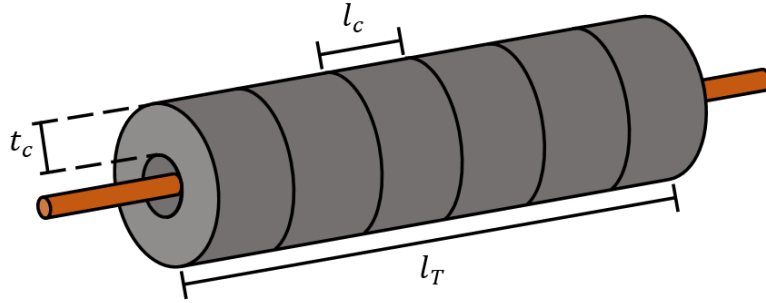


Figure 2.8: AC Inductor Construction

2.2.1 Single-Turn Inductor Design

To determine the appropriate size of the stacked cores, the inductance of an individual toroidal core segment, L_{sc} , is first calculated. The core magnetic and geometric properties, as depicted in Fig. 2.8 and Fig. 2.9, are taken from the core datasheet, while the wire diameter is taken from the model input.

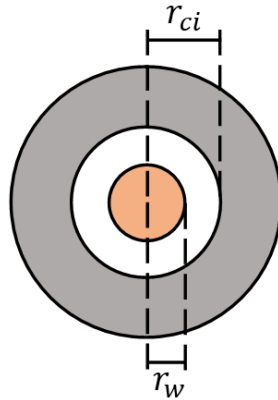


Figure 2.9: Single-Turn Inductor Cross-Section

Because the wire is only in the window of the core, it is assumed that there are two flux paths, designated in Fig. 2.10. The main flux Φ_c is contained in the core, with corresponding path permeance \mathcal{P}_c . The window flux Φ_w flows inside the window and wire, and the permeance of the window flux path is denoted \mathcal{P}_w .

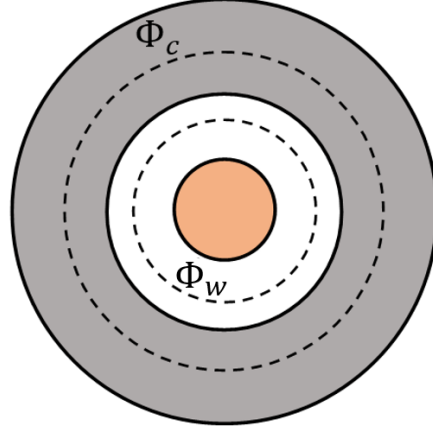


Figure 2.10: Single-Turn Inductor Flux Paths

Since most of the flux is in the core, \mathcal{P}_c is considered first. Utilizing techniques in [12], an expression for the permeance can be determined. To start, the relationship presented in (2.46) is considered:

$$\frac{1}{2} \mathcal{F}^2 \mathcal{P} = \frac{1}{2} \mu_0 \int H^2 dV \quad (2.46)$$

where V is volume, H is the magnetic field, and \mathcal{F} is the magnetomotive force. Accounting for the core geometry, the permeance of the core flux path is then determined by the following expression:

$$\mathcal{P}_c = \int_{r_{ci}}^{r_{co}} \frac{\mu_0 \mu_r l_c}{2\pi r} dr \quad (2.47)$$

where, based on the core datasheet, r_{ci} and r_{co} are specified as:

$$r_{ci} = \frac{ID}{2} \quad (2.48)$$

$$r_{co} = \frac{OD}{2} = r_{ci} + t_c \quad (2.49)$$

The integral from (2.47) is evaluated to:

$$\mathcal{P}_c = \frac{\mu_0 \mu_r l_c}{2\pi} \ln \left(1 + \frac{t_c}{r_{ci}} \right) \quad (2.50)$$

For the window permeance, the expression in (2.46) is rearranged for the core and conductor geometry, and \mathcal{P}_w can be calculated using the following expression:

$$\mathcal{P}_w = \mu_0 \left[\int_{r_w}^{r_{ci}} \frac{l_c}{2\pi r} dr + \int_0^{r_w} \frac{l_c r}{2\pi r_w^2} dr \right] \quad (2.51)$$

which is evaluated to:

$$\mathcal{P}_w = \frac{\mu_0 l_c}{2\pi} \left(\ln \left(\frac{r_{ci}}{r_w} \right) + \frac{1}{2} \right) \quad (2.52)$$

For the single-turn design, the inductance of one core segment, L_{sc} , can be calculated as:

$$L_{sc} = \mathcal{P}_c + \mathcal{P}_w \quad (2.53)$$

Stacking single cores increases the inductance, and to reach the desired inductance L_{des} , the total required core length l_T is determined using:

$$l_T = \frac{L_{des}}{L_{sc}} l_c \quad (2.54)$$

2.2.2 Multiple Turn Inductor Design

While the single turn design is slightly easier to analyze and construct, the design for inductors with multiple turns is also considered. The same steps are taken as previously discussed, but changes are made to the window permeance \mathcal{P}_w and single-core inductance L_{sc} . The multiple turns are simplified into the winding cross-section shown in Fig. 2.11, where r_w' denotes the combined winding bundle radius.

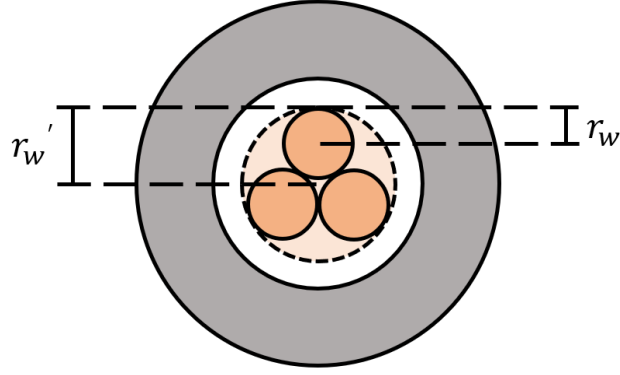


Figure 2.11: Multiple Turn Inductor Cross-section

For two and three turn designs, the calculations for $r'_w(N)$, where N is the number of turns, are shown below:

$$r'_w(2) = 2r_w \quad (2.55)$$

$$r'_w(3) = \left(1 + \frac{2}{\sqrt{3}}\right)r_w \quad (2.56)$$

As a result, the multi-turn \mathcal{P}_w is determined using the same expression as (2.52) but with r_w substituted for r'_w :

$$\mathcal{P}_w = \frac{\mu_0 l_c}{2\pi} \left(\ln \left(\frac{r_{ci}}{r'_w} \right) + \frac{1}{2} \right) \quad (2.57)$$

Although \mathcal{P}_w now accounts for additional turns, this expression only represents the permeance inside the core window, and with multiple turns, there are sections of the winding outside the core. One complication in accounting for this external leakage permeance is the minimum bend radius r_b of the Litz wire. As a general rule, r_b is ten times the wire radius r_w , which causes the turns to extend past the edge of the core. The resulting space between the core and the external winding result in additional leakage permeance that can vary greatly among designs. However, the leakage permeance is still relatively small compared to the core permeance, so it is ignored in this model.

To calculate the multi-turn L_{sc} , the following expression is used:

$$L_{sc} = N^2(\mathcal{P}_c + \mathcal{P}_w) \quad (2.58)$$

The necessary l_T to reach the desired inductance is still determined using (2.54), and it can be seen that using multiple turns can significantly reduce the inductor size.

2.2.3 Inductor Fitness Calculations

With the construction of the inductor defined for both the single-turn and multiple turn cases, the loss, volume, and mass can be calculated. For a given inductance L_{des} , current I_L , wire radius r_w , and frequency f , the full set of cores is evaluated, as listed in Table 2.5. The following process is used to determine the fitness metrics and chosen design:

1. Calculate L_{sc} and l_T for each core in the set using the previously described process.
2. Compute the packing factor k_{pf} within the core window. The window area A_w is calculated by:

$$A_w = \pi r_{ci}^2 \quad (2.59)$$

and k_{pf} is calculated by:

$$k_{pf} = \frac{N \pi r_w^2}{A_w} \quad (2.60)$$

If k_{pf} exceeds the maximum packing factor $k_{pf,max}$, as listed in Table 2.6, then that core is removed from consideration.

Table 2.6: Maximum Packing Factor Values

N	$k_{pf,max}$
1	1
2	0.5
3	0.646

3. Compute the maximum peak flux density $B_{pk,max}$, which is B_{pk} at the inner radius of the core, using:

$$B_{pk,max} = \frac{\mu_0 \mu_r N \sqrt{2} I_L}{2 \pi r_{ci}} \quad (2.61)$$

To ensure that magnetic saturation does not occur, the core is removed from consideration if $B_{pk,max}$ exceeds 80% of the saturation flux density, which is 1.5 T for this ferrite powder.

4. Calculate the length of the winding l_w by:

$$l_w = (2N - 1) l_T + 2(N - 1)\pi r_b \quad (2.62)$$

where r_b is the minimum bend radius of the Litz wire, estimated as:

$$r_b = 10 r_w \quad (2.63)$$

5. Calculate the core and winding volumes, V_c and V_w , by:

$$V_c = \pi t_c (2r_{ci} + t_c) l_T \quad (2.64)$$

$$V_w = \pi r_w^2 l_w \quad (2.65)$$

6. Calculate the core and winding masses, M_c and M_w , by:

$$M_c = \rho_c V_c \quad (2.66)$$

$$M_w = mpm_w l_w \quad (2.67)$$

where the density of the core material ρ_c can be inferred from its elemental composition, shown in Table 2.7, and mpm_w is the mass per meter of the Litz wire, which is taken from its datasheet [10].

Table 2.7: Inductor Core Material Composition

Element	Density $\left(\frac{kg}{m^3}\right)$	Percentage
Iron	7860	85%
Aluminum	2700	6%
Silicon	2330	9%

7. Calculate the resistive loss P_w by:

$$P_w = rpm_w l_w I_L^2 \quad (2.68)$$

where rpm_w is the resistance per meter of the Litz wire, which is taken from its datasheet.

8. Calculate the core loss P_c using the standard Steinmetz form:

$$P_c = K_h \left(\frac{f}{f_b} \right)^\alpha \left(\frac{B_{pk}}{B_b} \right)^\beta V_c \quad (2.69)$$

where B_{pk} is the average peak flux density in the core, f is the frequency, and K_h , α , and β are specified for the ferrite powder based on the relative permeability, as listed in Table 2.8. The base frequency f_b is 1 kHz, and the base flux density B_b is 1 T. The average B_{pk} in the core is calculated by:

$$B_{pk} = \frac{\sqrt{2} N I_L \mathcal{P}_c}{t_c l_{agg}} \quad (2.70)$$

The expressions for P_c and B_{pk} assume that I_L is sinusoidal.

Table 2.8: Inductor Core Loss Parameters

μ_r	$K_h \left(\frac{mW}{cm^3} \right)$	α	β
60	26.18	1.541	1.988
26, 40	32.22	1.541	1.988
14	80.55	1.541	1.988

9. Select the core that minimizes the P_w and P_c . The final inductor fitness metrics are those from the design with the minimum combined core and winding loss.

2.2.4 Turns Comparison

While using a multi-turn design can reduce the size of the compensation inductors, there can be complications with the assembly of the inductors and with uncontained magnetic radiation due to the external portions of the winding turns. Further observations of the trade-offs between single- and multi-turn inductor designs can be made by comparing the pareto-optimal fronts of genetic optimizations for the design of single-turn and three-turn inductors. With the volume and loss of the inductor as objectives, the genetic algorithm determines the best designs for the sample parameters $L_{sc} = 3.76 \mu H$, $I_L = 251 A$, and $f = 40 kHz$. The two genes were r_w and the core model number, ranging from 77212 to 77735 as noted in Table 2.5. As discussed earlier, constraints are imposed if the winding is too large for the core window or if the saturation flux density is exceeded.

It can be seen from the fronts, shown in Fig. 2.12, that single-turn inductors allow for slightly lower loss at the cost of a larger component relative to the three-turn inductors. It is noted that the gaps in the fronts are due to the different core model numbers, whose different geometries cause differences in the loss and volume of the inductors. While the observed trade-offs are not surprising, the loss density in the three-turn inductors might be a concern.

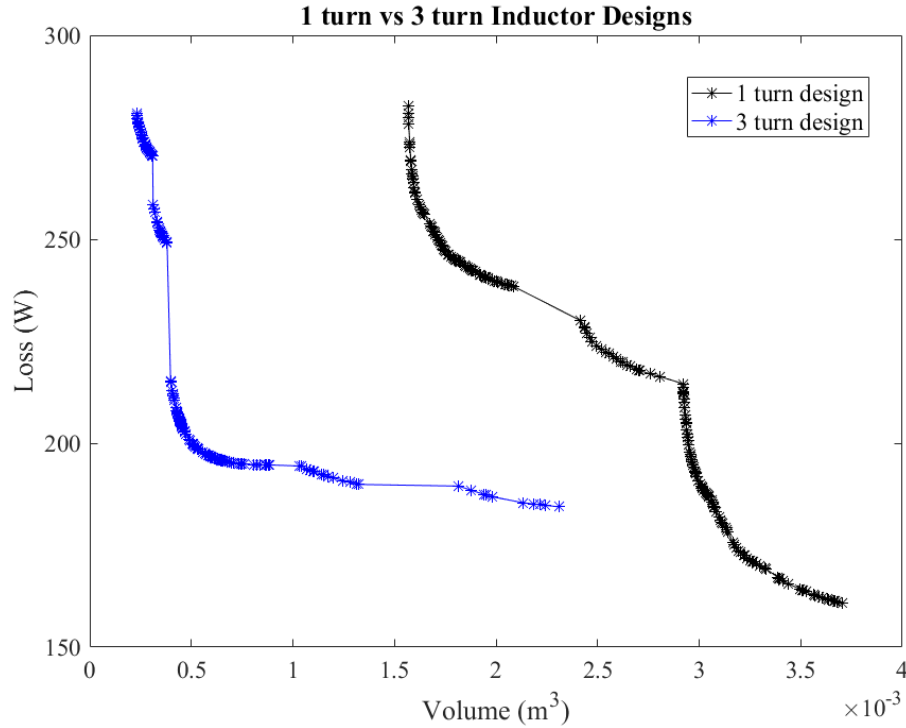


Figure 2.12: Pareto Fronts for 1 and 3 turn Inductors

The sizes and losses of designs with a similar loss are compared in Table 2.9, and it is seen that the volume of the three-turn inductor core is an order of magnitude lower than the single-turn inductor. The size disparity is also demonstrated in Fig. 2.13, showing both inductor constructions. Consequently, the loss density is an order of magnitude higher for the three-turn designs, so there are likely to be concerns related to overheating.

Table 2.9: Inductor Loss and Size Comparison

	1-turn Inductor	3-turn Inductor
$P_c (W)$	152.61	150.61
$V_c (m^3)$	2.88×10^{-3}	3.20×10^{-4}
$P_w (W)$	42.07	44.10
$V_w (m^3)$	8.93×10^{-5}	5.04×10^{-4}
$l_T (m)$	1.17	0.13



Figure 2.13: 1 and 3 turn Sample Inductors

To investigate the thermal performance of the both inductors, a steady-state thermal FEA in Ansys Workbench was created. The relevant material properties for the core are listed in Table 2.10, and to estimate the thermal properties of the ferrite powder, the previously mentioned elemental composition from Table 2.7 is used. The Litz wire properties, listed in Table 2.11, are anisotropic due to the structure of its many parallel strands, so a radial and longitudinal conductivity are shown. The process of determining the Litz wire properties is explained in Chapter 3.

Table 2.10: Core Material Thermal Properties

	Iron	Aluminum	Silicon	Core Estimate
Conductivity $\left(\frac{W}{m \cdot ^\circ C}\right)$	80	239	0.013	90
Heat capacity $\left(\frac{J}{kg \cdot ^\circ C}\right)$	450	890	700	505
Density $\left(\frac{kg}{m^3}\right)$	7680	2700	2330	6911

Table 2.11: Litz Wire Thermal Properties

	Litz Wire
Radial Conductivity $\left(\frac{W}{m \cdot ^\circ C}\right)$	0.09
Longitudinal Conductivity $\left(\frac{W}{m \cdot ^\circ C}\right)$	232
Heat capacity $\left(\frac{J}{kg \cdot ^\circ C}\right)$	403
Density $\left(\frac{kg}{m^3}\right)$	2798

As for the surface conditions, the core and Litz wire have a similar thin black plastic coating, so the same parameters were used for both. The convection coefficient was set to 5, which is representative of low airflow conditions, and emissivity was set to 0.95. The ambient temperature surrounding the inductor was assumed to be 22 °C.

The results of the thermal FEA are shown in Table 2.12, with the peak winding interior and core surface temperatures, T_w and T_c , shown. The winding temperatures in both cases are below the 155 °C temperature limit of the Litz wire, stated in [10]. However, the core temperature is significantly higher in the 3-turn inductor, exceeding 90 °C, which can be a concern depending on location of the DWPT system components.

Table 2.12: Inductor Thermal FEA Results

	1-turn Inductor	3-turn Inductor
T_w (°C)	54.93	30.07
T_c (°C)	31.98	91.17

Despite the more desirable operating temperature, the single-turn inductor is still much larger than the 3-turn one. However, the size is still relatively small compared to other system components, specifically the transmitter and receiver. Considering all these factors, the single-turn inductor design is much more feasible to incorporate into the DWPT system, and additional analysis can be done for the single-turn case.

2.2.5 Inductor Evaluation

To ensure that the core inductance and loss calculations are reasonable, a magnetic FEA simulation was created in Ansys Maxwell. Within Ansys, the eddy current solution type was used for a three-dimensional inductor model. As established in [13], the eddy current type solves the magnetic field H in the frequency domain through a $\vec{T} - \Omega$ formulation, and the flux density B is computed in post-processing. The insulating boundary type, which prevents flux from crossing the boundary, was imposed on the surface of a large surrounding cuboid. The boundary size was defined by 500% offset padding from the inductor in all directions. However, the winding must be extended to meet the boundary for this solution type, so there is additional inductance from the extra winding length. To account for this, a separate magnetic FEA of the extra winding was created using the same solution type and same size boundary, and that inductance was subtracted from the final value. Under these conditions, three sample single-turn inductor designs were evaluated, for which the specifications are listed in Table 2.13.

Table 2.13: Sample Inductor Specifications

Parameter	Design 1	Design 2	Design 3
$I_L \text{ rms (A)}$	251	283	265
$f \text{ (kHz)}$	40	30	50
μ_r	26	40	60
$r_{ci} \text{ (m)}$	1.80×10^{-2}	1.78×10^{-2}	1.24×10^{-2}
$t_c \text{ (m)}$	1.60×10^{-2}	1.08×10^{-2}	1.29×10^{-2}
$r_w \text{ (m)}$	4.74×10^{-3}	9.48×10^{-3}	4.74×10^{-3}
$l_T \text{ (m)}$	1.05	1.76	0.86

The distribution of the flux density B_{pk} can be seen in Fig. 2.14, in which the values refer to the peak B magnitude. As expected, the flux density is concentrated in the core, with a relatively low amount inside the core window. While B is not uniform in the core, as is assumed in the core

loss analysis, the spatial flux density average $B_{pk,avg}$ and core loss P_C are very similar to the values determined by the analytical model. These values are shown in Table 2.14, along with the flux density maximum $B_{pk,max}$ and inductance L as determined by both the presented model and the FEA. It is noted that while L and P_C are direct outputs in the FEA results, $B_{pk,max}$ is retrieved from the B_{pk} plots, and the value of $B_{pk,avg}$ is the spatial average attained from integrating B_{pk} over the core volume in the Ansys fields calculator. Compared to the FEA results, the presented model produces very similar values.

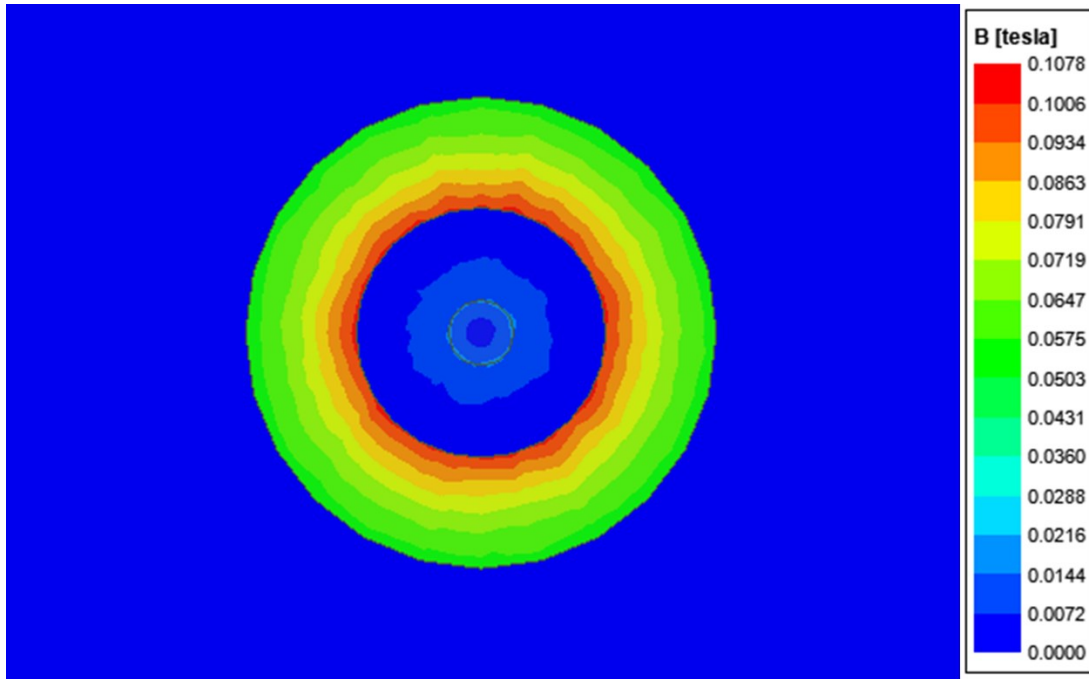


Figure 2.14: Sample Inductor Design 1 Flux Density

Table 2.14: Inductor Magnetic Validation Results

	Design 1		Design 2		Design 3	
	Model	FEA	Model	FEA	Model	FEA
L (μH)	3.859	3.746	7.078	7.102	7.613	7.548
$B_{pk,avg}$ (mT)	73.38	71.43	140.72	138.91	248.87	240.34
$B_{pk,max}$ (mT)	102.57	107.83	180.08	186.40	363.12	374.60
P_c (W)	144.61	137.62	750.19	728.25	405.51	384.38

2.3 Compensation Circuit Capacitor Metamodel

To determine the loss, mass, and volume of the compensation circuit capacitors, the following metamodel is used, based on high power polypropylene capacitors. These capacitors are designed to handle up to 400 kVAR at frequencies in the hundreds of kHz, making them well-suited for WPT applications. To ensure that the capacitors operate within their intended limits, it is assumed that multiple capacitors will be arranged in a bank such that the voltage and current limits are not exceeded in any individual capacitor. The limits and the standard capacitance values are attained from [14] and shown in Fig. 2.15. For the expected currents on the order of 100 A and peak voltages up to the order of 1 kV, it can be seen that a small number of capacitors will typically be needed to meet the current and voltage ratings.

Capacitance (±10%)	μF	0.1	0.2	0.33	0.66	1	1.33	2.6	5
Sinusoidal Voltage	Vrms	1000				800	900	700	500
Peak Voltage	Vpeak	1410				1130	1270	990	710
Max. Current	Arms	400		600		650	850	950	1000
Max. Power	kVAr	400							

Figure 2.15: Capacitor Data [14]

2.3.1 Previous Capacitor Types

For this WPT system, the capacitor metamodel was improved multiple times, using different capacitor types in each version. The most recent version was based on a smaller type of polypropylene capacitor but with lower current and voltage ratings. The highest current rating within the old set of capacitors was 22 A, with the voltage rating at 460 V. Although the old capacitors have a smaller volume than the current ones, the total capacitor bank size needs to be much larger to meet the current and voltage ratings. To demonstrate the size difference, the size of C_1 and C_{f1} banks for the same capacitance, voltage, and current specifications are shown in Fig. 2.16 for both the present and previous capacitor metamodels. The volumes of the capacitors are also listed in Table 2.15, where the old capacitors are 10 times larger than the present ones. It is clear that the updated capacitor type offers a significant volume improvement over the previous versions.

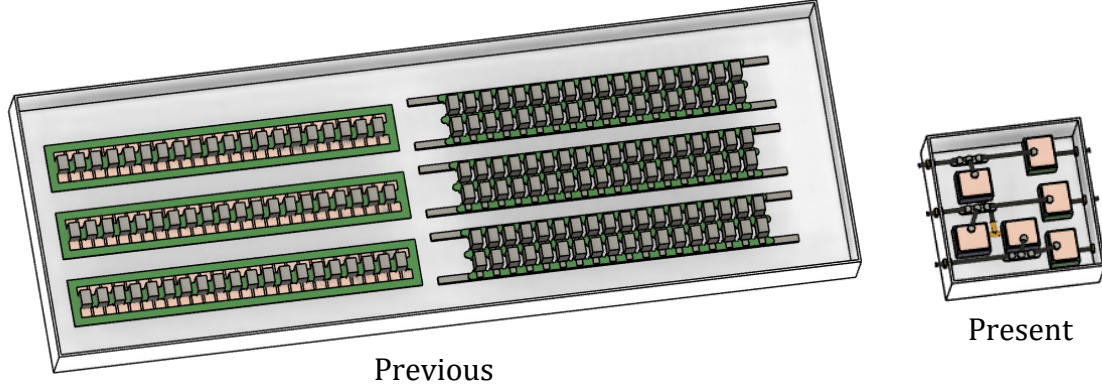


Figure 2.16: Capacitor Type Volume Comparison

Table 2.15: Capacitor Bank Volume Comparison

	Previous Style	Present Style
C_1 Volume (m^3)	2.88×10^{-3}	3.26×10^{-4}
C_{f1} Volume (m^3)	5.18×10^{-3}	3.26×10^{-4}
Total Volume (m^3)	8.05×10^{-3}	6.52×10^{-4}

2.3.2 Capacitor Arrangement Method

In order to achieve the desired capacitance, a variety of capacitor combinations are considered, and a configuration is determined that reaches the desired capacitance within a certain tolerance and meets the voltage and current ratings for each capacitor. While it would be relatively simple to only consider combinations using uniform capacitor values, this would typically increase the necessary number of capacitors greatly. Using a combination of different valued capacitors can keep the total amount small but introduces some complications due to the different current and voltage ratings.

To determine the arrangement of capacitors within the bank, a large set of potential capacitor value combinations is generated, and the equivalent capacitance C_{eq} of each arrangement is evaluated. To ensure that the voltage and current ratings are not exceeded, the minimum number of series $N_{s,mn}$ and minimum number of parallel $N_{p,mn}$ connections for each capacitance value are calculated as:

$$N_{s,mn}^{(i)} = \text{ceil} \left(\frac{V_C}{V_{R,i}} \right) \quad (2.71)$$

$$N_{p,mn}^{(i)} = \text{ceil} \left(\frac{I_C}{I_{R,i}} \right) \quad (2.72)$$

for

$$i \in \{1, 2, \dots, n_{cm}\} \quad (2.73)$$

where V_C refers to the total voltage across C_{eq} , and I_C refers to the total current through C_{eq} . The rated voltage $V_{R,i}$ and current $I_{R,i}$ refer to the ratings for capacitor C_i out of n_{cm} distinct capacitor models.

A subset of possible arrangements U is generated which contains arrangements of a uniform capacitor value C_i , such as the one in Fig. 2.17, such that there are at least $N_{s,mn}^{(i)}$ series and $N_{p,mn}^{(i)}$ parallel connections. The whole set of arrangements A is composed of the subset U and all unique parallel combinations of up to m arrangements in U . This combination of arrangements is depicted in Fig. 2.18, where $[u_1, u_2, \dots, u_m] \in U \in A$ and $a_j \in A$ with $j \in \{1, 2, \dots, n_A\}$ and n_A being the number of arrangements in A .

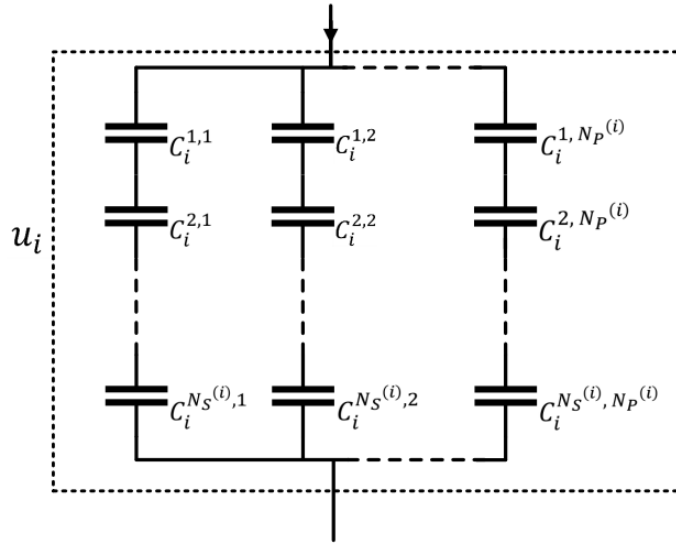


Figure 2.17: Capacitor Sub-group Layout

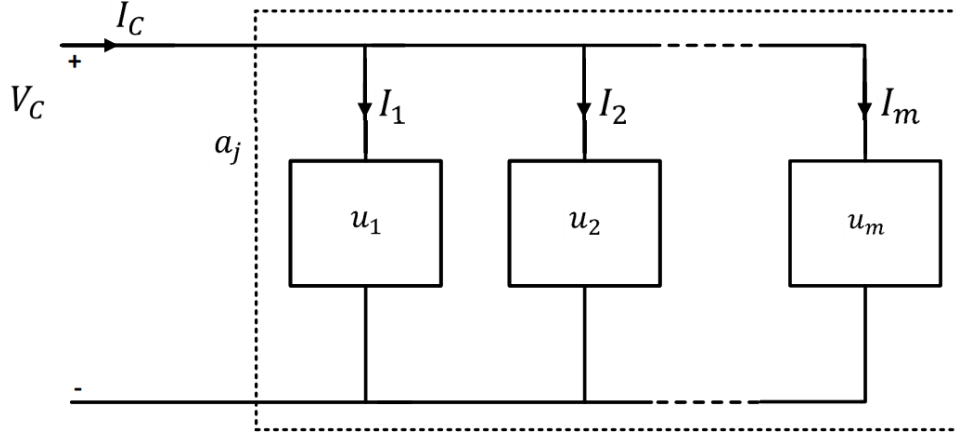


Figure 2.18: Capacitor Arrangement with Multiple Sub-groups

To select the best capacitor arrangement, the equivalent capacitance $C_{eq}^{(j)}$ for any arrangement a_j must be close to the desired capacitance C_{des} . A tolerance τ is used to control this, such that arrangements are filtered out of set A if the following condition is not met:

$$|C_{eq}^{(j)} - C_{des}| < \tau \quad (2.74)$$

Because the subgroups are connected in parallel, $C_{eq}^{(j)}$ is determined by:

$$C_{eq}^{(j)} = \sum_{i=1}^m \frac{N_p^{(i)}}{N_s^{(i)}} C_i \quad (2.75)$$

where a_j consists of the sub-arrangements u_1, u_2, \dots, u_m , and $N_s^{(i)}$ and $N_p^{(i)}$ are the number of series and parallel connections in sub-arrangement u_i .

After removing the arrangements that don't meet the tolerance condition in (2.74), the size of each remaining arrangement is determined. The total number of capacitors for each arrangement can be calculated by:

$$N_C^{(j)} = \sum_{i=1}^m N_s^{(i)} N_p^{(i)} \quad (2.76)$$

Since the mass and volume is the same for each capacitance, the mass and volume of the bank, M_C and Vol_C , only depend on N_C and physical dimensions listed in [14]. The total mass and volume are determined by:

$$M_C = N_C M_s \quad (2.77)$$

$$Vol_C = N_C h_s w_s l_s \quad (2.78)$$

where M_s is the mass a single capacitor, and the dimensions h_s , w_s , and l_s are the height, width, and length of one capacitor.

To estimate the loss of the capacitors, the manufacturer states that the general expected loss $P_{C,0}$ is dependent on the reactive power in the capacitor as follows:

$$P_{C,0} = V_C I_C \times 10^{-3} \quad (2.79)$$

This initial estimate includes both the losses in the capacitor and the connectors, and it is assumed to be primarily conduction loss. However, splitting the total current I_C into multiple parallel branches should reduce the total loss, which is not consistent with this initial loss estimate. An initial resistance estimate $R_{C,0}$ can be made from the initial loss assumptions as:

$$R_{C,0} = \frac{V_C \times 10^{-3}}{I_C} \quad (2.80)$$

The capacitor bank loss P_C is then determined by the sum of losses in each parallel sub-arrangement through the following:

$$P_C = \sum_{i=1}^m R_{C,0} \left(\frac{C_i I_C}{C_{eq}} \right)^2 \quad (2.81)$$

The equivalent series resistance R_C is then determined by:

$$R_C = \frac{P_C}{I_C^2} \quad (2.82)$$

The arrangement that meets the tolerance condition in (2.74) and minimizes P_C is selected as the final arrangement. The outputs of the metamodel are P_C , R_C , Vol_C , and M_C corresponding to that final arrangement.

2.3.3 Custom Value Capacitors

While the metamodel is intended to work with the standard capacitance values and ratings in Fig. 2.15, it is also possible to use custom capacitance values from the same manufacturer. This simplifies the process of determining the configuration, since it can simply be an array of $N_{s,mn}$ series connections by $N_{p,mn}$ parallel connections. In this case, $N_{s,mn}$ and $N_{p,mn}$ are based on the maximum current and voltage ratings from the standard set of capacitors. The custom capacitors have the same physical dimensions as the standard ones, so the mass and volume are calculated in the same way. The loss and resistance are also determined in the same way as in the standard value case.

2.3.4 Capacitor Thermal Performance

To ensure the capacitor design is physically reasonable, a sample capacitor configuration was evaluated through a steady-state thermal FEA simulation in Ansys Workbench. The proposed physical layout of the capacitors places the C_1 and C_{f1} capacitors together in one enclosure and the C_2 and C_{f2} capacitors together in another enclosure. The evaluated capacitor layout is a sample C_1 and C_{f1} enclosure, where it is assumed that the ambient temperature is 22 °C and there is minimal airflow inside the enclosure. For the sample design, the losses per each individual capacitor within C_1 and C_{f1} are 12.68 W and 9.34 W, respectively. The thermal properties of the capacitors are estimated based on those of copper and polypropylene, shown in Table 2.16, since the capacitors are primarily composed of those materials.

Table 2.16: Capacitor Material Thermal Properties

	Polypropylene	Copper	Capacitor Estimate
Conductivity $\left(\frac{W}{m \cdot ^\circ C}\right)$	0.22	385	192
Heat capacity $\left(\frac{J}{kg \cdot ^\circ C}\right)$	1920	390	1152
Density $\left(\frac{kg}{m^3}\right)$	950	8890	4955

The surface boundary parameters imposed on the capacitor and enclosure are shown in Table 2.17, in which the heat transfer coefficient defines a convection boundary, and the emissivity defines a radiation boundary in Ansys Workbench. Copper connection plates are included in the model, and the capacitor's surface is primarily copper, so the values for copper are used on the capacitor and connection surfaces. The enclosure is assumed to be steel, so the steel parameters are used for its surface. To account for the lack of airflow, the shown heat transfer coefficients are the values under still-air conditions.

Table 2.17: Capacitor Material Surface Properties

	Copper	Steel
Heat transfer coefficient $\left(\frac{W}{m^2}\right)$	13.14	25.32
Emissivity	0.07	0.96

The results of the FEA simulation of the sample layout are shown in Fig. 2.19, and it can be seen that the peak temperature reaches 60.496 °C. As stated in [14], the capacitors are rated up to 90 °C, so the proposed arrangement should allow the capacitors to operate safely. Importantly, this implies that the relatively small enclosure can still be used with the loss and number of capacitors predicted by the metamodel.

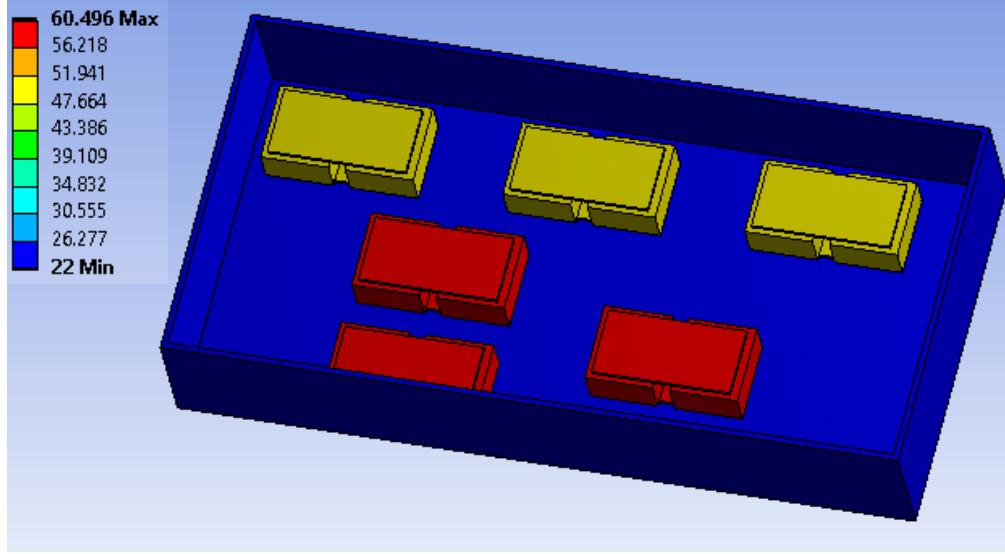


Figure 2.19: C_1 and C_{f1} Thermal Performance

2.4 Power Electronics Models

For the power electronics, models for the loss, volume, mass, and temperature of inverter and diode rectifier modules are utilized that are derived in [7]. While the values of loss, volume, and mass are directly included in the overall fitness, the temperature of the devices are also calculated to confirm that the operating temperature is below the manufacturer rated value. In this DWPT system, it is assumed that there is a 180° switching control scheme in the power electronics. The voltage waveform on the inverter output for this type of switching is shown in Fig. 2.20, where V_{inv} is the DC input voltage to the inverter.

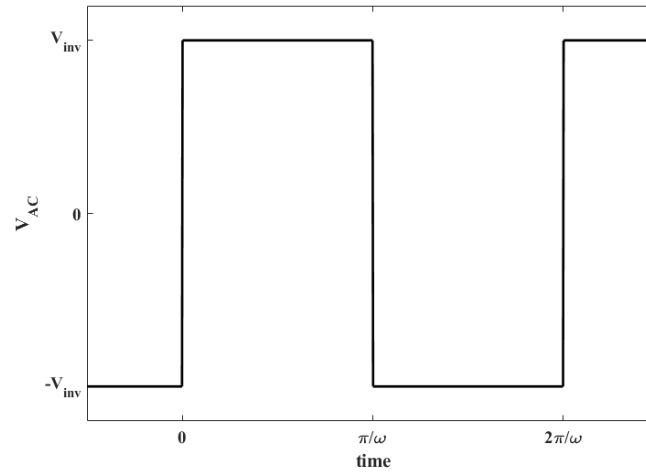


Figure 2.20: Inverter Output under 180° Switching

Under this operating condition, the loss, volume, and mass can be calculated through the methods in [7]. Derivations for both the switching loss and conduction loss are utilized here; however, the phase leg part is updated to the Wolfspeed CAB400M12XM3 module. Additionally, the model accounts for the use of multiple inverter devices. As shown in Fig. 2.21, each inverter phase leg in the system circuit diagrams represents N_{inv} parallel modules.

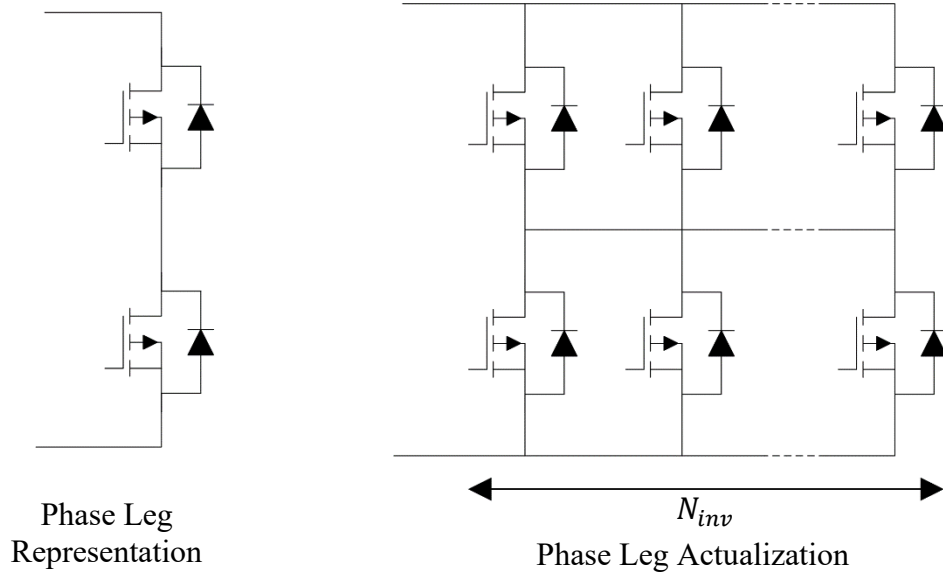


Figure 2.21: Representation of Multiple Inverter Devices

The inverter model receives the DC voltage V_{inv} , the output current I_{AC} , number of devices N_{inv} , switching frequency f_{sw} , fundamental frequency f_{AC} , and ambient temperature T_{Amb} . It is noted that with 180° switching, f_{sw} and f_{AC} are the same.

2.4.1 Power Electronic Losses

To calculate the inverter conduction loss, first the resistance of the inverter module is determined. Adding inverter devices in parallel has the obvious benefit of reducing resistance and conduction loss, and the drain to source transistor resistance R_{DS} and diode resistance R_d are calculated as:

$$R_{DS} = \frac{R_{DS,base}}{N_{inv}} \quad (2.83)$$

$$R_d = \frac{R_{d,base}}{N_{inv}} \quad (2.84)$$

where $R_{DS,base}$ and $R_{d,base}$ are the resistances for a single inverter module. Assuming sinusoidal current, the energy lost due to conduction is calculated over one period of the fundamental waveform. The conduction energy of upper and lower transistors and diodes of each phase leg, denoted $E_{C,Tu}$, $E_{C,Du}$, $E_{C,Tl}$, and $E_{C,Dl}$, are calculated distinctly. The conditions associated with different conduction energies define when conduction occurs in each component of the phase leg, and consequently, there is no conduction loss in a component if the corresponding condition is not met. When Tu is open and $I_{AC} > 0$, the upper switch energy $E_{C,Tu}$ is calculated by:

$$E_{C,Tu}^{(k)} = dt \cdot R_{DS} \cdot \left(I_{AC}^{(k)}\right)^2 \quad (2.85)$$

where dt is the time step, and k is the time step index. When Tu is open and $I_{AC} < 0$, the upper diode energy $E_{C,Du}$ is calculated by:

$$E_{C,Du}^{(k)} = dt \cdot \left(V_d \cdot |I_{AC}^{(k)}| + R_d \cdot \left(I_{AC}^{(k)}\right)^2 \right) \quad (2.86)$$

where V_d is the specified voltage drop across the diodes. The energy of the lower components is calculated similarly. When Tu is closed and $I_{AC} < 0$, the lower switch energy $E_{C,Tl}$ is calculated by:

$$E_{C,Tl}^{(k)} = dt \cdot R_{DS} \cdot \left(I_{AC}^{(k)}\right)^2 \quad (2.87)$$

Finally, when Tu is closed and $I_{AC} > 0$, the lower diode energy $E_{C,Dl}$ is calculated by:

$$E_{C,Dl}^{(k)} = dt \cdot \left(V_d \cdot I_{AC}^{(k)} + R_d \cdot \left(I_{AC}^{(k)}\right)^2 \right) \quad (2.88)$$

During the one period simulation, the switching loss is also calculated. By interpolating the test switching energy at the appropriate time steps, the upper and lower transistor switching energies, $E_{S,Tu}$ and $E_{S,Tl}$, can be calculated. When the upper transistor is switched on, $E_{S,Tu}$ is calculated by:

$$E_{S,Tu}^{(k)} = \text{interp1}(I_{test}, E_{on,test}, I_{AC}^{(k)}) \cdot \frac{V_{inv}}{V_{test}} \quad (2.89)$$

where *interp1* refers to a linear interpolation of the on-switching test energy $E_{on,test}$ against the test current I_{test} , and V_{test} is the switching test voltage. When upper transistor is turned off, $E_{S,Tu}$ is calculated by:

$$E_{S,Tu}^{(k)} = \text{interp1}(I_{test}, E_{off,test}, I_{AC}^{(k)}) \cdot \frac{V_{inv}}{V_{test}} \quad (2.90)$$

where $E_{off,test}$ is the off-switching test energy across the same I_{test} range. The same strategy is used for the lower transistors. When the lower transistor is switched on, $E_{S,Tl}$ is calculated by:

$$E_{S,Tl}^{(k)} = \text{interp1}(I_{test}, E_{on,test}, |I_{AC}^{(k)}|) \cdot \frac{V_{inv}}{V_{test}} \quad (2.91)$$

Finally, when lower transistor is turned off, $E_{S,Tl}$ is calculated by:

$$E_{S,Tl}^{(k)} = \text{interp1}(I_{test}, E_{off,test}, |I_{AC}^{(k)}|) \cdot \frac{V_{inv}}{V_{test}} \quad (2.92)$$

It is noted that the switching energy is only incident at the moment the switch status changes and not for the whole duration of any switch state.

With the conduction and switching energy defined at all times in the fundamental period, the RMS loss can be determined for each transistor and diode. The transistor and diode losses, P_{Tu} , P_{Tl} , P_{Du} , and P_{Dl} , are calculated using the following equations:

$$P_{Tu} = \sum_{k=1}^K (E_{C,Tu}^{(k)} + E_{S,Tu}^{(k)}) \cdot f_{AC} \quad (2.93)$$

$$P_{Du} = \sum_{k=1}^K \left(E_{C,Du}^{(k)} \right) \cdot f_{AC} \quad (2.94)$$

$$P_{Tl} = \sum_{k=1}^K \left(E_{C,Tl}^{(k)} + E_{S,Tl}^{(k)} \right) \cdot f_{AC} \quad (2.95)$$

$$P_{Dl} = \sum_{k=1}^K \left(E_{C,Dl}^{(k)} \right) \cdot f_{AC} \quad (2.96)$$

where K is total number of time steps. The total inverter loss P_{inv} is then determined by:

$$P_{inv} = N_{pl} \cdot (P_{Tu} + P_{Du} + P_{Tl} + P_{Dl}) \quad (2.97)$$

where N_{pl} is the number of phase legs in the inverter. Specifically, $N_{pl} = 2$ for the single-phase system, and $N_{pl} = 3$ for the three-phase system. The properties of the inverter modules used in (2.83) to (2.92) are shown in Table 2.5, as noted in [7].

Table 2.18: Inverter Electrical Parameters

Parameter	Value
$R_{DS,base}$	5.3 mΩ
$R_{d,base}$	6.7 mΩ
V_d	2.0 V
$E_{on,test}$	[0, 1.8, 4, 8] mJ
$E_{off,test}$	[0, 0.5, 4, 11] mJ
I_{test}	[0, 100, 400, 800] A
V_{test}	600 V

For the rectifier losses, the DWPT system assumes a passive diode rectifier, which is relatively simple to analyze compared to the inverter. Assuming 180° operation, the loss of one rectifier diode is calculated as:

$$P_D = V_d \cdot I_{AC} \cdot \frac{\sqrt{2}}{\pi} \quad (2.98)$$

where V_d is the voltage drop across the diode, specified as 1.5 V. The total loss of the inverter is then calculated by:

$$P_{rec} = N_{pl} \cdot N_{rec} \cdot P_D \quad (2.99)$$

2.4.2 Power Electronics Temperature

Based on the internal heat generation from the inverter losses, the temperature can be assessed to check that the inverter is operating within the manufacturer specified temperature range. A one-dimensional thermal model with multiple branches is developed in [7] to analyze the inverter and rectifier temperature, which is depicted in Fig. 2.22. This model is fully accurate for the inverter; however, for the rectifier, the model is simplified to only include the diode branches.

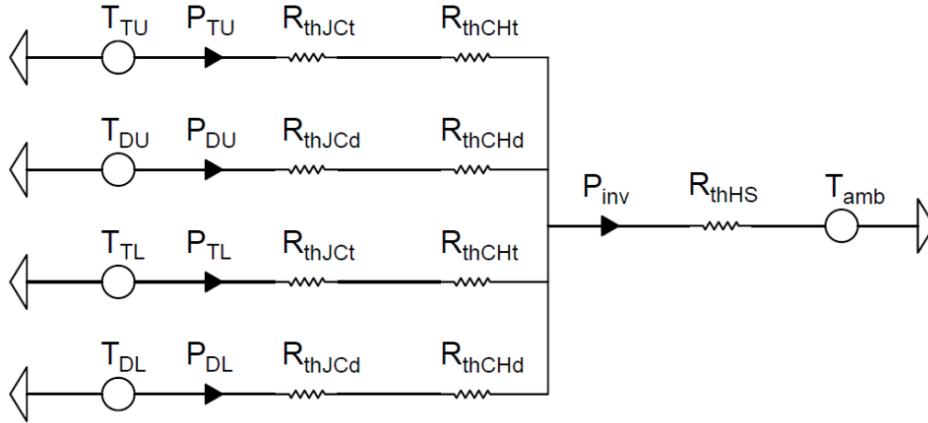


Figure 2.22: Power Electronics Thermal Model [7]

The heatsink temperature T_{HS} is first calculated as:

$$T_{HS} = P_{PE} \cdot \frac{R_{thHS,base}}{N_{PE}} + T_{Amb} \quad (2.100)$$

where the subscript PE refers to relevant power electronic converter, either the inverter or rectifier. $R_{thHS,base}$ is the base heatsink thermal resistance, which is scaled by the number of power electronic devices. The temperatures of the remaining branches are calculated through the following equations:

$$T_{Tu} = P_{Tu} \cdot \frac{R_{thJct,base} + R_{thCHt,base}}{N_{PE}} + T_{HS} \quad (2.101)$$

$$T_{Du} = P_{Du} \cdot \frac{R_{thJcd,base} + R_{thCHd,base}}{N_{PE}} + T_{HS} \quad (2.102)$$

$$T_{Tl} = P_{Tl} \cdot \frac{R_{thJct,base} + R_{thCHt,base}}{N_{PE}} + T_{HS} \quad (2.103)$$

$$T_{Dl} = P_{Dl} \cdot \frac{R_{thJcd,base} + R_{thCHd,base}}{N_{PE}} + T_{HS} \quad (2.104)$$

where $R_{thJct,base}$ and $R_{thJCHd,base}$ are the base transistor and diode thermal resistances from junction to case, and $R_{thJct,base}$ and $R_{thJCHd,base}$ are the base transistor and diode thermal resistances from case to heatsink. It is noted that for the rectifier, P_D is substituted for P_{Du} and P_{Dl} .

The peak junction temperatures of the inverter and rectifier are then determined by finding the maximum of all the branches:

$$T_{inv} = \max(T_{Tu}, T_{Du}, T_{Tl}, T_{Dl}) \quad (2.105)$$

$$T_{rec} = T_{Du} = T_{Dl} \quad (2.106)$$

The thermal resistances used in (2.100) to (2.104) are listed in Table 2.19a and Table 2.19b, which are retrieved from [15].

Table 2.19: Power Electronic Thermal Parameters

a) Inverter Properties

Parameter	Value
$R_{thHs,base}$	0.02 K/W
$R_{thJCt,base}$	0.15 K/W
$R_{thCHt,base}$	0.02 K/W
$R_{thJcd,base}$	0.15 K/W
$R_{thCHd,base}$	0.02 K/W

b) Rectifier Properties

Parameter	Value
$R_{thHs,base}$	0.01 K/W
$R_{thJcd,base}$	0.12 K/W
$R_{thCHd,base}$	0.02 K/W

2.4.3 Power Electronic Mass and Volume

When determining the sizes of the inverter and rectifier, the mass and volume of the converter modules is considered as well as for common mode chokes and an enclosure. The module mass and volume are taken from the datasheet and includes the heatsink, connectors, and converter components. The power module mass and volume, M_{pw} and Vol_{pw} , are calculated by:

$$M_{pw} = N_{pl} \cdot N_{inv} \cdot M_{pw,base} \quad (2.107)$$

$$Vol_{pw} = N_{pl} \cdot N_{inv} \cdot Vol_{pw,base} \quad (2.108)$$

where $M_{pw,base}$ and $Vol_{pw,base}$ are the mass and volume per phase leg module. The mass and volume of the chokes, M_{ch} and Vol_{ch} , are then calculated by:

$$M_{ch} = N_{pl} \cdot N_{inv} \cdot M_{ch,base} \cdot \frac{f_{base}}{f_{sw}} \quad (2.109)$$

$$Vol_{ch} = N_{pl} \cdot N_{inv} \cdot Vol_{ch,base} \cdot \frac{f_{base}}{f_{sw}} \quad (2.110)$$

where $M_{ch,base}$ and $Vol_{ch,base}$ are the base mass and volume of a single choke, and f_{base} is the corresponding base frequency. The total inverter mass and volume, M_{inv} and Vol_{inv} , are then estimated based on the sums of the power module and choke mass and volumes as follows:

$$M_{inv} = 1.7 \cdot (M_{pw} + M_{ch}) \quad (2.111)$$

$$Vol_{inv} = 1.33 \cdot (Vol_{pw} + Vol_{ch}) \quad (2.112)$$

These equations estimate the combined mass and volume of the power modules, chokes, and enclosure to provide complete values of the full inverter. The total rectifier mass and volume, M_{inv} and Vol_{inv} , are determined in the following equations:

$$M_{rec} = 1.7 \cdot M_{pw} \quad (2.113)$$

$$Vol_{rec} = 1.33 \cdot Vol_{pw} \quad (2.114)$$

which use the same estimation for the enclosure but do not include chokes. The physical parameter values used in (2.107)-(2.110) are listed in Table 2.20.

Table 2.20: Power Electronics Physical Parameters

Parameter	Value
$M_{pw,base}$	0.5 kg
$Vol_{pw,base}$	1066 cm ³
f_{base}	60 kHz
$M_{ch,base}$	1.0 kg
$Vol_{ch,base}$	853 cm ³

3. TRANSMITTER THERMAL MODEL

To assess the temperature in the pavement and transmitter winding, a thermal model of the roadway is developed using a thermal equivalent circuit (TEC). The layout of the transmitter roadway is divided into cuboidal elements, and a thermal resistance in each dimension is determined for each element. The TEC toolbox [16] is utilized to compute the TEC component values associated with each cuboid and to solve the temperatures at each node in the network of cuboids. The structure of a cuboidal element defined by the TEC toolbox is shown in Fig. 3.1, in which parameters are specified for the x, y, and z direction branches. Tables 3.1a and 3.1b list the description of each component in cuboid Ω .

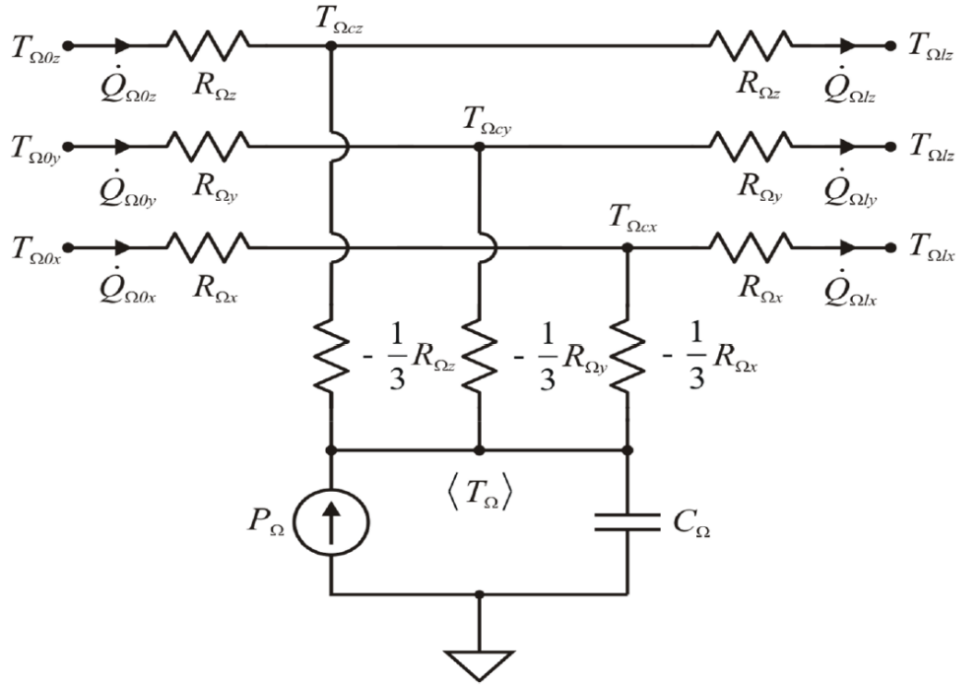


Figure 3.1: TEC Cuboidal Element [16]

Table 3.1: Cuboidal Element Label Descriptions

a) Component Descriptions		b) Subscript Description	
Component	Description	Subscript	Description
T	Temperature	$\mathbf{0}$	Initial node
Q	Heat flux	c	Center node
R	Thermal Resistance	l	End node
P	Dissipated Power		
C	Thermal Capacitance		

There are 4 unique temperatures and corresponding nodes associated with each cuboid, with 6 additional connection nodes. The mean temperature is denoted $\langle T_{\Omega} \rangle$. The initial and end nodes are shared between neighboring cuboids in a given direction. A simplified depiction of the TEC cuboidal element is shown in Fig. 3.2 for element Cub_i , where i is the index within the set of cuboidal elements. The nodes unique to each cuboid, N_{cx} , N_{cy} , N_{cz} , and N_m , denote the center nodes along the x, y, and z direction and the mean temperature node.

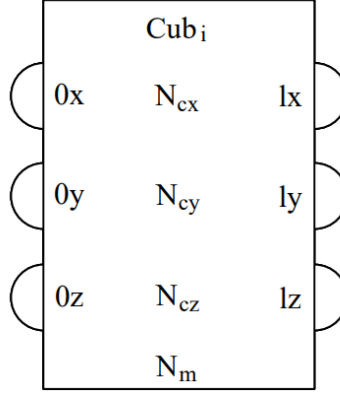


Figure 3.2: Simplified TEC Cuboidal Element

To demonstrate the TEC structure, a generic array of cuboidal elements is shown in Fig. 3.3. Within the transmitter TECs, the cuboids interface vertically such that ly of one cuboid connects to $0y$ of its above neighboring cuboid, and horizontally such that lx of one cuboid connects to $0x$ of its right neighboring cuboid. For cuboids on the edges of the array, an ambient temperature $T_{A,edge}$ is assigned to the edge nodes for the top, bottom, left, and right edges. It is not necessary to use the same ambient temperature for all cuboids on a common edge, and a unique

temperature value can be assigned to any combination of edge nodes. Additionally, while the generic TEC array is arranged in a grid, each column or row can contain any number of cuboids, and connection nodes can be shared among more than 2 neighboring cuboids. It is also noted that the z direction nodes are not shown in Fig. 3.3, but the principles of organizing the x and y direction nodes also apply to the z direction nodes.

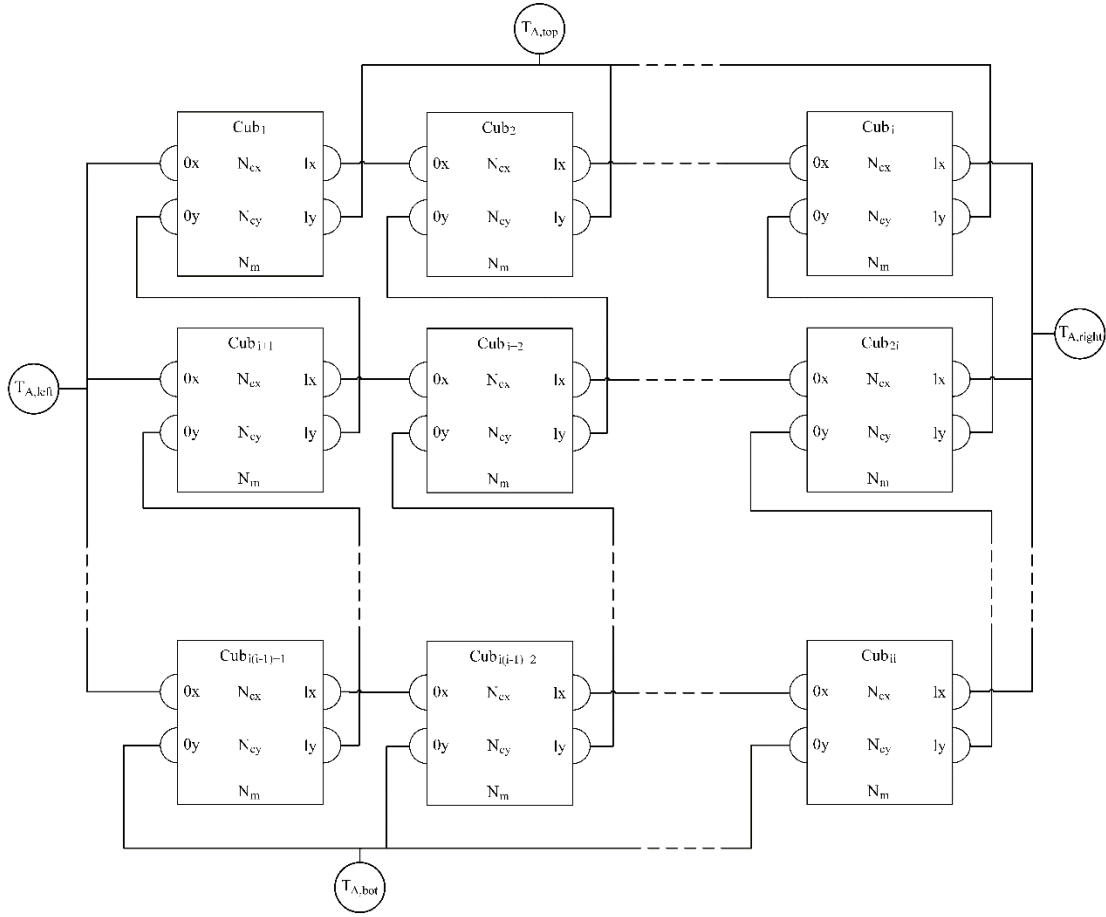


Figure 3.3: TEC Structure

3.1 Transmitter Roadway Environment

The roadway environment of the model includes the transmitter, the surrounding road material, and the underlying base and subbase materials, as depicted in Fig. 3.4. There is a 2-inch layer of pavement above the uppermost point of the core and winding, which is an estimate for the height of road removed during repaving. Both concrete and asphalt pavement are considered. Based on road building guidelines in [17], the base is a 3-inch thick layer of gravel, and the subbase is a 12-

inch thick layer of coarse crushed stone. In addition to the lane that contains the transmitter, the neighboring lane and shoulder are included, where it is assumed that the lane width is 12 feet and the shoulder width is 10 feet. For Fig. 3.4 and the following road cross-sections, the x-axis is defined from left to right, and the y-axis is defined from bottom to top. The terms width and length in this context refer to quantities in the x- and z-dimensions, respectively, whereas the terms height and thickness refer to quantities in the y-dimension.

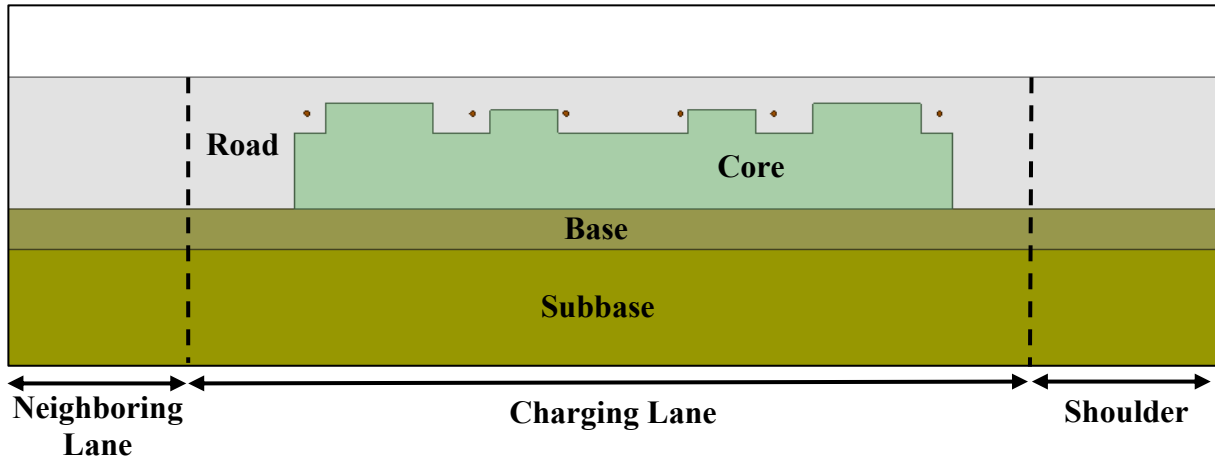


Figure 3.4: Transmitter Roadway Layout

For all materials in the model, the thermal properties are listed in Table 3.2. While the values for most materials can be retrieved from [18], the properties of the Litz wire are neither commonly known nor provided by the manufacturer.

Table 3.2: Material Thermal Properties

Material	Conductivity $\left(\frac{W}{m \cdot ^\circ C}\right)$	Heat capacity $\left(\frac{J}{kg \cdot ^\circ C}\right)$	Density $\left(\frac{kg}{m^3}\right)$
Concrete	1.40	840	2100
Asphalt	1.18	1040	2295
Magment	3.0	700	3750
Gravel	0.36	840	1840
Crushed stone	0.96	1000	1800
Nylon	0.25	1670	1150
Polyurethane	0.023	1590	24
FEP	0.21	1100	2150

To estimate the Litz wire thermal properties, the homogenizing function in [16] is used. The general homogenization process is depicted in Fig. 3.5, which shows the conversion of multiple conductors, insulation, and air/potting material into a homogenized material.

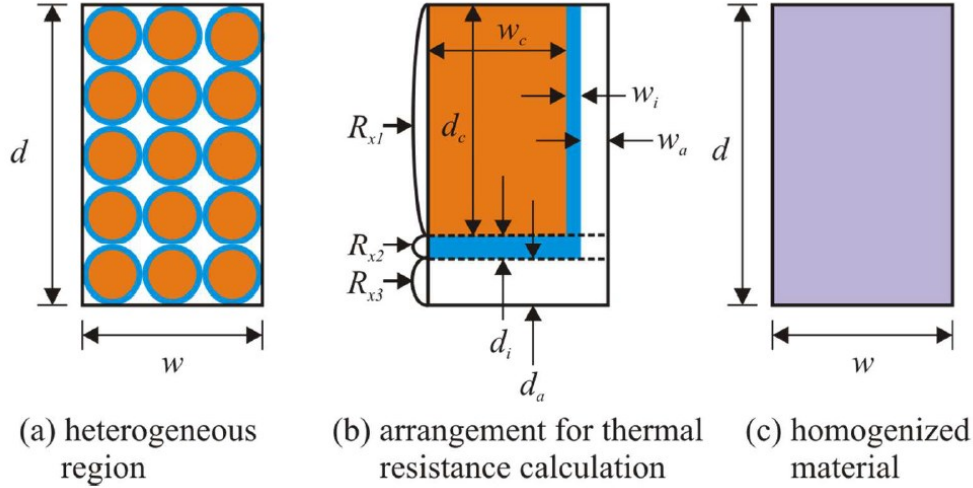


Figure 3.5: TEC Material Homogenization [16]

The total volume of each material is simplified to a rectangular cross-section, and then material properties are determined based on the rectangular sections. Due to the orientation of the conductor material, the winding block thermal conductivity is anisotropic, with identical values in the x- and y-directions. To determine the homogenized thermal conductivities $k_{h,xy}$ and $k_{h,z}$, the following equations are used:

$$k_{h,xy} = \frac{1}{\frac{1}{k_c} + \frac{d_i}{k_c + d_c} + \frac{d_a}{k_a \cdot d_c}} + \frac{1}{\frac{d_c + d_i}{k_i \cdot d_i} + \frac{d_a}{k_a \cdot d_i}} + \frac{1}{\frac{d}{k_a \cdot d_a}} \quad (3.1)$$

$$k_{z,h} = \frac{a_c \cdot k_c + a_i \cdot k_i + a_a \cdot k_a}{w \cdot d} \quad (3.2)$$

where k refers to the thermal conductivities and a refers to the area of the conductor, insulation, and potting/air material, denoted with subscripts c , i , and a respectively. The dimensions w and d are specified in Fig. 3.5. The homogenized density ρ_h is then determined through (3.3):

$$\rho_h = \frac{a_c \cdot \rho_c + a_i \cdot \rho_i + a_a \cdot \rho_a}{w \cdot d} \quad (3.3)$$

where ρ refers to the density of each material.

To estimate the properties of the winding block in the transmitter, the homogenization process is employed in two steps:

1. The Litz wire is homogenized based on the number of copper strands, taken from [10], with nylon insulation around each strand and polyurethane filler.
2. The winding block is homogenized based on the number of Litz wire turns with FEP insulation and the road material as the filler.

This results in a unique set of thermal properties for the winding material given the wire gauge and number of turns.

On the boundary of the model, the thermal circuit assigns appropriate ambient temperatures at various surfaces. The bottom of the subbase layer is set to an ambient ground temperature of 16°C, which is assumed to be relatively constant throughout the year. For the ambient air temperature, a layer of air is included above the road surface, and the air temperature is assigned to the top of the air cuboids. There are two cases considered for the ambient air temperature: a standard case and a high heat case. The standard case sets the air temperature to 22°C and represents average environmental conditions, while the high heat case is meant to represent the hottest roadway conditions that could be seen in the summer, where the surface of the road can reach up to 60°C. The air temperature is set to 40°C and heat flux is included at the surface of the road to account for solar radiation. The amount of heat flux is determined independently for the different transmitter topologies such that the surface reaches approximately 60°C when the transmitter is off. For the remaining boundaries along the right edge of the shoulder and left edge of the neighboring lane, the ambient temperatures are set to the average of the air and ground temperatures.

It is worth noting some concerns over the high heat case, primarily that some pavements may become deformed and curled under the assumed high temperatures. Additionally, despite the similar temperature levels, the differing amounts of solar radiation imply different environmental conditions among the model variations. While these factors may introduce some uncertainty in the

model, the high heat conditions are meant to provide insight into the worst-case, and the results still provide value as a precautionary metric.

A final consideration of the roadway layout is the expected transmitter duty cycle. The transmitter is intended to be controlled where it operates only in the presence of a vehicle equipped with a receiver, which means the power loss won't be constant, and a duty cycle and average power dissipation can be estimated to model the expected steady-state performance. To determine the average power dissipation, first the peak power transfer time t_{on} is determined by the following equation:

$$t_{on} = \frac{l_{tx} + l_{rx}}{v} \quad (3.4)$$

where l_{rx} is the length of the receiver, l_{tx} is the total length of a transmitter segment group, and v is the vehicle speed. The vehicle speed is assumed to be 60 mph, or 26.82 m/s. The length of a group of transmitter segments is used because the transmitters are intended to be organized consecutively into groups of five. All the transmitter segments in a group are powered by the same inverter and have the same controls, meaning the whole group will be turned on if the receiver is sensed over any portion of it.

To estimate the total time period T_{tx} , the following equation is used:

$$T_{tx} = \frac{l_v}{v} + \frac{t_{sp}}{2} \quad (3.5)$$

where l_v is the average vehicle length, assumed to be 70 feet, or 21.34 meters, and t_{sp} is a spacing time based on recommendations for safe vehicle spacing. t_{sp} is defined as an added second of spacing for every 10 feet of vehicle length; however, because this is just a guideline for drivers, the added time is halved to be a more realistic estimate. No rise or fall times are considered since the transmitter power loss will occur as soon as it is turned on. The expected transmitter duty cycle is shown in Fig. 3.6, where P_{tx} is the combined rms winding and core loss in the transmitter during continuous operation. The duty cycle d is calculated by:

$$d = \frac{t_{on}}{T_{tx}} \quad (3.6)$$

The average power dissipation P_{avg} is then determined by:

$$P_{avg} = d \cdot P_{tx} \quad (3.7)$$

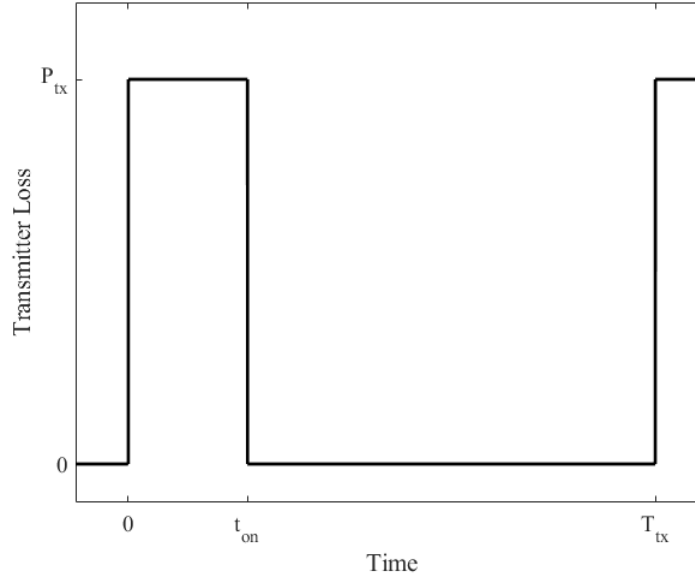


Figure 3.6: Expected Transmitter Duty Cycle

3.2 Three-Phase Transmitter Model

Due to the differing geometries of the single-phase and three-phase transmitters, it is necessary to develop unique thermal models. The three-phase system is analyzed first, using the previously described three-phase transmitter winding placement and core geometry. As inputs, the model requires the set of core and winding geometric parameters, the winding and core losses, and the winding and core volumes. Identifiers for the core and road materials can also be inputs if desired. The model outputs are the peak winding and road surface temperatures, but only the winding temperature is currently utilized by the system optimization.

3.2.1 Two-Dimensional Thermal Model

A two-dimensional TEC composed of cuboidal elements can be used to represent the roadway layout described previously. The division of the transmitter and roadway into these cuboidal elements is depicted in Fig. 3.7, where red elements are used to denote homogenized

winding material, green elements for core material, light grey for road material, medium grey for the base, and dark grey for the subbase.

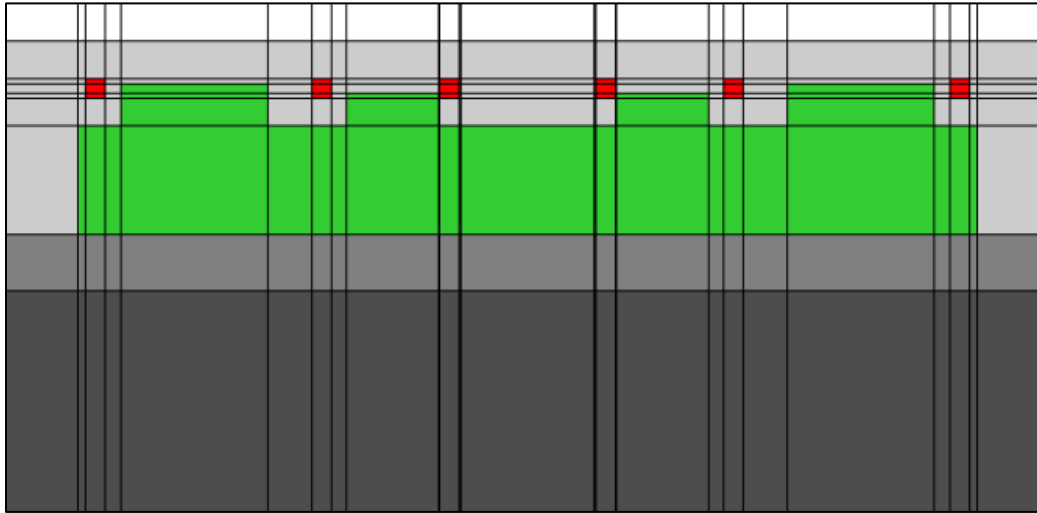


Figure 3.7: Two-Dimensional Transmitter Cuboidal Division

Since the height and presence of the transmitter teeth vary with each design, the cuboidal division is generated uniquely for each design. In the y-direction, the cuboid layers are defined as shown in Fig. 3.8, where the heights and number of the y-direction layers are determined by the top of a tooth (y_{t1} , y_{t2}), the top and bottom of the winding block (y_{w0} , y_{w1}), and top of the core base (y_{cb}). Each tooth or winding block can be divided into multiple cuboidal elements through this process.



Figure 3.8: TEC Y-direction Cuboidal Division

The division into x-direction layers is depicted in Fig. 3.9. Similarly, each x-direction layer is determined by the conductor placement between the neighboring teeth, where each layer is determined by the teeth start positions ($x_{t1,0}$, $x_{t2,0}$), teeth end positions ($x_{t1,l}$, $x_{t2,l}$), and winding block start and end positions (x_{w0} , x_{wl}).

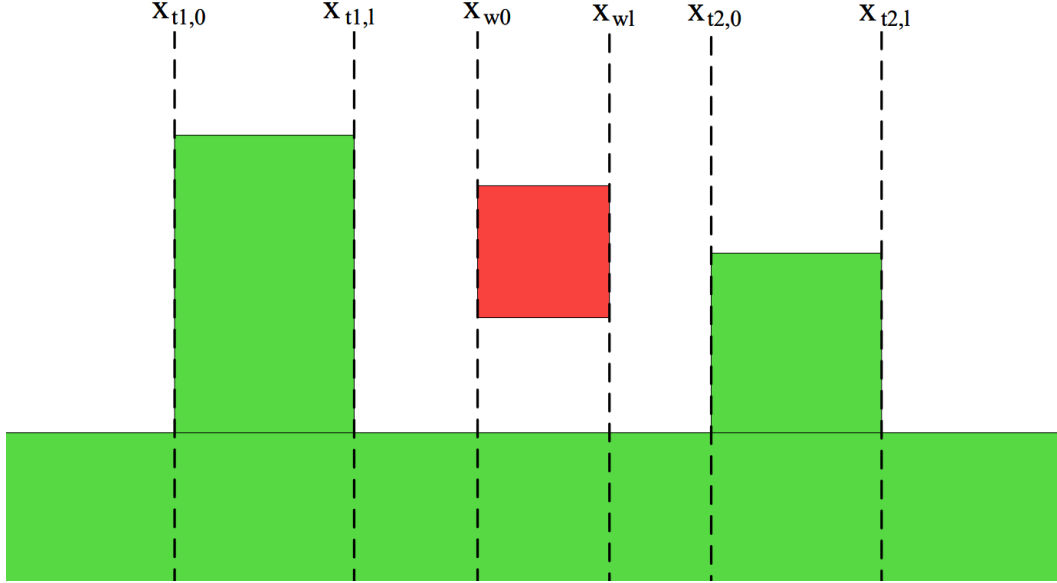


Figure 3.9: TEC X-direction Cuboidal Division

Because the wire is modeled with a rectangular cross-section, the total height of the winding block h_w and width per winding turn $\frac{w_w}{N_{tx}}$ are calculated as:

$$h_w = \frac{w_w}{N_{tx}} = 2r_w \quad (3.8)$$

where r_w is the radius of the Litz wire. Under this assumption, the cross-section of the actual winding is enclosed by the area of the cuboidal winding elements.

The final consideration in the TEC is the power that is dissipated in the transmitter windings and in the core material. It is assumed that the loss density is uniform in winding and in the core, so the loss in each winding cuboid $P_{w,cub}^{(i)}$ is calculated by:

$$P_{W,cub}^{(i)} = Vol_{cub}^{(i)} \frac{d \cdot P_{tx,W}}{Vol_{tx,W}} \frac{N_{tx} \pi r_W^2}{h_W w_W} \quad (3.9)$$

where the $P_{tx,W}$ is the total winding loss, $Vol_{tx,W}$ is the total winding volume, and $Vol_{cub}^{(i)}$ is the volume of the cuboid. The added factor in the winding loss ensures that the total loss across all winding elements is equivalent to the predicted value. The loss in each core cuboid $P_{C,cub}^{(i)}$ is similarly calculated by:

$$P_{C,cub}^{(i)} = Vol_{cub}^{(i)} \frac{d \cdot P_{tx,C}}{Vol_{tx,C}} \quad (3.10)$$

where $P_{tx,C}$ is the total core loss, $Vol_{tx,C}$ is the total core volume, and $Vol_{cub}^{(i)}$ is the volume of the cuboid. In both, i refers to the index of the cuboid within the full set of cuboids.

Typically, the core loss is concentrated closer to the windings and not uniformly distributed as in the model. However, the core loss is also typically much lower than the winding loss and influences the temperature rise to a much lesser extent, so this generalization likely has minimal impact on the accuracy of the model.

3.2.2 Three-Dimensional Thermal Model

The model up to this point can be used to evaluate a two-dimensional cross-section of the transmitter, which represents the majority of the transmitter length. However, the full three-dimensional model is also considered in which the end turns and neighboring transmitter segments are incorporated. The transmitter segment is broken into five sections along its length, as noted in Fig. 3.10, which shows the top-down view of a transmitter segment. Section F is shown twice since it is connected to both sections A and D, which produces the effect of neighboring transmitter segments. The previously shown cross-section from Fig. 3.4 and Fig. 3.7 describe section C in this configuration.

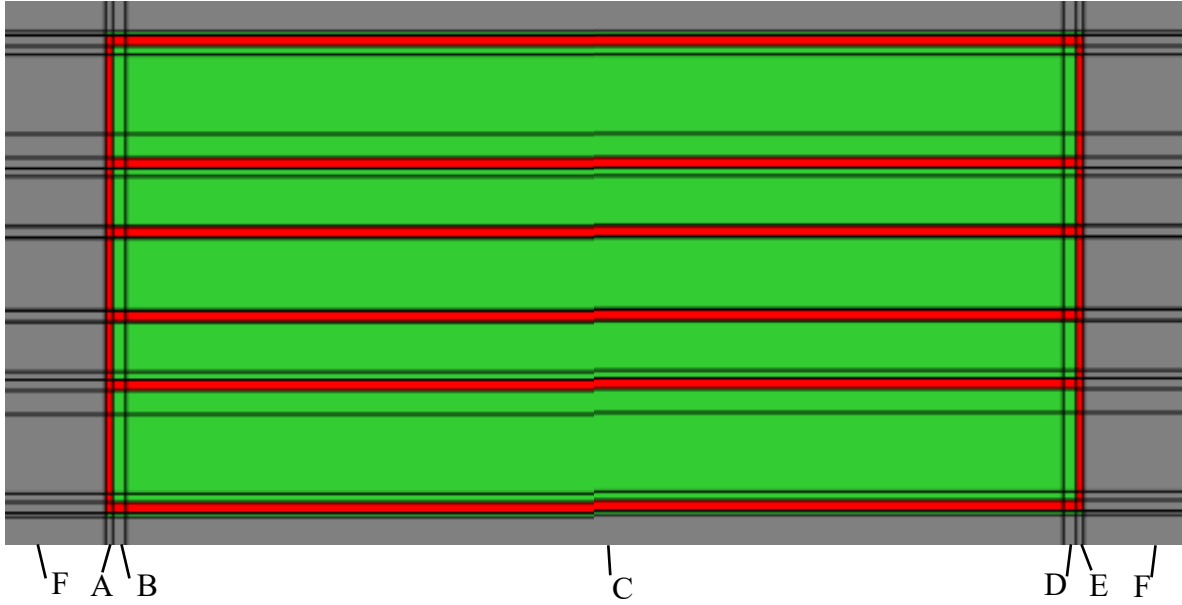


Figure 3.10: Three-Dimensional Transmitter Sections

Since the thermal model is built using cuboids, the end turns of the winding cannot be added in their exact form, and a rectangular approximation is used. In this simplified construction, the winding continues in the z -direction at the start of the end turns. Sections B and D correspond to this portion of the transmitter segment, depicted in Fig. 3.11. The division into cuboidal elements in this section utilizes the same grid as in section C but omits the core teeth. The length of the elements in this section is equivalent to the bend radius r_b of the end turns, which is approximated as:

$$r_b = 10 r_w \quad (3.11)$$

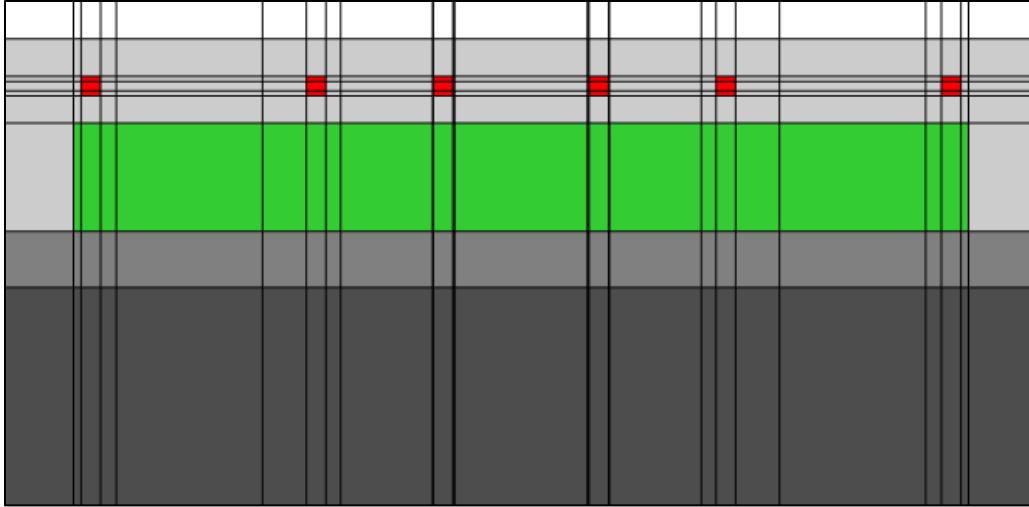


Figure 3.11: Transmitter Sections B and D Cuboidal Division

The remaining end turn winding is inserted in the spaces between the winding cuboids of the preceding two sections, completing the turns. This is the construction of cuboidal elements in sections A and E, shown in Fig. 3.12. The length of these sections should be the same as the winding diameter, but because the different phase windings overlap at certain points in the end winding, the length is increased by half.

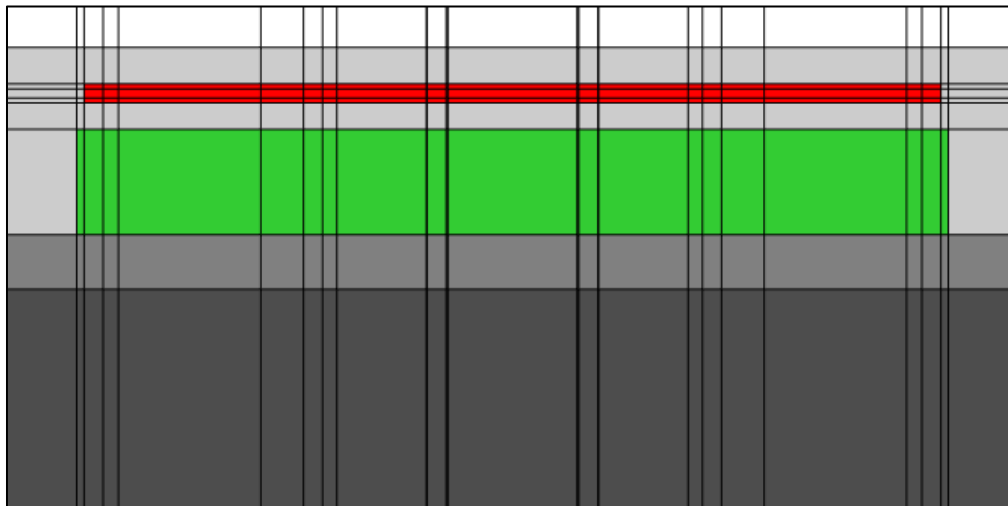


Figure 3.12: Transmitter Sections A and E Cuboidal Division

The last section contains the remaining road material between two transmitter segments. The same grid of cuboidal elements is maintained from the previous arrangements, with all core

and winding elements being replaced by the road material, as shown in Fig. 3.13. The section F cuboidal division could be simplified to a handful of cuboids; however, in the greater context of all the other sections, it is not difficult to include and does not add significant computation time.

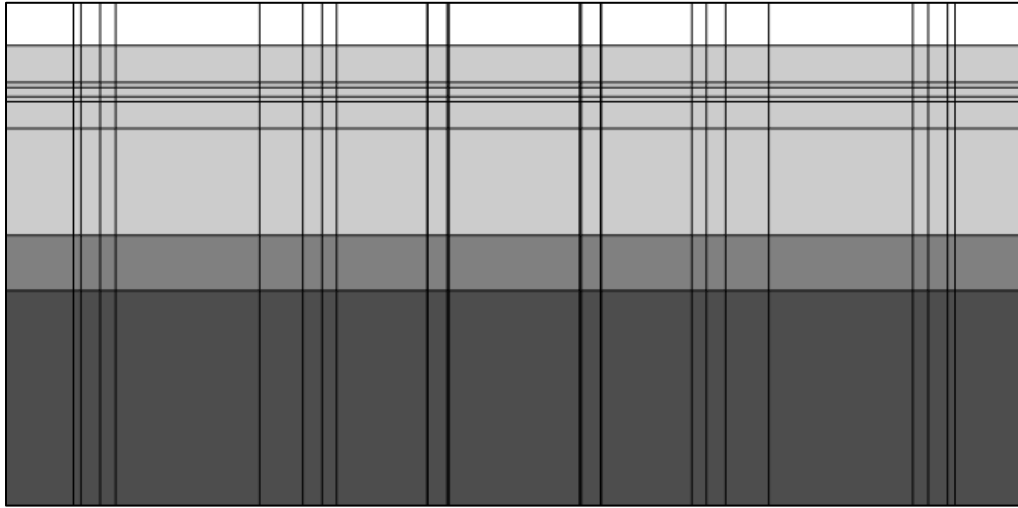


Figure 3.13: Transmitter Section F Cuboidal Division

3.2.3 Thermal Model Evaluation

To assess the quality of the three-phase transmitter TEC model, a three-dimensional steady-state thermal finite element analysis (FEA) simulation was created for the discussed transmitter and roadway layout. The same material properties and boundary conditions were assigned in both models. For the high heat condition, the amount of solar radiation at the road surface was determined using the FEA model. With no power dissipation in the transmitter winding and core, the solar heat flux was tuned until the surface temperature reached approximately 60°C. The magnitude of the surface heat flux as well as the heat transfer coefficient of the road surface are listed in Table 3.3. The same boundary properties are used for both concrete and asphalt roadways, since the heat transfer coefficient is a generalized estimate of a road-to-air boundary. It is noted that the amount of solar radiation on the road surface is typically higher in reality; however, the emissivity of the road surface, which dictates the amount of heat that is radiated away from the road, is not considered in these models, and a greater heat flux would be required to reach 60°C at the surface under this condition. The TEC model cannot represent emissivity, so it is not included in either model to maintain the consistent conditions in the validation.

Table 3.3: Thermal Model Boundary Properties

	Parameter Value
Heat transfer coefficient $\left(\frac{W}{m^2 \cdot ^\circ C}\right)$	12
Road surface heat flux $\left(\frac{W}{m^2}\right)$	300

For the standard heat condition, in which the air temperature is set to 22 °C, the heat distribution maps across the x-y cross-section of the transmitter for both models are shown in the following figures for concrete roadways. The temperatures shown for the TEC model indicate the temperatures from the mean nodes of each cuboid. It can be seen that there is a similar heat distribution in both models, but the TEC predicts higher overall temperatures.

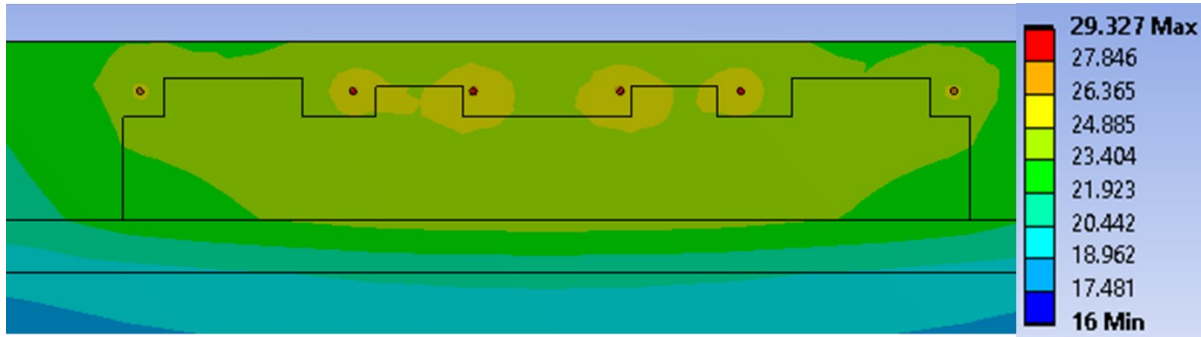


Figure 3.14: FEA Results for Concrete Roadway under Standard Conditions

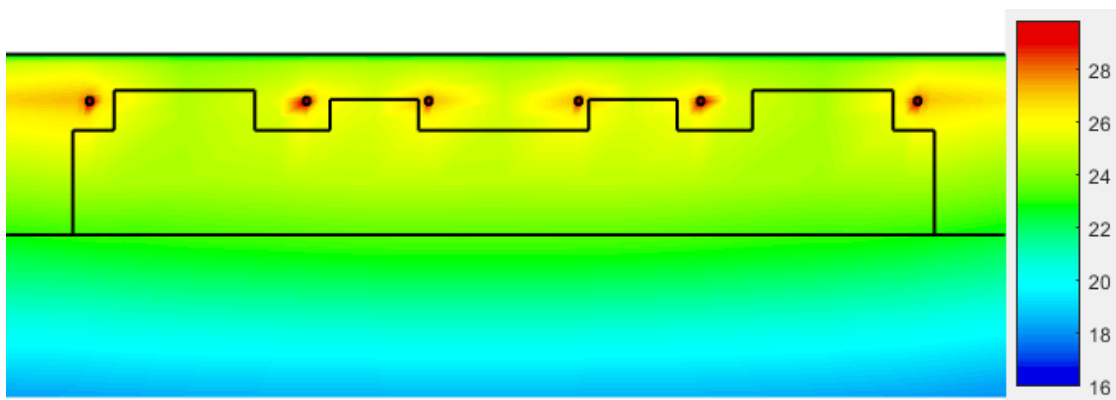


Figure 3.15: TEC Results for Concrete Roadway under Standard Conditions

Under the high heat condition, there is an additional difference between the TEC and FEA models. The effect of solar radiation on the road surface is considered here, and in the FEA model,

a heat flux density can be assigned to flow into the road surface. However, in the TEC model, the heat generated by the solar radiation is assigned to the nodes on the road surface. Therefore, the amount of solar radiation differs between models, since it is determined as the amount needed to reach 60 °C at the road surface without transmitter power loss. The TEC and FEA model heat distributions are shown for the high heat condition in the following figures. The peak temperatures are overestimated by a few degrees in high heat case, but in general, the heat distributions are very similar between the models.

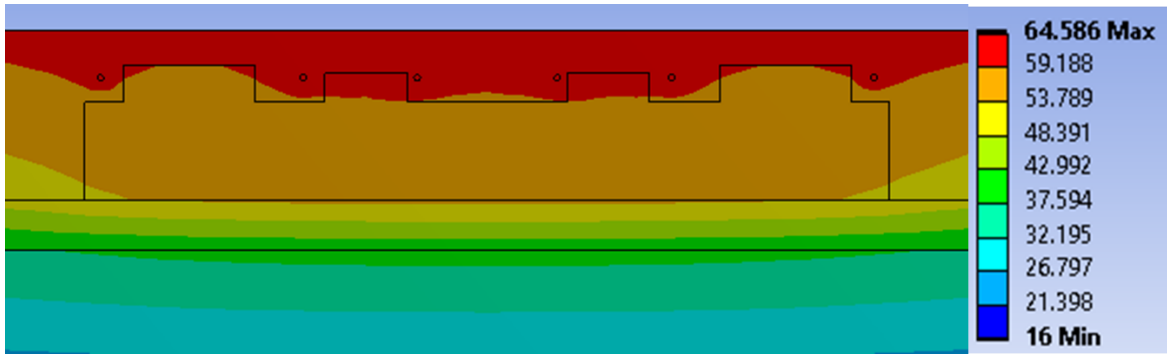


Figure 3.16: FEA Results for Concrete Roadway under High Heat Conditions

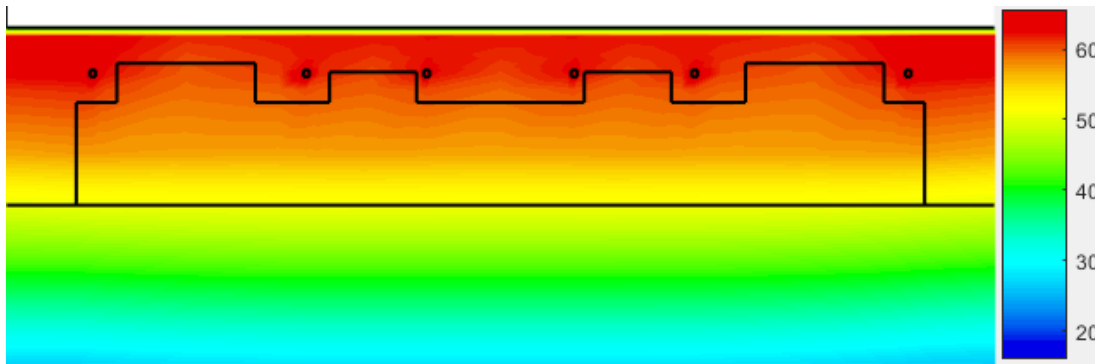


Figure 3.17: TEC Results for Concrete Roadway under High Heat Conditions

Comparing the peak winding $T_{w,Pk}$ and peak surface $T_{s,Pk}$ temperatures of the concrete roadway from the different models, the same observation can be made. The TEC models predict higher temperatures compared to the FEA model, as seen in Table 3.4, however the temperatures difference between models is only around a few degrees for both the winding and surface temperatures. Additionally, the 2D and 3D TEC models perform nearly identically, which is

beneficial for the full system genetic optimization, since the quicker 2D model can be used. It is also noted that only the 2D TEC heat distributions are shown to avoid redundancy.

Table 3.4: Thermal Model Comparison and Validation for Concrete Roadway

		TEC 2D	TEC 3D	FEA
Standard	$T_{w,Pk}$ (°C)	29.84	29.20	29.33
	$T_{S,Pk}$ (°C)	25.26	25.86	24.23
High Heat	$T_{w,Pk}$ (°C)	65.65	65.28	64.59
	$T_{S,Pk}$ (°C)	63.72	64.26	62.29

Using the same boundary conditions and transmitter design, the same studies are carried out again with asphalt as the road material. Both the standard and high heat cases are considered, with results from the TEC and FEA methods shown in Figs. 3.18-3.21 and Table 3.5. Compared to the concrete roadway, slightly higher temperatures are seen in the asphalt roadway studies; however, the differences are relatively small. As with the previous results, the TEC model also predicts overall higher temperatures than the FEA model for an asphalt road, and a similar behavior is seen with the surface temperatures in the high-heat scenario.

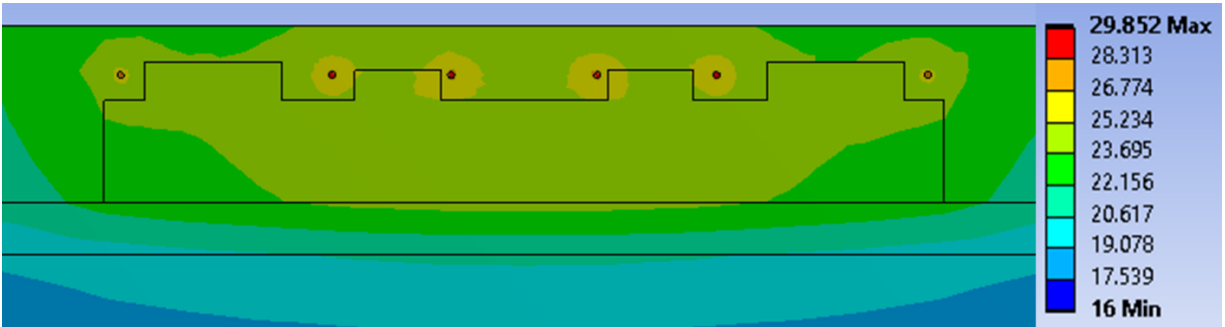


Figure 3.18: FEA Results for Asphalt Roadway under Standard Conditions

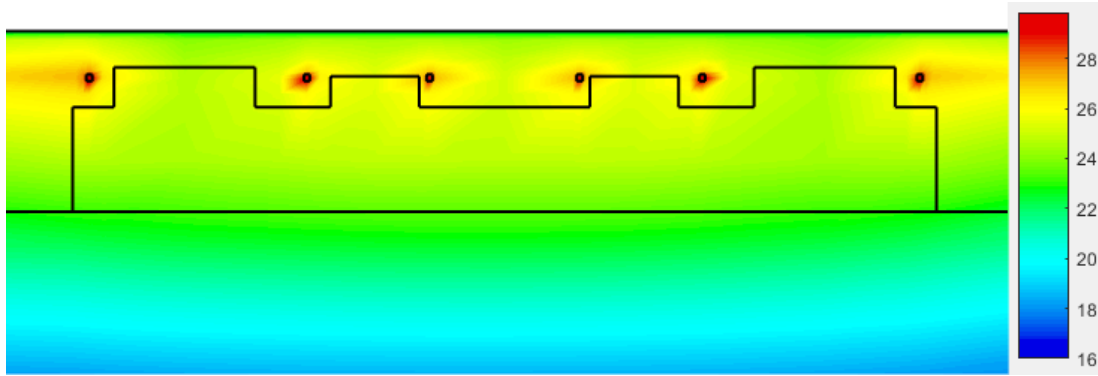


Figure 3.19: TEC Results for Asphalt Roadway under Standard Conditions

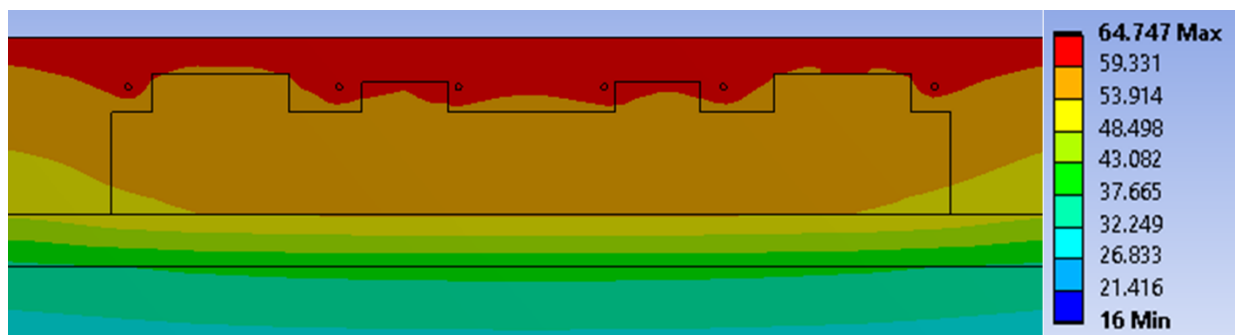


Figure 3.20: FEA Results for Asphalt Roadway under High Heat Conditions

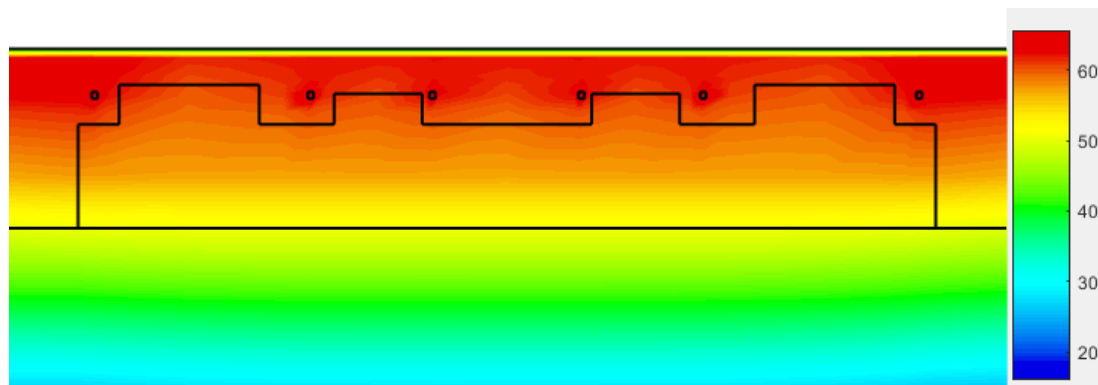


Figure 3.21: TEC Results for Asphalt Roadway under High Heat Conditions

Table 3.5: Thermal Model Comparison and Validation for Asphalt Roadway

		TEC 2D	TEC 3D	FEA
Standard	$T_{w,Pk}$ (°C)	29.84	29.84	29.85
	$T_{S,Pk}$ (°C)	25.26	26.15	24.24
High Heat	$T_{w,Pk}$ (°C)	65.65	65.62	64.74
	$T_{S,Pk}$ (°C)	63.72	64.62	62.35

3.3 Single-Phase Transmitter Model

Using a similar process as the three-phase transmitter, a thermal model of the single-phase transmitter is also created and validated. The roadway environment enclosing the single-phase transmitter is divided into cuboidal elements, but a simpler approach can be taken for in the single-phase case. Since the height of the transmitter teeth never intersect the winding, a fixed TEC can be used here, unlike the three-phase system where a new TEC must be generated for each design.

The cuboidal element division in Fig. 3.22 is used to represent the single-phase transmitter. As previously specified with Fig. 3.7, red elements denote homogenized winding material, green elements denote core material, and the light to dark grey elements denote road, base, and subbase material, respectively. Again, the cuboidal elements are a simplified version of the realistic transmitter layout, specifically in that the winding blocks encapsulate and homogenize multiple turns of Litz wire. Additionally, the winding cuboids are placed fully within the base of the core, whereas in the realistic transmitter, the winding block is only partially recessed into the core.

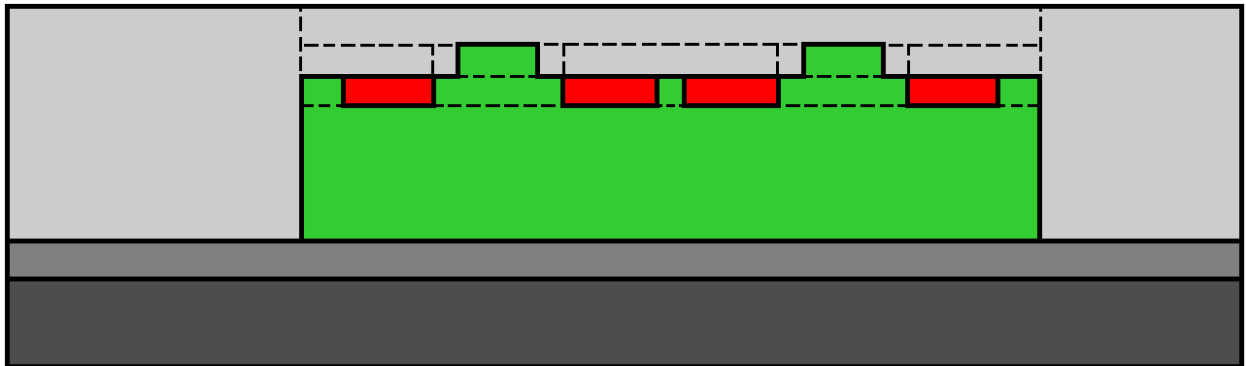


Figure 3.22: Single-Phase Transmitter Cuboidal Distribution

To estimate the power dissipation in each element, the same method involving the winding and core loss densities is utilized. The winding block size is determined by (3.8), and the losses in each winding and core cuboid are calculated using (3.9)-(3.10).

The 2-dimensional representation of the transmitter is fully described, which essentially models a continuous transmitter core and winding along the length of the roadway. To account for the 3-dimensional transmitter construction, based on 15-foot segments, the thermal model can be expanded to include the end turns and extra road material. The top-down view of the transmitter is shown in Fig. 3.23, which shows the division into lengthwise cuboidal layers. The cross-section of section C is the 2-dimensional model from Fig. 3.22. Since cuboidal elements are used to represent round end turns, the transmitter sections are just approximations of the actual transmitter layout. It is also noted that the end turns are duplicated onto the opposite end of the transmitter, and the terminals are not included in the model.

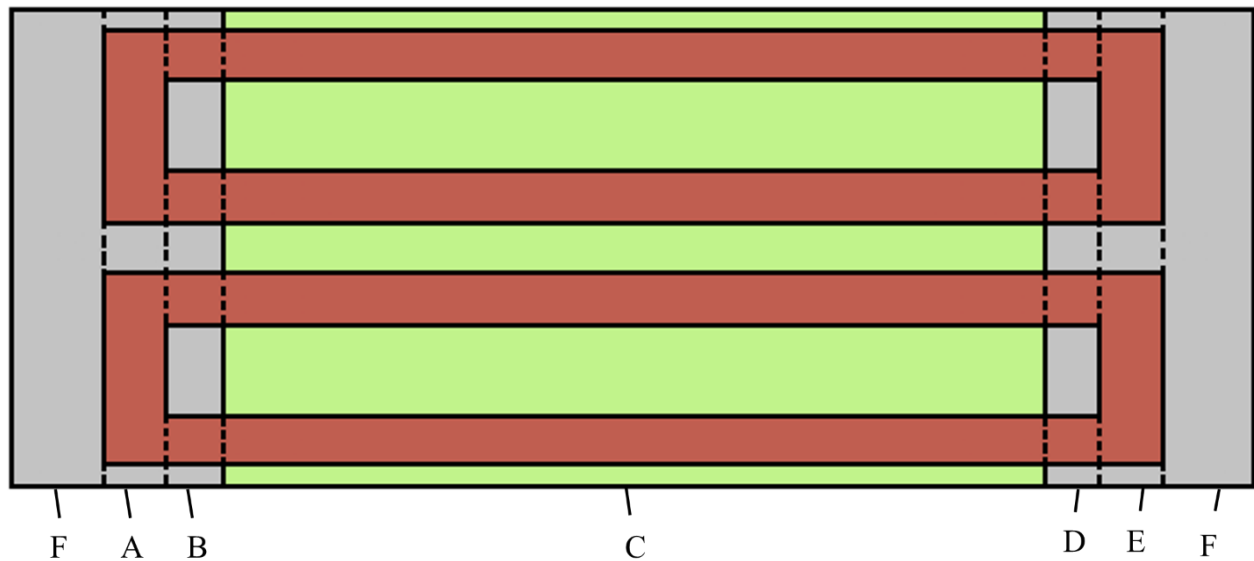


Figure 3.23: Transmitter Sections

Adjacent to the main section of the transmitter, the cuboidal division of sections B and D are depicted in Fig. 3.24. The length of sections B and D are set to the bend radius of the windings, which is approximated with (3.11). The winding and base of the core extend into this section, but the teeth are not present.

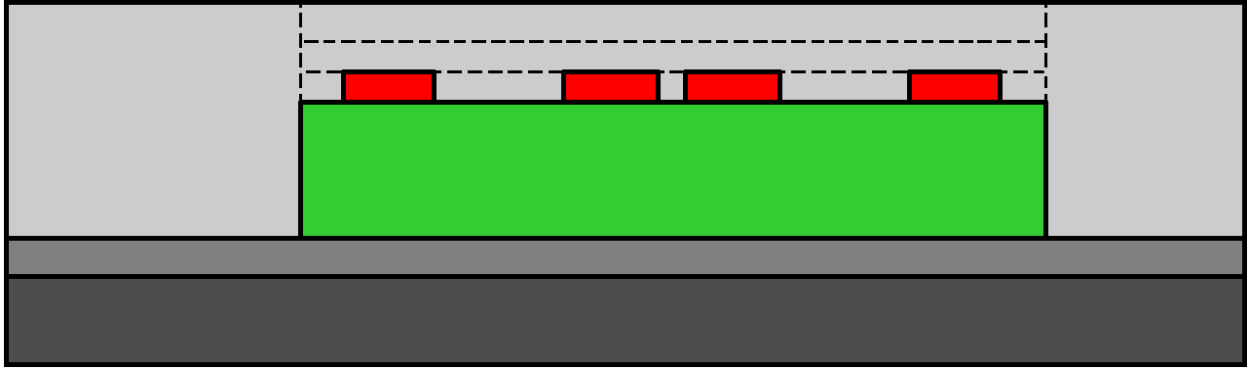


Figure 3.24: Sections B and D Cuboidal Distribution

The remaining sections of the end turns are sections A and E, whose cuboidal element division is shown in Fig. 3.25. The length of these sections is set to the winding block width w_w from sections B, C, and D. The winding blocks here connect the pairs of winding blocks in sections B and D, and the base of the core continues beneath the winding.

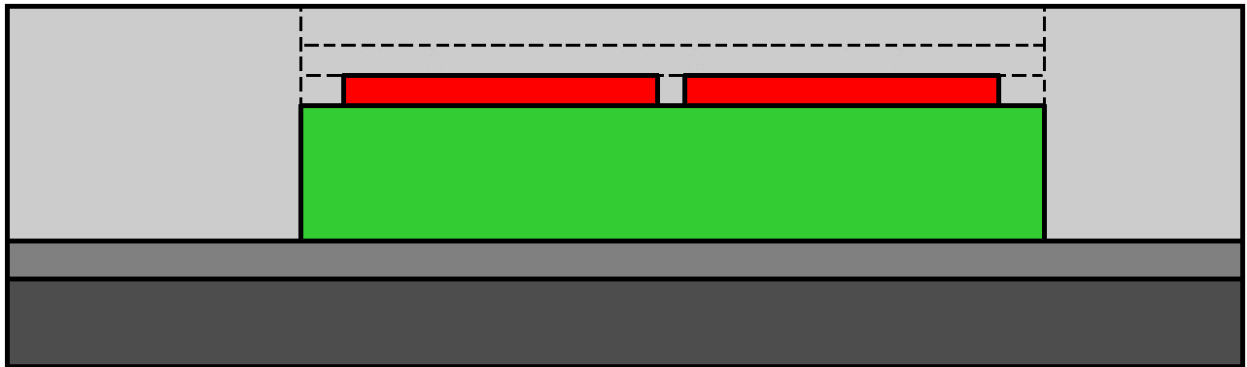


Figure 3.25: Sections A and E Cuboidal Distribution

The final section F connects the start and end of neighboring transmitter segments, and its length is determined by removing the combined lengths of section A through E from the 15-foot length of the segment. The cuboidal division is depicted in Fig. 3.26. This section does not contain any core or winding material, and is primarily composed of just the road material.

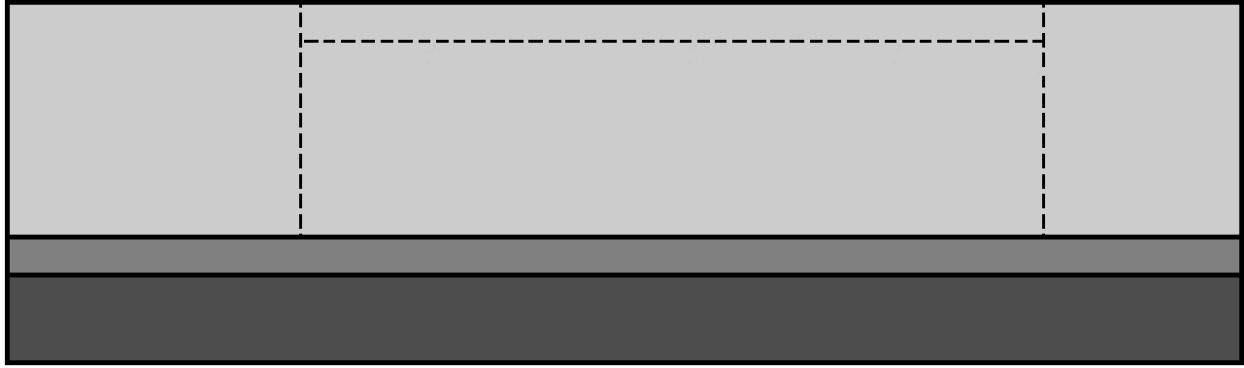


Figure 3.26: Section F Cuboidal Distribution

Present in all the cross-sections of Figs. 3.24-3.26 are cuboids for the road surface, neighboring lane, shoulder, base layer, and subbase layer. These cuboids extend across the total length of the model, which is why they are present in each section.

3.3.1 Thermal Model Evaluation

To evaluate the thermal model, a steady-state thermal FEA was created using the same parameters and boundary conditions as in the three-phase model. The value of the heat flux was changed to 270 W/m^2 , which results in approximately 60°C at the surface for the single-phase FEA model. The performance was considered for concrete and asphalt roadways and for the previously discussed standard and high heat conditions. While both 2D and 3D TEC models were considered for the three-phase transmitter, only the 3D TEC model is considered in the single-phase system. The simplified cuboidal element arrangement significantly reduces the total number of elements, which allows the 3D TEC to be solved quickly and eliminates the need for a faster 2D version.

The results for the transmitter with a concrete roadway under the standard conditions are shown in Fig. 3.27 and Fig. 3.28. Comparing the temperature distribution for the TEC and FEA methods, it is seen that the temperatures are roughly the same, and the location of the peak temperatures is in the winding for both. The single-phase TEC results are much lower resolution than the FEA results, which seems to affect the prediction of the peak temperatures in the roadway.

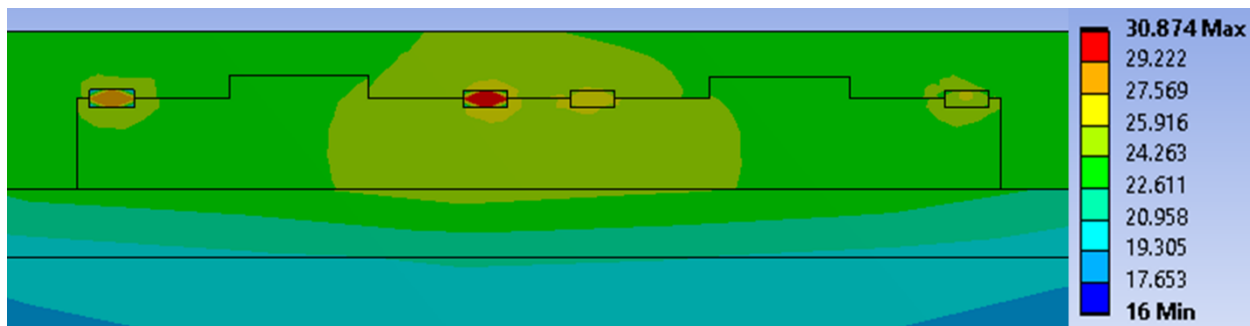


Figure 3.27: FEA Results for Concrete Roadway under Standard Conditions

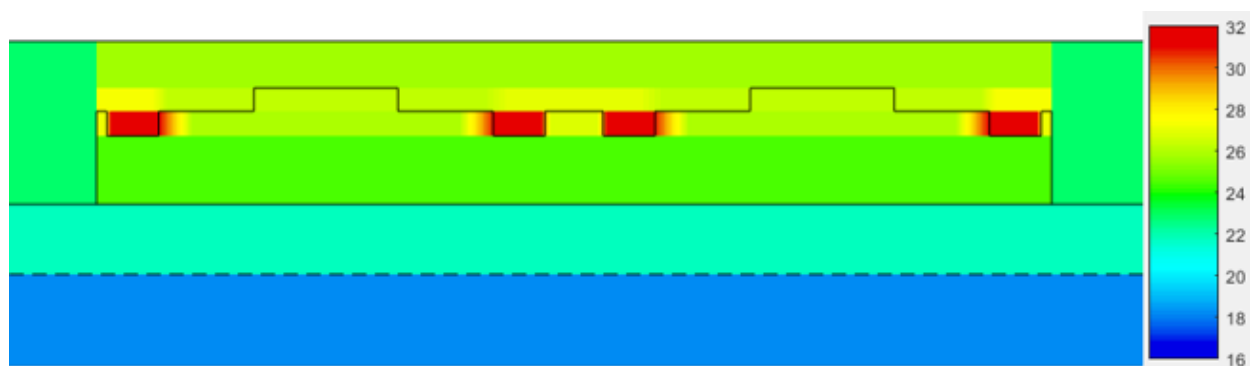


Figure 3.28: TEC Results for Concrete Roadway under Standard Conditions

Under the high heat conditions, it is also seen that the TEC and FEA models predict similar peak temperatures in the windings, shown in the results of Fig. 3.29 and Fig. 3.30. The temperature range throughout the transmitter is also very similar between models, although with noticeably lower resolution.

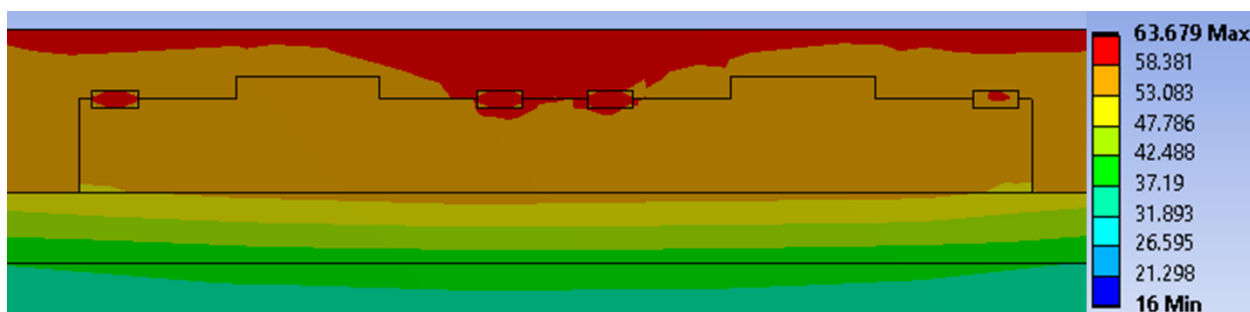


Figure 3.29: FEA Results for Concrete Roadway under High Heat Conditions

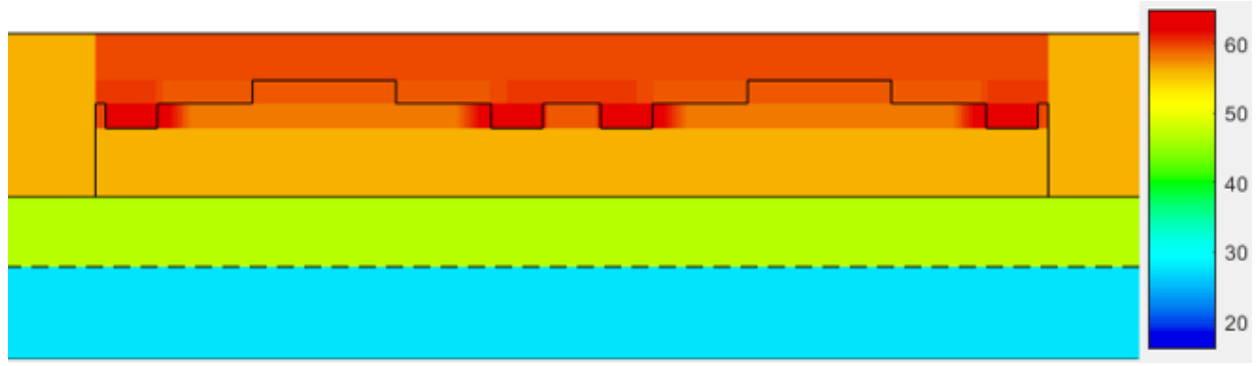


Figure 3.30: TEC Results for Concrete Roadway under High Heat Conditions

The peak winding and surface temperatures for each concrete roadway variation are listed in Table 3.6. It can be seen that peak winding temperatures predicted by the TEC model are within a couple degrees of the FEA model, suggesting that the TEC is a reliable method for checking the winding temperature. There is a bigger difference between the predicted surface temperatures of either model, with the TEC results being slightly lower. This is primarily due to the simple cuboid structure of the road surface in the TEC, which results in value closer to the mean road surface temperature.

Table 3.6: Concrete Roadway Thermal Model Comparison

		TEC 3D	FEA
Standard	$T_{w,Pk}$ (°C)	32.06	30.87
	$T_{s,Pk}$ (°C)	22.81	25.20
High Heat	$T_{w,Pk}$ (°C)	64.94	63.68
	$T_{s,Pk}$ (°C)	55.89	60.98

The same models are then evaluated for an asphalt roadway. The standard condition results are shown in Fig. 3.31 and Fig. 3.32. Relative to the concrete roadway, higher temperatures are seen in the asphalt roadway, but these differences are within a few degrees. Comparing the TEC and FEA thermal distributions, it is seen that the peak winding temperatures and overall transmitter temperature range are very similar. Although, the peak road temperatures are underestimated in the TEC.

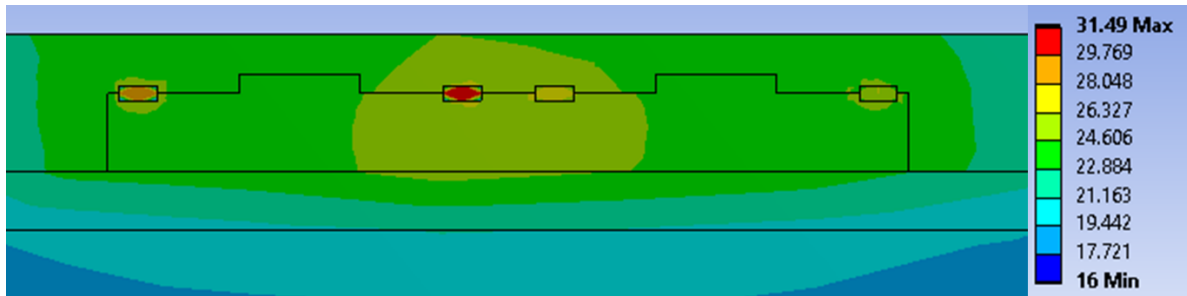


Figure 3.31: FEA Results for Asphalt Roadway under Standard Conditions

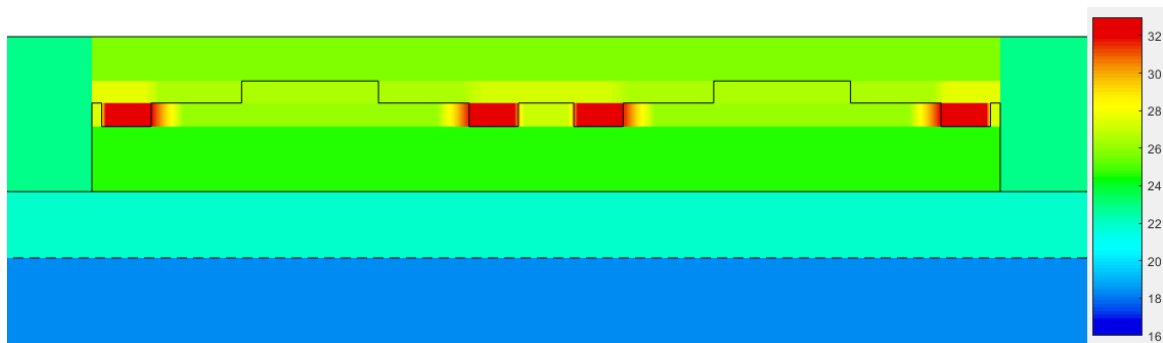


Figure 3.32: TEC Results for Asphalt Roadway under Standard Conditions

Looking at the high heat performance for the asphalt roadway in Fig. 3.33 and Fig. 3.34, the same relationships are observed. The asphalt temperature is a little higher than the concrete, and the temperature distribution is similar between the FEA and TEC methods. As noted previously, there is lower resolution in the TEC models, which leads to a decrease in the evaluated peak roadway temperatures.

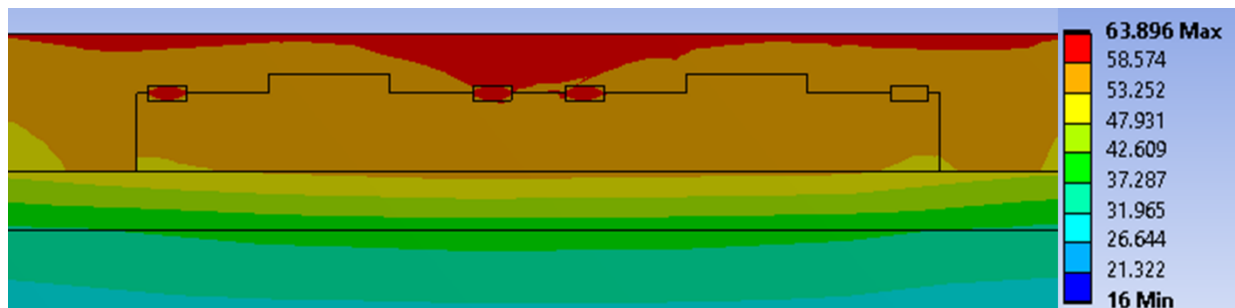


Figure 3.33: FEA Results for Asphalt Roadway under High Heat Conditions

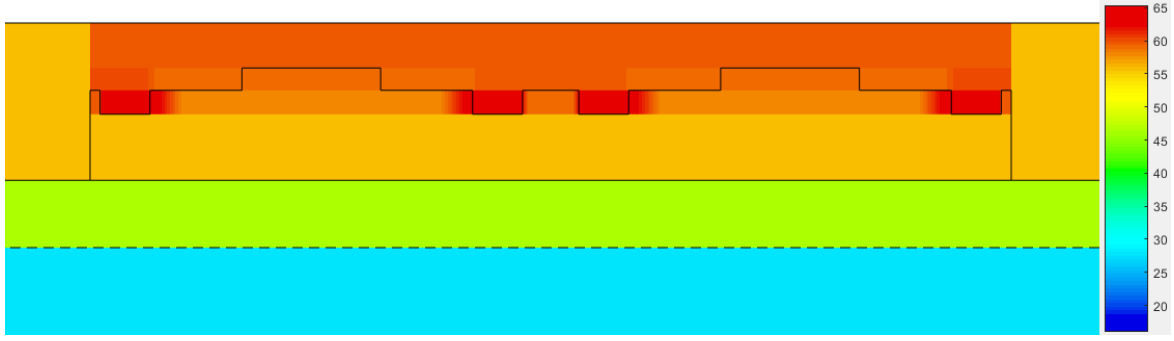


Figure 3.34: TEC Results for Asphalt Roadway under High Heat Condition

The peak winding and surface temperatures are listed for the different asphalt roadway variations in Table 3.7. As seen in the concrete roadway results, the TEC method calculates peak winding temperatures that are close to those of the FEA, but the surface temperatures are underestimated in both the standard and high heat scenarios, likely as an effect from the low road surface resolution. Overall, the TEC proves to determine the winding temperature reliably, and is useful for very rough estimates of the surface temperature.

Table 3.7: Asphalt Roadway Thermal Model Comparison

		TEC 3D	FEA
Standard	$T_{w,Pk}$ (°C)	32.98	31.49
	$T_{s,Pk}$ (°C)	22.87	25.24
High Heat	$T_{w,Pk}$ (°C)	65.37	63.90
	$T_{s,Pk}$ (°C)	55.69	61.15

3.4 Thermal Model Limitations

While the evaluations of the single and three-phase transmitter TEC models show that they can be used in place of the FEA models, this assumes that the FEA model is an accurate representation of the real transmitter performance. A primary source of potential error is the homogenization of the Litz wire material, since this directly affects the analysis of the winding temperature. Because the real internal winding temperature could be higher than the model predictions, any constraints involving the transmitter temperatures utilize conservative limits.

Another source of potential inaccuracies are the assumptions of the boundary temperatures and parameters. There is a high degree of variability in road environment conditions can make it difficult to determine the appropriate parameters to use in the models. However, the FEA and TEC results should be good reflections of the real transmitter thermal performance if the considered boundary conditions are accurate.

4. OPTIMIZATION OVERVIEW

To facilitate the design of the DWPT systems, a genetic algorithm-based optimization is utilized. Two fitness objectives are used in these studies: loss and volume. The loss objective ensures that the generated system designs are as efficient as possible, which is critical for potential DWPT installations. System size and cost are also key concerns for DWPT adoption, and the volume objective directly regulates the total size of the system and serves as a stand-in for the cost. As in [4], a distinct cost objective can be added; however, the price volatility and availability of certain materials at this time mitigate the effectiveness of this metric. To handle the genetic algorithm computations, the genetic algorithm optimization toolbox GOSET [19] is utilized.

The system fitness function incorporates the previously described component models to determine the loss and volume of the collective system. The general structure is depicted in Fig. 4.1, with descriptions of the variables and subscripts listed in Tables 4.1a and 4.1b. The fitness function is originally established in [7], but modifications are incorporated from [20]. Fundamentally, a unique set of genes is received as input, and the fitness metrics are calculated while various constraints are imposed to ensure reasonable designs.

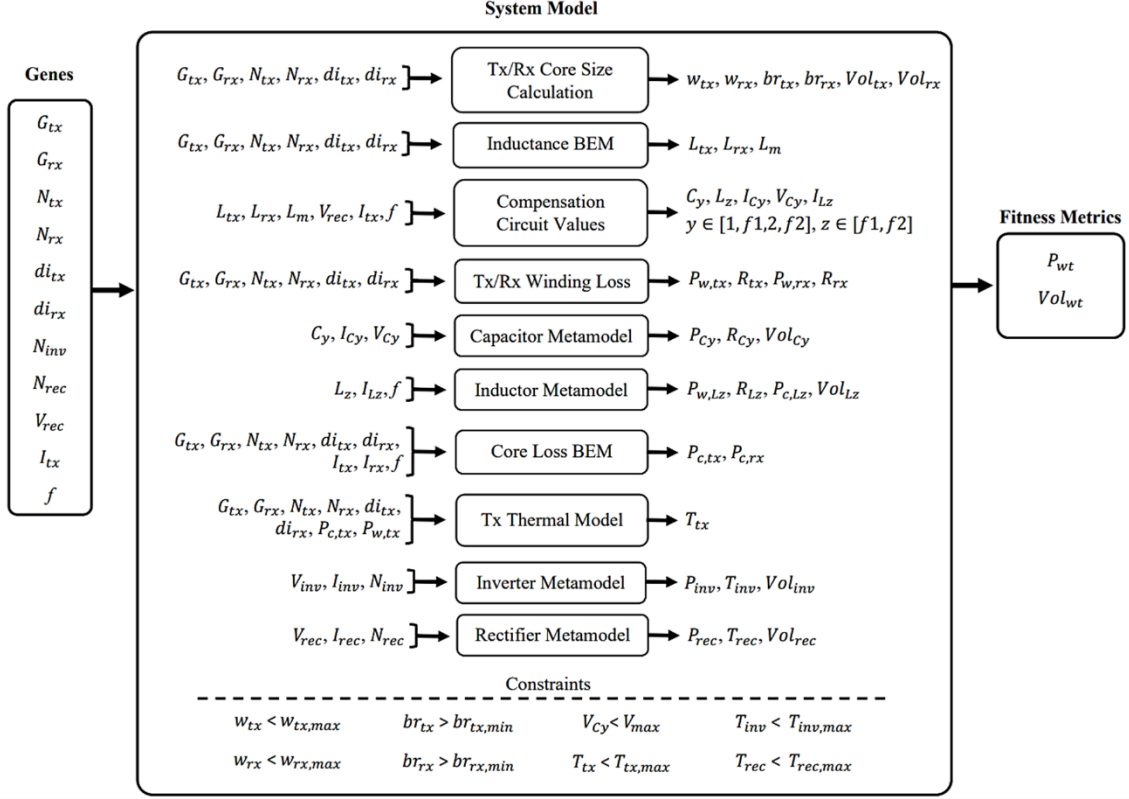


Figure 4.1: System Optimization Fitness Function Overview

Table 4.1: Fitness Function Parameter Descriptions

a) Variable Descriptions

Variable	Description
G	Structure of geometric parameters
$N (N_{tx}, N_{rx})$	Number of turns
$N (N_{inv}, N_{rec})$	Number of devices
di	Winding diameter
V	Voltage
I	Current
f	Fundamental frequency
w	Width
br	Winding bend radius
Vol	Volume
L	Inductance
C	Capacitance
P	Power loss
R	Resistance
T	Temperature

b) Subscript Descriptions

Subscript	Description
tx	Transmitter
rx	Receiver
inv	Inverter
rec	Rectifier
w	Winding
c	Core
m	Mutual inductance (Lm)
y, Cy	Compensation capacitors (i.e. $C1, Cf1, C2, Cf2$)
z, Lz	Compensation inductors (i.e. $Lf1, Lf2$)
wt	Weighted total

Each set of genes defines a unique system design, so they must contain the required information to fully specify the physical aspects and operation of the corresponding system. As shown in Fig. 4.1, the genes contain the geometric parameters of the transmitter and receiver, the number of turns and diameter of their windings, the number of power electronic devices, the rectifier voltage, transmitter current, and system frequency. It is noted that G_{tx} and G_{rx} are comprised of multiple different genes, as described in Section 2.1, but are labeled this way for simplicity. By following the fitness function outline and understanding the component models, one can clearly see that this set of genes is sufficient to determine the loss and volume of all necessary system components.

While it might be expected that the system fitness is a direct sum of all the component fitness values, it is seen that the assigned fitness is a weighted sum of the losses and volumes. This is primarily used to reduce the dominance of the transmitter and receiver in determining the volume fitness metric. The weights used in this optimization setting are listed in Table 4.2 and established by [20]. Using the weights, the fitness metrics are determined by (4.1):

$$fit_{wt} = \sum_i wt_{fit,i} \cdot fit_i \quad (4.1)$$

where fit refers to either the loss or volume fitness objective, and i refers to the index in the set of components as listed in. Because the transmitter and receiver core volumes are typically an order of magnitude larger than the other component volumes, a weighting of 0.1 is applied. This influences the optimization to minimize the compensation circuit and power electronic volumes in

a similar regard as the transmitter and receiver volumes. Additionally, when the core material is non-magnetic, there is no trade-off between the magnetic performance and the core volume within the optimization, and the weight on that core volume is set to 0.

Table 4.2: Fitness Metrics Weights

Component	Loss Weight	Volume Weight (w\ tx core)	Volume Weight (w\o tx core)
Inverter	1	1	1
L_{f1}	1	1	1
C_{f1}	1	1	1
C_1	1	1	1
Tx Winding	1	1	1
Tx Core	1	0.1	0
Rx Core	1	0.1	0.1
Rx Winding	1	1	1
C_2	1	1	1
C_{f2}	1	1	1
L_{f2}	1	1	1
Rectifier	1	1	1

4.1 Constraints

In addition to determining the fitness metrics of each component, constraints must be included to remove unrealistic or problematic designs. If a constraint is violated, the fitness of the design is set to a small negative number to influence gene evolution away from such genes. Constraints in the fitness function are imposed for geometric, electrical, and thermal conditions, as established in [7] and [20].

The geometric constraints are evaluated at the same point in the fitness function, which is at the beginning before the transmitter and receiver volume calculations. The widths of the transmitter w_{tx} and receiver w_{rx} are determined differently depending on the topology, but they are subject to the same following constraints:

$$w_{tx} < w_{tx,max} \quad (4.2)$$

$$w_{rx} < w_{rx,max} \quad (4.3)$$

where $w_{tx,max}$ and $w_{rx,max}$ are the maximum allowed transmitter and receiver widths, which must be less than 12 ft to fit in a standard highway lane. The remaining geometric constraints account for the minimum bend radius of the Litz wire that is recommended by the manufacturer, discussed in earlier chapters. The bend radii implied by each transmitter and receiver, br_{tx} and br_{rx} , are also dependent on the topology but with the same following constraints:

$$br_{tx} > br_{tx,min} \quad (4.4)$$

$$br_{rx} > br_{rx,min} \quad (4.5)$$

where $br_{tx,min}$ and $br_{rx,min}$ are the minimum bend radius for the wire gauge of the transmitter and receiver.

Electrically, the only constraints included are for the compensation capacitor voltages. This constraint is included as a safety precaution intended to limit the voltage from any electrical node to ground. The constraint for compensation capacitor voltages V_{cy} for $y \in [1, f1, 2, f2]$ is:

$$V_{cy} < V_{max} \quad (4.6)$$

$$\text{for } y \in [1, f1, 2, f2] \quad (4.7)$$

where the maximum allowed voltage V_{max} is typically set to 1 kV.

The last set of constraints account for thermal limits in the transmitter and power electronics. In the transmitter, the winding temperature T_{tx} determined by the thermal model is limited by the following condition:

$$T_{tx} < T_{tx,max} \quad (4.8)$$

where $T_{tx,max}$ is based on maximum temperature guidelines from the manufacturer. In this optimization, a conservative 90 degree C is used, which is below the manufacturer specified limit. For the power electronics, the inverter and rectifier temperatures, T_{inv} and T_{rec} , are similarly limited to a manufacturer specified maximum through the following conditions:

$$T_{rec} < T_{inv,max} \quad (4.9)$$

$$T_{inv} < T_{rec,max} \quad (4.10)$$

where $T_{inv,max}$ and $T_{rec,max}$ are retrieved from the datasheets. These constraints are sufficient for producing reliable designs in most cases, but they are not exhaustive. Additional constraints can be added to the fitness function to cover any perceived oversights.

4.2 Optimization Studies

To demonstrate the benefits of the optimization design method, a series of optimization studies are performed in which the core materials as well as the gap distance are varied. The considered core materials include magnetized concrete Magment, ferrite, and no core (i.e. no magnetic material). The gap sizes considered are 26 cm, which is within the common range of gap distances among other DWPT systems, and 18 cm, which is around the lowest gap size seen among other DWPT systems. Each study size is 500 population by 500 generations.

The single-phase topology is optimized in the following studies, and the full list of the genes and their ranges are provided in Table 4.3. The same gene range is used for each study variation. Although the optimization process is described for both single- and three-phase systems, the single-phase system is chosen for these demonstrations because it utilizes fewer genes and converges more fully than the three-phase.

Table 4.3: Optimization Gene Ranges

Gene	Minimum Value	Maximum Value	Gene Type
hb_{tx}	0.10 m	0.30 m	Linear
hs_{tx}	0.01 m	0.0635 m	Linear
ws_{tx}	0.05 m	0.20 m	Linear
$sratio$	1.01	1.50	Linear
sep_{tx}	0.01 m	0.20 m	Linear
$dsep_{tx}$	0.01 m	0.15 m	Linear
$csep_{tx}$	0.01 m	0.15 m	Linear
N_{tx}	1	20	Integer
wb_{rx}	0.10 m	1.00 m	Linear
hb_{rx}	0.01 m	0.20 m	Linear
wt_{rx}	0.01 m	0.10 m	Linear
ht_{rx}	0.05 m	0.20 m	Linear
Nh_{rx}	1	20	Integer
Nv_{rx}	1	20	Integer
l_{rx}	0.01 m	0.20 m	Linear
f	20 kHz	85 kHz	Linear
I_{tx}	250 A	400 A	Linear
di_{tx}	0.01 m	0.02 m	Linear
di_{rx}	0.01 m	0.02 m	Linear
N_{inv}	1	2	Integer
N_{rec}	1	2	Integer
V_{rec}	500 V	1000 V	Linear

In each study, multiple design parameters are plotted to compare between the variation in materials and gap size. One key aspect is the coupling factor k , which is defined by the following equation:

$$k = \frac{L_m}{\sqrt{L_{tx}L_{rx}}} \quad (4.11)$$

where L_{tx} is the transmitter self-inductance, L_{rx} is the receiver self-inductance, and L_m is their mutual inductance. Occasionally interchanged with the loss objective P_{wt} , the system efficiency η is another metric and is defined as:

$$\eta = \frac{P_{out}}{P_{out} + P_{wt}} \quad (4.12)$$

where P_{out} is the output power of the DWPT system. The receiver footprint is an additional consideration with the footprint area A_{rx} is defined as:

$$A_{rx} = w_{rx}l_{rx} \quad (4.13)$$

where w_{rx} is the receiver width and l_{rx} is the receiver length.

4.2.1 Core Material Comparison

The following studies provide insight into the effects of different transmitter core materials by comparing optimization studies with Magment and non-magnetic transmitter cores. The receiver is assumed to be ferrite in both studies with a 26 cm gap between transmitter and receiver coils. Designs specified as Magment or no-core only refer to the transmitter material in this context. Fig. 4.2 presents the pareto fronts for the two studies with loss and volume objectives. It is seen that the no-core designs are smaller in volume, which is mostly due to the removal of the transmitter core. However, lower losses are seen in the Magment core designs.

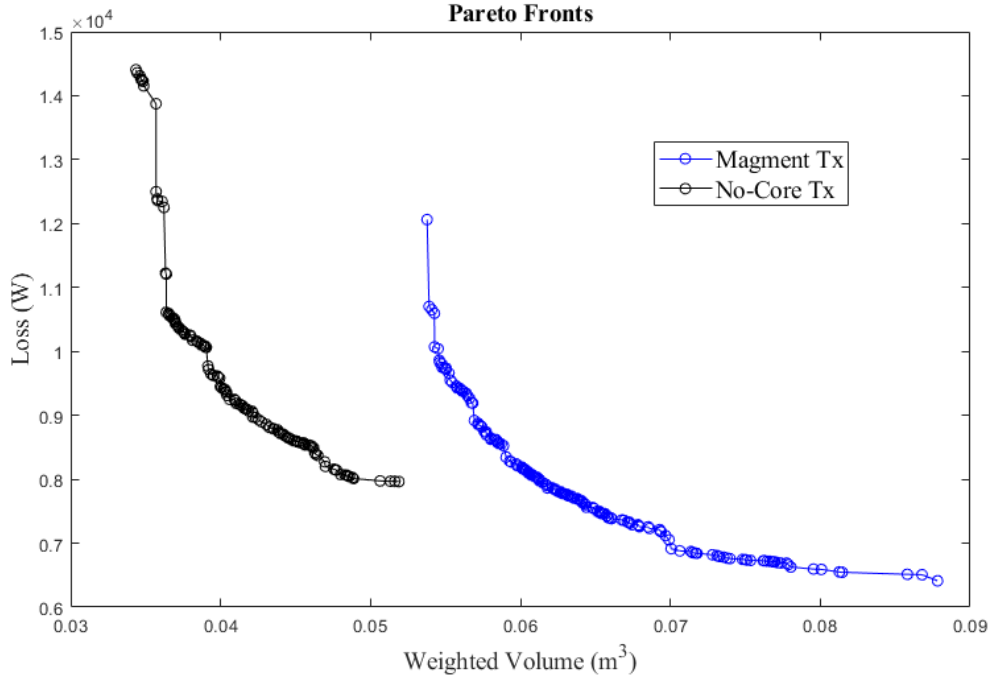


Figure 4.2: Core Material Comparison Pareto Fronts

When comparing the losses of the design fronts, further observations are made by viewing the coupling coefficients. The plot of coupling coefficient against system efficiency is shown in Fig. 4.3 for both studies, where it is seen that higher efficiency is correlated with higher coupling

factor. Among the core materials, the no-core coupling factors approach 0.16, while Magment designs surpass this noticeably to reach coupling factors above 0.2. Furthermore, Magment designs appear to be more efficient than no-core designs with the same coupling factor. In this regard, the benefits of the Magment in the transmitter are clear.

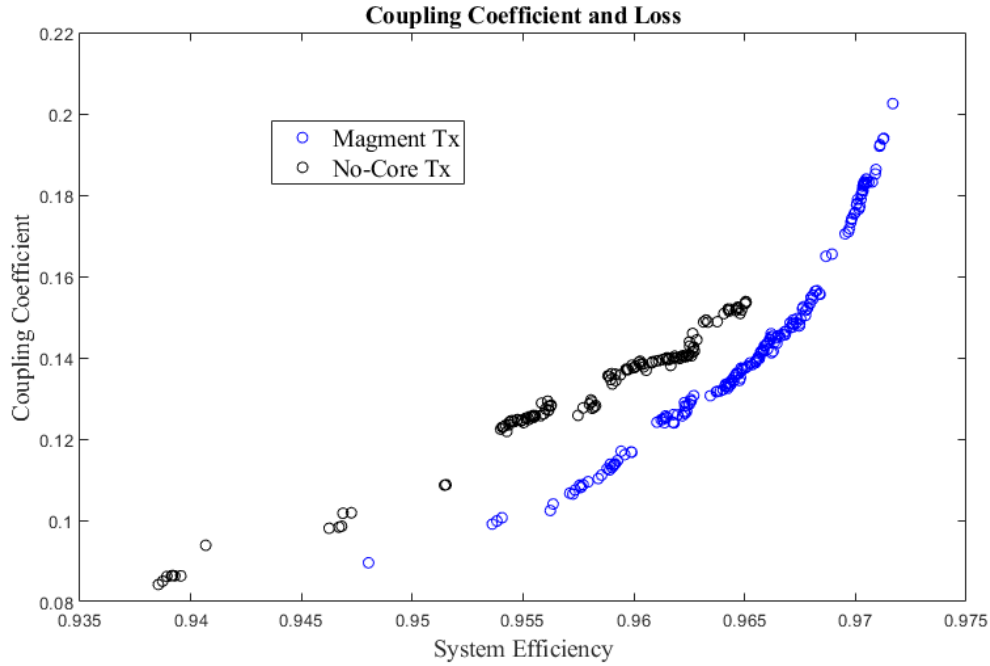


Figure 4.3: Core Material Comparison Coupling Coefficient and System Efficiency

With size and cost of the system being another concern, the receiver footprint is compared for the different materials. The plot of the receiver footprint area and system frequency is shown in Fig. 4.4, and as one might expect, there is a decrease in the receiver area as the frequency increases. In general, incorporating Magment into the transmitter allows for a smaller receiver footprint on the vehicle, which is favorable for potential consumers. It is noted that there are some smaller receiver footprints for the no-core transmitter designs; although, receiver footprint does not completely indicate the receiver volume which may be larger in those designs. Somewhat surprisingly, most of the Magment designs have a higher system frequency than the no-core designs.

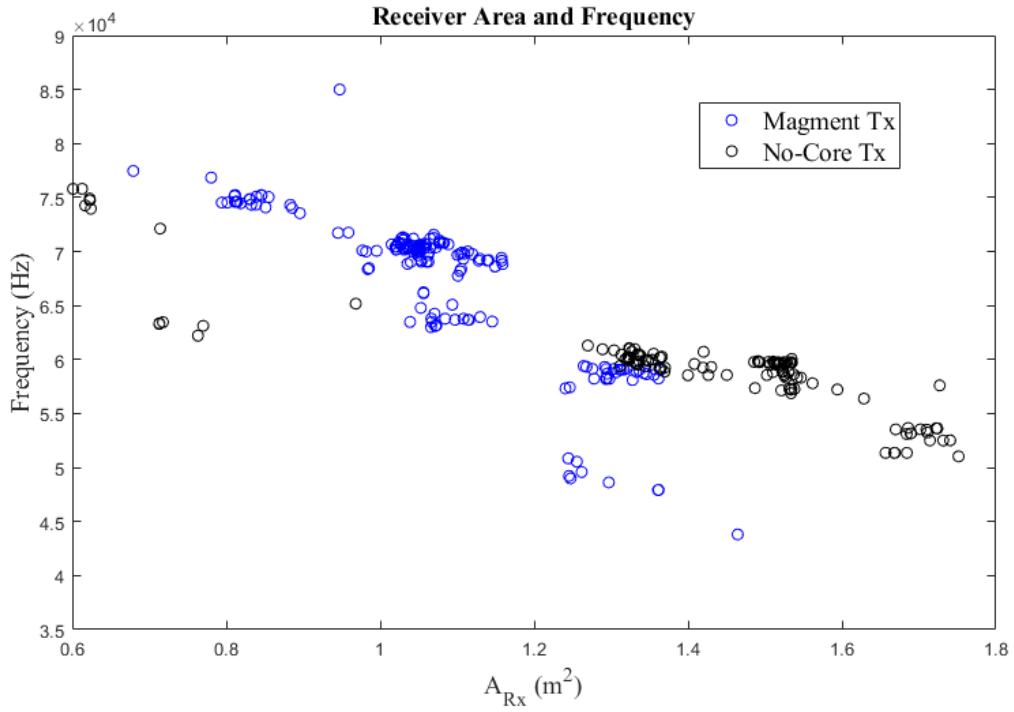


Figure 4.4: Core Material Comparison Reciever Footprint and Frequency

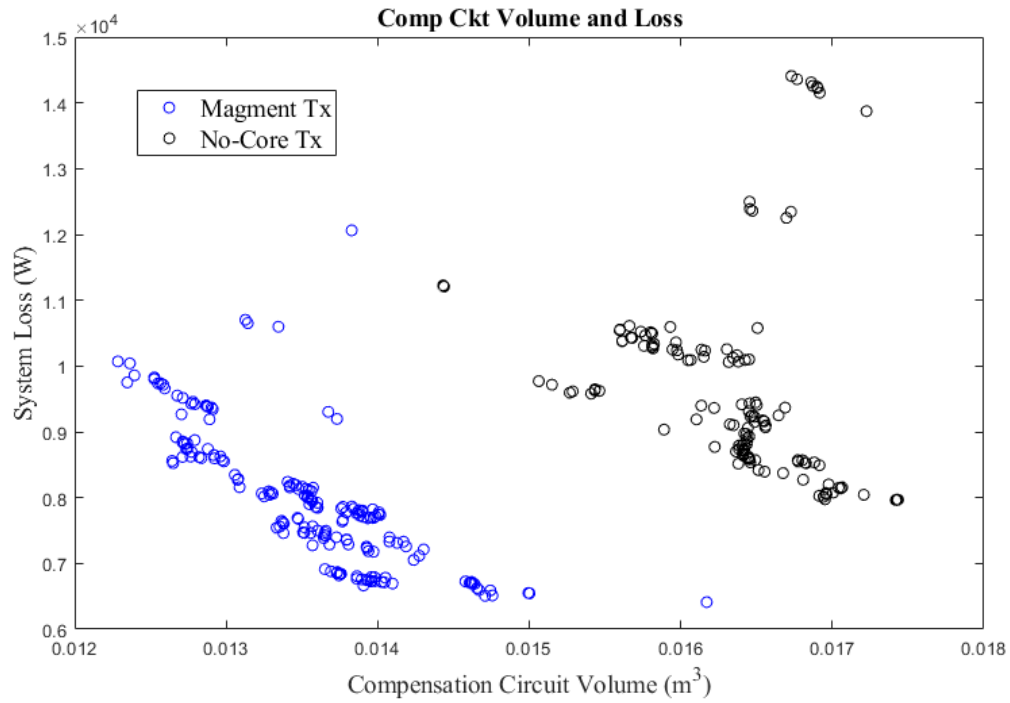


Figure 4.5: Core Material Comparison Compensation Circuit Volume

The compensation circuit components are another concern in regard to reducing system size, particularly on the vehicle, and a closer look is taken for the volume of the compensation circuit. Fig. 4.5 shows the plot of the compensation circuit volume and total system loss, where there is a moderate trade-off between those volumes and the system loss. While the pareto fronts showed a total volume improvement with the no-core transmitter, the compensation circuit volume is considerably smaller for Magment designs, which may facilitate the installation of the on-vehicle components for potential DWPT systems.

A final consideration is the volume of the transmitter and receiver windings. The plot of the winding volumes and coupling coefficients for both variations is shown in Fig. 4.6. A slight improvement in coupling factor is observed for increases in winding volume; however, there is a noticeable point of diminishing returns for the no-core transmitter winding. The no-core designs after that point have a significantly larger conductor volume than the Magment designs. Minimal differences in the receiver winding volume are seen among the two transmitter core materials.

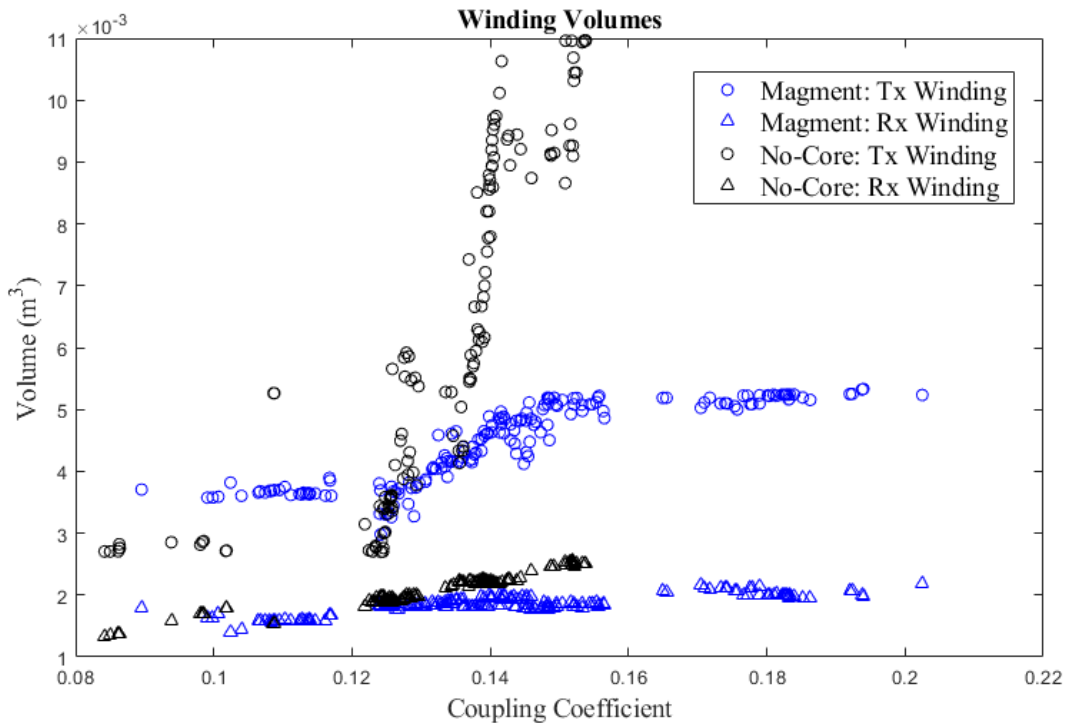


Figure 4.6: Core Material Comparison Winding Volumes

To better illustrate some of the trade-offs between Magment and no-core transmitters in DWPT systems, a sample design from each study is analyzed. Designs with similar losses were selected, specifically for a total system loss of 9.5 kW in this comparison. The geometry of the transmitter and receiver is depicted in Fig. 4.7 for the Magment transmitter and in Fig. 4.8 for the non-magnetic transmitter core, with the unit of the shown dimensions in meters. For the latter, it is noted that the outline of the transmitter core is shown although its geometry does not affect the design other than determining the conductor placement. The no-core transmitter is substantially wider than the Magment transmitter, and to a lesser extent, the same is true for the receivers.

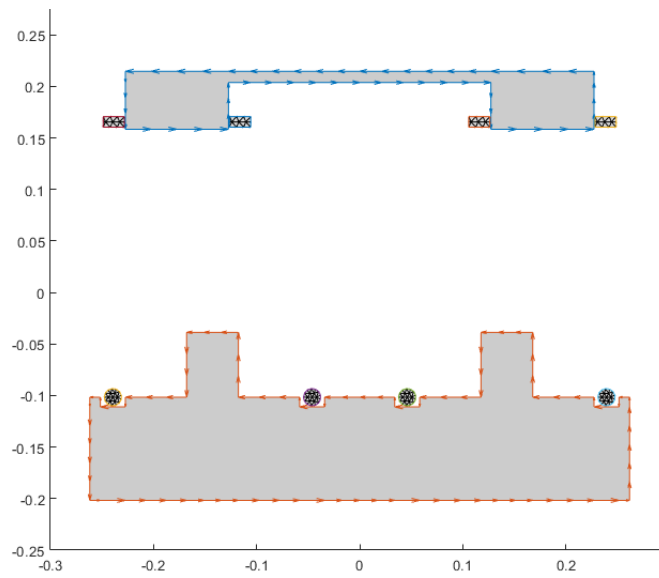


Figure 4.7: Sample Design with Magment Transmitter

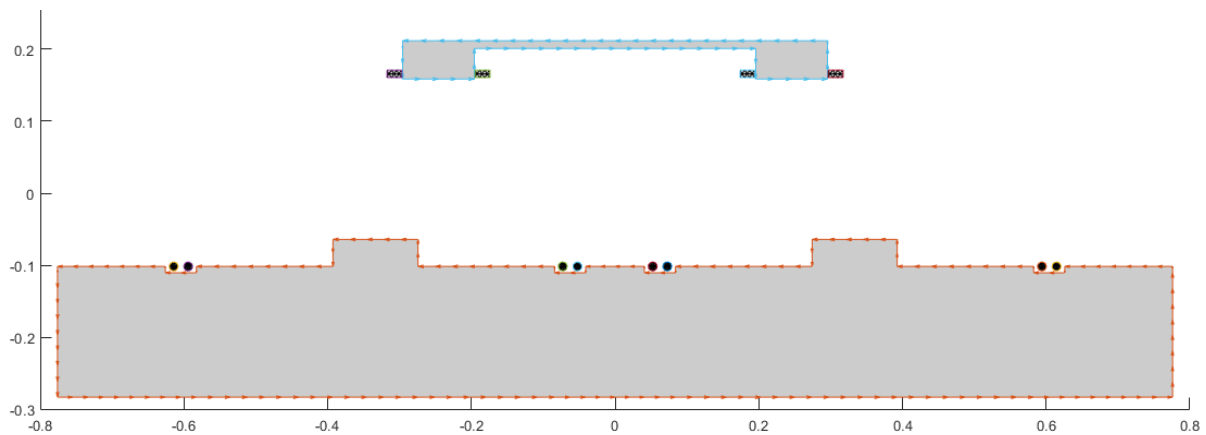


Figure 4.8: Sample Design with Non-Magnetic Transmitter

The genes for each design are listed in Table 4.4. As previously seen in Fig. 4.7 and Fig. 4.8, the genes for the transmitter and receiver core widths are larger in the no-core design. Additionally, the length of the receiver is around 0.8 m longer for the no-core design, and there is an added turn on the no-core transmitter. Electrically, the Magment design operates at a frequency almost 20 kHz higher and with a transmitter current over 100 A greater than the no-core design. A lower rectifier voltage is also seen in the Magment design.

Table 4.4: Material Comparison Sample Design Genes

Gene	Magment Transmitter	Non-Magnetic Transmitter
hb_{tx}	0.1001 m	0.1814 m
ws_{tx}	0.0629 m	0.0374 m
hs_{tx}	0.0501 m	0.1183 m
$sratio$	1.1183 m	1.4226
sep_{tx}	0.0594 m	0.1900 m
$csep_{tx}$	0.0102 m	0.1500 m
$dsep_{tx}$	0.0680 m	0.0818 m
N_{tx}	1	2
wb_{rx}	0.2546 m	0.3915 m
hb_{rx}	0.0109 m	0.0108 m
wt_{rx}	0.0999 m	0.0999 m
ht_{rx}	0.0552 m	0.05212m
Nh_{rx}	2	2
Nv_{rx}	1	1
l_{rx}	1.8275 m	2.5941 m
f	74858 Hz	56877 Hz
I_{tx}	400 A	293.06 A
di_{tx}	0.0168 m	0.0123 m
di_{rx}	0.0100 m	0.0101 m
N_{inv}	2	2
N_{rec}	1	1
V_{rec}	564.49 V	641.32 V

The total system loss is roughly the same between designs, but the breakdown of the loss among all components is shown in Table 4.5. Although core loss is not a factor in the no-core transmitter, there is a rather large increase in the winding loss from the Magment transmitter.

Despite the lower transmitter current, the added resistance caused by the extra turns and wider conductor positioning leads to higher conduction loss. Another discrepancy is seen in the loss in the C_2 capacitors, where it is significantly higher for the Magment design. In contrast, the C_1 and L_{f1} losses are lower in the Magment design. The losses in the remaining components are within a similar range for both designs.

Table 4.5: Sample Design Component Losses

Component Loss	Magment Transmitter	Non-Magnetic Transmitter
Inverter (W)	915.20	891.13
L_{f1} (W)	850.31	1050.50
C_{f1} (W)	74.89	66.53
C_1 (W)	1554.80	1735.70
Tx Winding (W)	916.21	1450.00
Tx Core (W)	252.75	0
Rx Core (W)	50.73	150.55
Rx Winding (W)	1090.60	1147.30
C_2 (W)	1434.30	811.84
C_{f2} (W)	76.83	76.99
L_{f2} (W)	1106.40	1016.10
Rectifier (W)	1193.10	1050.10

Looking at the volumes of each component, listed in Table 4.6, a main difference is the larger receiver volume for the no-core design. Similarly, the transmitter and receiver windings are larger for the no-core system. It is noted that the transmitter core volume is not compared since it can be ignored for the no-core design. For the remaining components, the power electronic and total capacitor volumes are comparable between designs, but smaller compensation circuit inductors can be utilized in the Magment design.

Table 4.6: Sample Design Component Volumes

Component Volume	Magment Transmitter	Non-Magnetic Transmitter
Inverter (m ³)	9.31×10-3	1.05×10-2
L_{f1} (m ³)	2.44×10-3	4.39×10-3
C_{f1} (m ³)	6.52×10-4	7.61×10-4
C_1 (m ³)	3.26×10-3	3.91×10-3
Tx Winding (m ³)	3.62×10-3	4.13 ×10-3
Tx Core (m ³)	2.28 ×10-1	1.14
Rx Core (m ³)	2.57 ×10-2	3.85 ×10-2
Rx Winding (m ³)	1.58 ×10-3	2.23 ×10-3
C_2 (m ³)	3.26 ×10-3	2.61 ×10-3
C_{f2} (m ³)	6.52 ×10-4	6.52 ×10-4
L_{f2} (m ³)	2.44 ×10-3	4.17 ×10-3
Rectifier (m ³)	2.84 ×10-3	2.84 ×10-3

Continuing to the DWPT circuit values, listed in Table 4.7, it can be seen that the transmitter/receiver inductances are actually higher in the no-core design. Despite this, the coupling factor is still higher for the Magment design at 0.14 compared to 0.11 in the no-core design. A side-effect of the higher transmitter/receiver inductances is higher compensation inductances, which is a primary cause of the larger L_{f1} and L_{f2} volumes seen in the no-core designs.

Table 4.7: Sample Design Compensation Circuit Values

Component	Magment Transmitter	Non-Magnetic Transmitter
L_{f1}	3.10 μ H	5.571 μ H
C_{f1}	1.458 μ F	1.406 μ F
C_1	0.1823 μ F	0.1385 μ F
L_{tx}	27.89 μ H	62.12 μ H
L_m	3.403 μ H	7.006 μ H
L_{rx}	33.61 μ H	43.01 μ H
C_2	0.1519 μ F	0.2151 μ F
C_{f2}	1.467 μ F	1.483 μ F
L_{f2}	3.081 μ H	5.281 μ H

A final comparison of designs is shown in Table 4.8, which lists the expected voltages and currents of a handful of system components. Because the inverter voltage is the same in both designs, I_{Lf1} is also the same. Across the system, lower voltage and higher currents are observed in the Magment design, which is favorable from a safety perspective. Typically, the higher currents might be concerning due to the incurred loss and temperature increases, but the total loss is the same with the same thermal constraints imposed on both systems.

Table 4.8: Sample Design Voltage and Current Ratings

Rating	Magment Transmitter	Non-Magnetic Transmitter
I_{Lf1} rms (A)	384.79	384.79
I_{tx} rms (A)	400.00	293.06
I_{Cf1} rms (A)	555.03	483.68
V_{Cf1} peak (V)	1144.80	1361.70
I_{Lf2} rms (A)	441.72	388.80
I_{rx} rms (A)	350.67	305.93
I_{Cf1} rms (A)	563.99	494.73
V_{Cf1} peak (V)	1156.00	1320.50

4.2.2 Gap Distance Comparison

To view the effects of different gap sizes in the DWPT system, the results from additional optimization studies are discussed, wherein systems with a 26 cm gap and an 18 cm gap are designed. In both studies, the transmitter is composed of Magment with the receiver composed of ferrite. Fig. 4.9 presents the pareto fronts for the two studies, which plots the loss and volume objectives. Lower losses and lower volumes are found in the 18 cm gap designs, although the loss improvement is less than in the transmitter material comparisons.

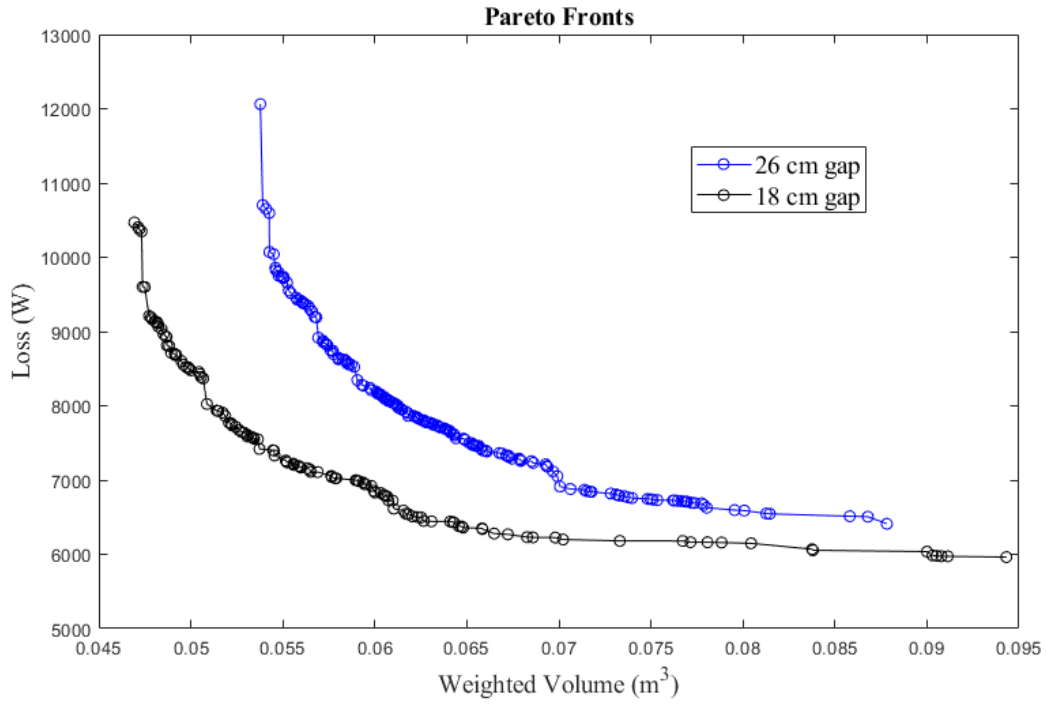


Figure 4.9: Gap Size Comparison Pareto Fronts

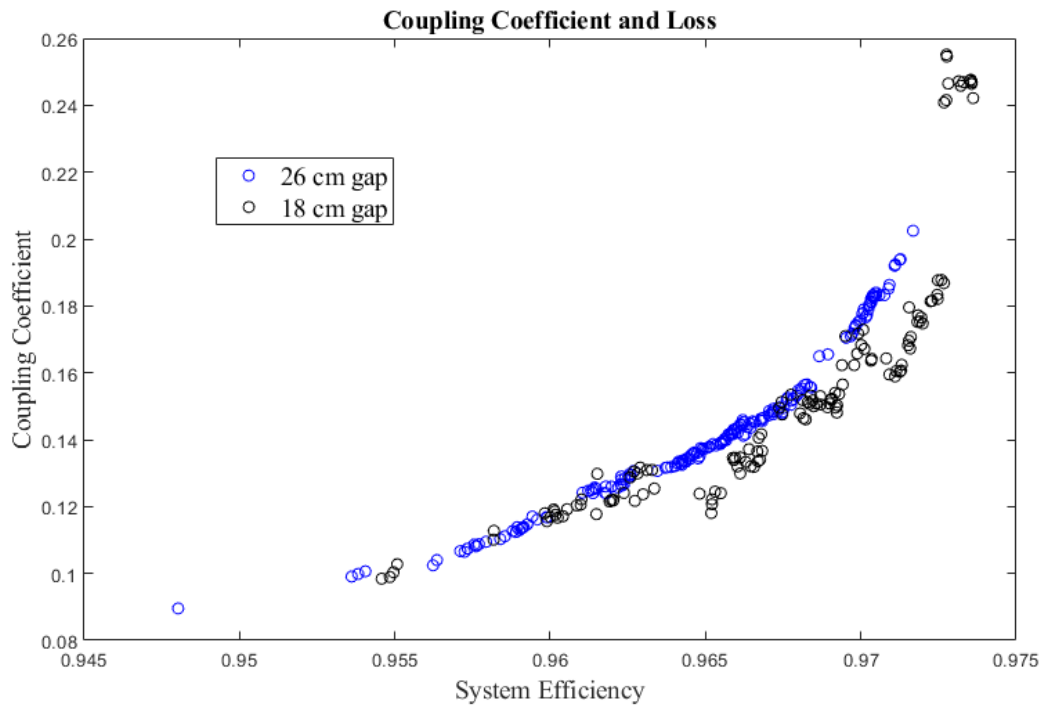


Figure 4.10: Gap Size Comparison Coupling Coefficient and Efficiency

Gap size can have a direct impact on the coupling coefficients, and Fig. 4.10 shows the plots of the coupling coefficients and system efficiency for both gap sizes. As noted previously, higher efficiency is possible with higher coupling factor, and the 18 cm gap designs have slightly better efficiencies than the 26 cm designs at the same coupling factor. Furthermore, the coupling factor in the 18 cm gap rises above 0.25, improving on the peak coupling factor around 0.2 from the 26 cm gap systems.

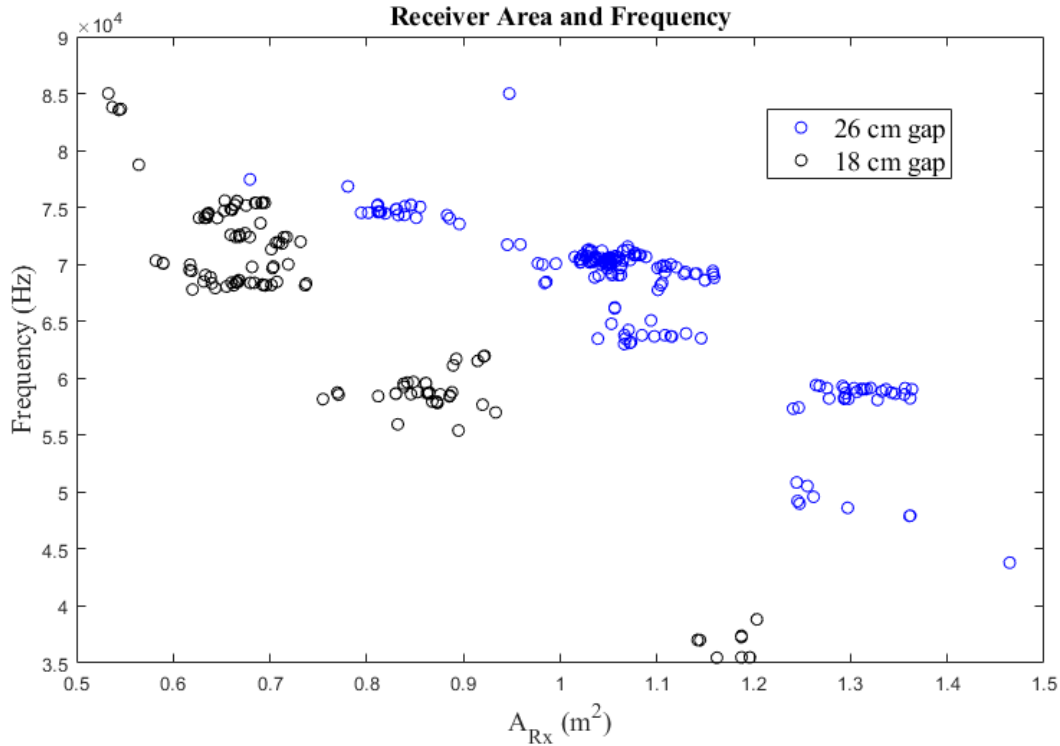


Figure 4.11: Gap Size Comparison Receiver Footprint and Frequency

Examining the effects on the receiver footprint, which is plotted along with the frequency in Fig. 4.11 it is seen that smaller receiver footprints are feasible in the 18 cm gap designs. The previously discussed trade-off of increased frequency and decreased size is also seen in these studies, however to greater effect in the 18 cm gap designs. While the system frequencies are generally in the same range for both studies, a handful of 18 cm gap designs use frequencies below 40 kHz, which is lower than any of the 26 cm gap designs. The smaller receiver footprint and potentially lower system frequencies may make smaller gap DWPT systems easier to implement.

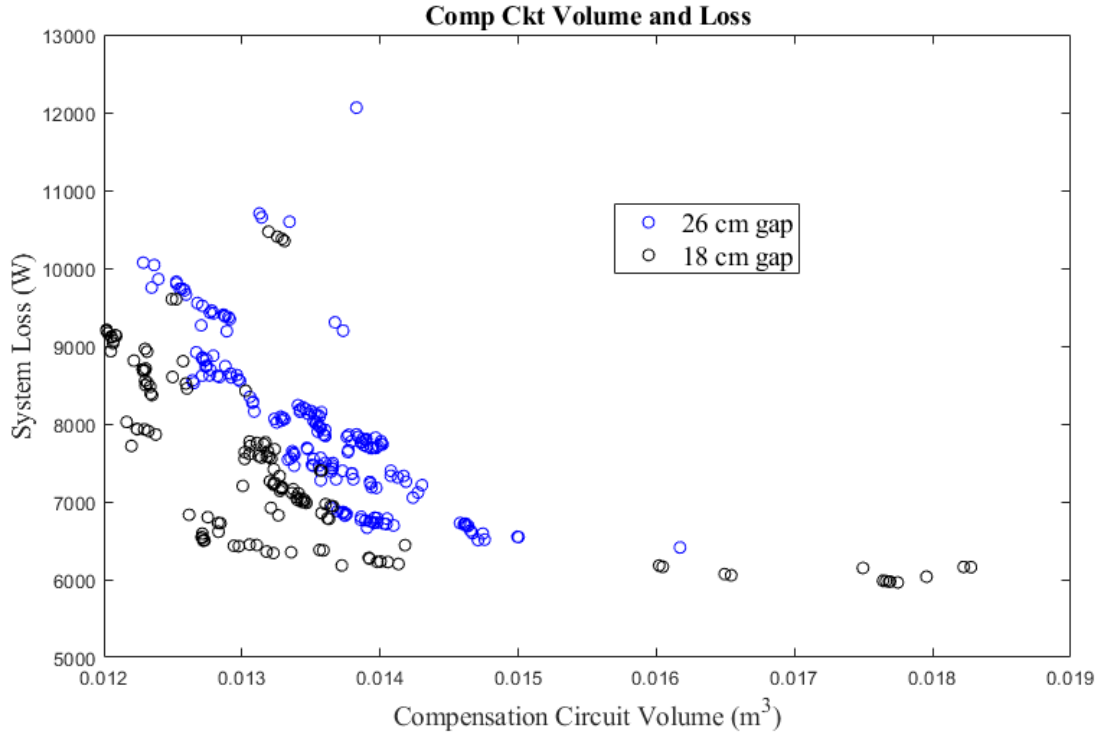


Figure 4.12: Gap Size Comparison Compensation Circuit Volumes

For a further size comparison, the volumes of the compensation circuit are plotted with the system loss in Fig. 4.12. There isn't an appreciable difference in total compensation circuit volume among the gap variations. Although several of the 18 cm gap designs surpass the normal compensation circuit size range, this is not likely to be problematic due to the smaller system volume of the 18 cm gap designs.

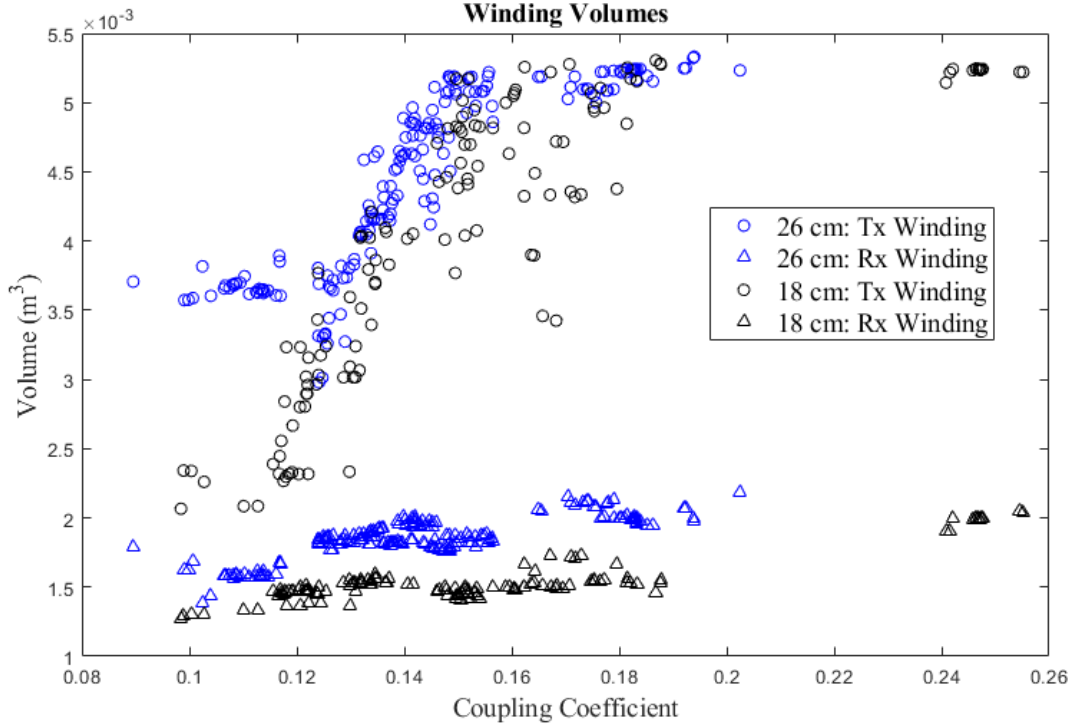


Figure 4.13: Gap Size Comparison Winding Volumes

The size of the windings is also considered for both gap sizes, with the transmitter and receiver conductor volumes plotted with the coupling coefficient for the two studies in Fig. 4.13. Less conductor volume is typically needed for both the transmitter and receiver in the 18 cm gap systems, but there is not a prominent difference in volume across both sets of designs.

As with the material comparison studies, a sample design from each gap size study is selected and dissected to better view differences among the gap variations. Designs with system loss around 7 kW were selected. The transmitter and receiver geometries are depicted in Fig. 4.14 for the 18 cm gap system and in Fig. 4.15 for the 26 cm gap system. One immediate observation is the suppression of the transmitter stubs on the 18 cm gap design, whereas the 26 cm gap transmitter utilizes the full possible height of the stubs. This may be explained by a diminishing trade-off between volume and loss in the 18 cm gap study, wherein the decrease in volume from removing the transmitter stubs is more valuable than the added coupling and therefore increased efficiency from expressing the transmitter teeth. The only other notable difference is the wider design of the transmitter and receiver in the 26 cm gap system.

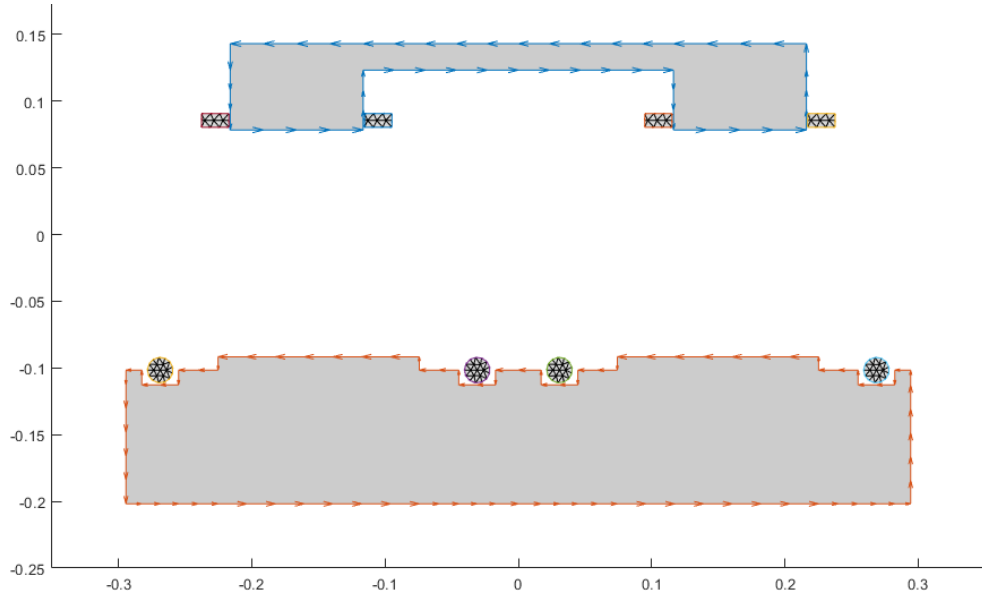


Figure 4.14: Sample Design with 18 cm Gap

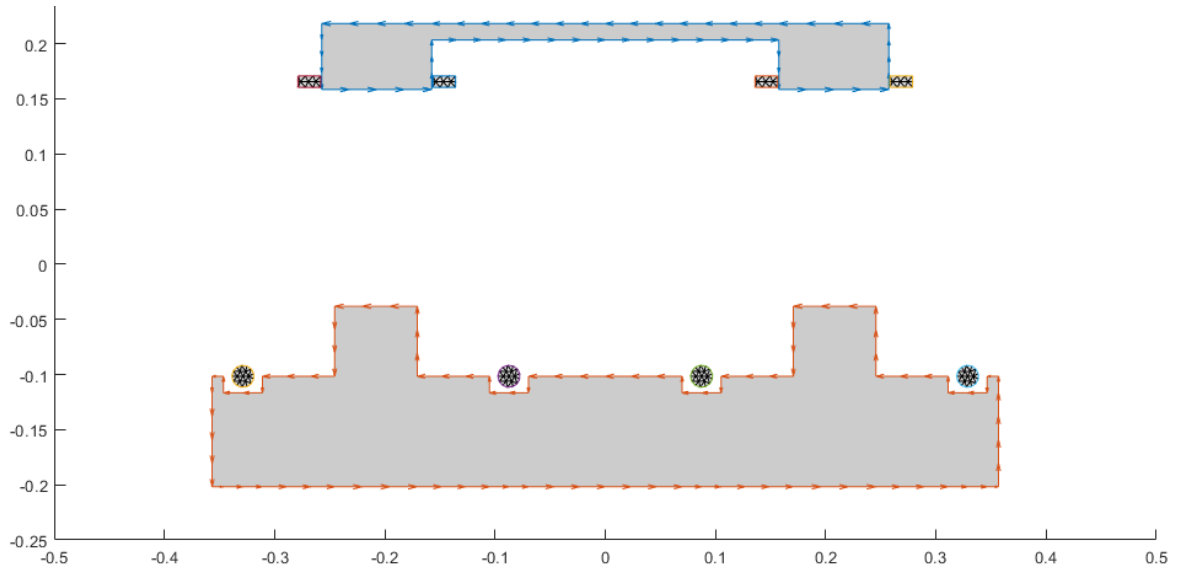


Figure 4.15: Sample Design with 26 cm Gap

The genes for the two systems are listed in Table 4.9. It is seen that the genes that determine core width are larger in the 26 cm gap design, and the receiver is also significantly longer. Electrically, a higher frequency is selected in the 18 cm gap design, with a slightly lower transmitter current and higher rectifier voltage.

Table 4.9: Gap Size Comparison Sample Design Genes

Gene	18 cm Gap	26 cm Gap
hb_{tx}	0.1002 m	0.1002 m
ws_{tx}	0.0100 m	0.0635 m
hs_{tx}	0.151 m	0.0749 m
s_{ratio}	1.152	1.500
sep_{tx}	0.0297 m	0.0655 m
$csep_{tx}$	0.0119 m	0.0103 m
$dsep_{tx}$	0.0342 m	0.1395 m
N_{tx}	1	1
wb_{rx}	0.2328 m	0.3151 m
hb_{rx}	0.0198 m	0.0148 m
wt_{rx}	0.0997 m	0.0999 m
ht_{rx}	0.0637 m	0.0588 m
Nh_{rx}	2	2
Nv_{rx}	1	1
l_{rx}	1.627 m	2.409 m
f	69813 Hz	57329 Hz
I_{tx}	354.06 A	375.6 A
di_{tx}	0.0192 m	0.0199 m
di_{rx}	0.01 m	0.01 m
N_{inv}	2	2
N_{rec}	1	1
V_{rec}	675.34 V	657.93 V

The loss in each component is broken down in Table 4.10 where it is seen that the loss distribution among components is nearly the same between the designs. The noticeable differences occur with the C_1 loss, which is greater in the 18 cm gap design partially due to the increased transmitter current, and with the receiver winding loss, which is over 300 W higher in the 26 cm gap design.

Table 4.10: Gap Size Comparison Component Losses

Component Loss	18 cm Gap	26 cm Gap
Inverter (W)	889.84	875.22
L_{f1} (W)	935.07	821.82
C_{f1} (W)	64.362	64.159
C_1 (W)	859.47	642.34
Tx Winding (W)	566.92	598.44
Tx Core (W)	131.43	143.22
Rx Core (W)	79.828	23.85
Rx Winding (W)	681.36	986.07
C_2 (W)	638.74	768.57
C_{f2} (W)	65.887	66.276
L_{f2} (W)	1088.3	1038.7
Rectifier (W)	997.23	1023.6

As with the losses, the volumes for each component are fairly similar between designs, as shown in Table 4.11. The primary discrepancies are in the transmitter and receiver volumes, which are larger in all aspects for the 26 cm gap design. The compensation inductor volumes are also larger in the 26 cm gap design, but to a lesser extent than the transmitter and receiver volumes. As noted in Fig. 4.12, there isn't that pronounced of a difference in the compensation circuit volumes among the gap size variations.

Table 4.11: Gap Size Comparison Component Volumes

Component Volume	18 cm Gap	26 cm Gap
Inverter (m^3)	9.571×10^{-3}	1.042×10^{-2}
L_{f1} (m^3)	2.962×10^{-3}	3.400×10^{-3}
C_{f1} (m^3)	7.610×10^{-4}	7.610×10^{-4}
C_1 (m^3)	2.609×10^{-3}	2.283×10^{-3}
Tx Winding (m^3)	4.826×10^{-3}	5.188×10^{-3}
Tx Core (m^3)	2.402×10^{-1}	3.118×10^{-1}
Rx Core (m^3)	2.852×10^{-2}	4.006×10^{-2}
Rx Winding (m^3)	1.415×10^{-3}	2.048×10^{-3}
C_2 (m^3)	2.609×10^{-3}	2.609×10^{-3}
C_{f2} (m^3)	7.610×10^{-4}	7.610×10^{-4}
L_{f2} (m^3)	3.732×10^{-3}	4.423×10^{-3}
Rectifier (m^3)	2.836×10^{-3}	2.836×10^{-3}

The values of all DWPT circuit components are listed in Table 4.12. The transmitter self-inductance is shockingly similar between designs, but the receiver self-inductance is higher in the 26 cm gap design due to the longer core. Despite this, the coupling factor is higher for the 18 cm gap design. It is also observed that the L_{f1} and L_{f2} values are larger in the 26 cm gap designs, which is the principal cause for their larger volumes.

Table 4.12: Gap Size Comparison Compensation Circuit Component Values

Component	18 cm Gap	26 cm Gap
L_{f1} (μH)	3.76 μH	4.31 μH
C_{f1} (μF)	1.38 μF	1.79 μF
C_1 (μF)	0.222 μF	0.348 μF
L_{tx} (μH)	27.2 μH	26.4 μH
L_m (μH)	4.94 μH	5.66 μH
L_{rx} (μH)	31.5 μH	44.3 μH
C_2 (μF)	0.204 μF	0.207 μF
C_{f2} (μF)	1.10 μF	1.37 μF
L_{f2} (μH)	4.74 μH	5.61 μH

A final inspection of the expected currents and voltages is provided in Table 4.13 for both designs. The fixed inverter voltage causes the designs to have the same L_{f1} current. There is very little disparity between the currents and voltages of the two designs across all system components. In general, there is slightly higher current and lower voltage in the 18 cm gap design, but these differences are minimal and likely hold little influence on choosing one gap size over another.

Table 4.13: Gap Size Comparison Voltage and Current Ratings

Rating	18 cm Gap	26 cm Gap
I_{Lf1} rms (A)	384.79	384.79
I_{tx} rms (A)	354.06	375.60
I_{Cf1} rms (A)	522.9	537.72
V_{Cf1} peak (V)	1218.5	1181.20
I_{Lf2} rms (A)	369.21	378.99
I_{rx} rms (A)	292.52	292.99
I_{Cf1} rms (A)	471.05	479.04
V_{Cf1} peak (V)	1384.70	1369.60

5. SYSTEM VALIDATION

To assess the inductance and capacitance characteristics of the DWPT system in a realistic setting, a three-phase topology system is evaluated within the expected laboratory layout. The selected design is determined through a multiple step optimization process established by [5] and involving the optimization process outlined in Chapter 5. The cross-section of this design's transmitter and receiver are presented in Fig. 5.1.

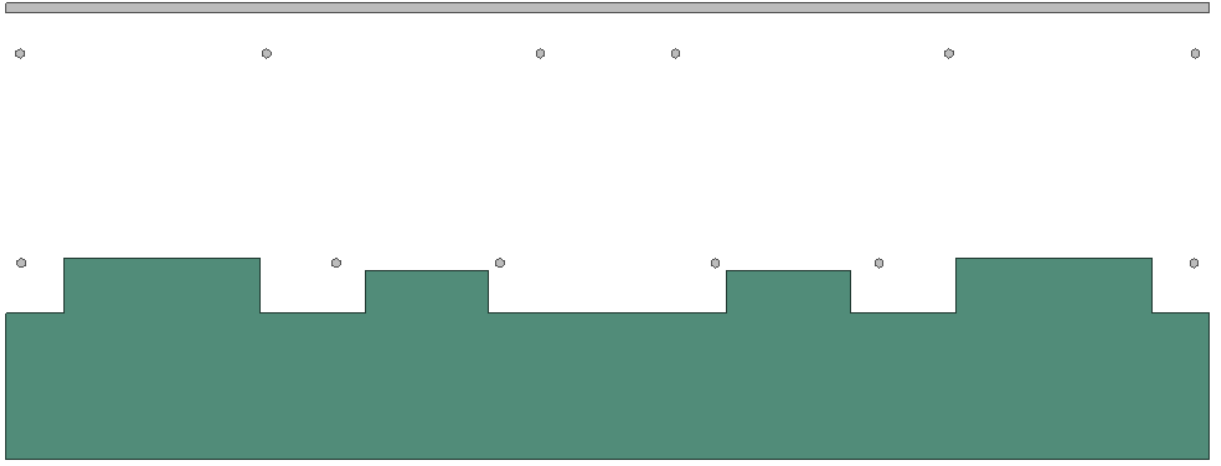


Figure 5.1: Transmitter and Receiver for System Validation

The physical parameters for the design are listed in Table 5.1. It is noted that the xi_{tx} and xi_{rx} parameters are the distance from the center to the conductor in each slot, and they derived from the parameters listed in Table 2.2. Similarly, the receiver does not have teeth, so just the width of the core base wb_{rx} is listed for simplicity. The parameters y_{tx} and y_{rx} denote the distance of the conductors from the road surface.

Table 5.1: Transmitter and Receiver Physical Design Parameters

a) Transmitter Parameters

Parameter	Value
hb_{tx}	0.1469 m
$wt1_{tx}$	0.1800 m
$wt2_{tx}$	0.1248 m
$wt3_{tx}$	0.1984 m
$wt4_{tx}$	0.0102 m
$ht1_{tx}$	0 m
$ht2_{tx}$	0.0436 m
$ht3_{tx}$	0.0563 m
$ht4_{tx}$	0 m
$ws1_{tx}$	0.0301 m
$ws2_{tx}$	0.1062 m
$ws3_{tx}$	0.0481 m
$x1_{tx}$	0.1088 m
$x2_{tx}$	0.2742 m
$x3_{tx}$	0.5921 m
y_{tx}	-0.0562 m
dia_{tx}	0.0095 m
l_{tx}	3.6576 m

b) Receiver Parameters

Parameter	Value
hb_{rx}	0.01 m
wb_{rx}	1.2161 m
$x1_{rx}$	0.0683 m
$x2_{rx}$	0.3446 m
$x3_{rx}$	0.5935 m
y_{rx}	0.1554 m
dia_{rx}	0.0095 m
l_{rx}	1.6202 m

The proposed capacitor layouts for the system are pictured for C_1 and C_{f1} in Fig. 5.2 and for C_2 and C_{f2} in Fig. 5.3, where the C_{f1} and C_{f2} capacitors are colored blue and C_1 and C_2 colored green. The capacitors on either transmitter or receiver side are grouped together to reduce the size of the system layout and to reduce the number of enclosures. The size of each enclosure is listed in Table 5.2, along with the number of individual capacitors that compose each component.

Table 5.2: Capacitor Physical Layout Parameters

Parameter	C_1, C_{f1} Enclosure	C_2, C_{f2} Enclosure
Height	4 in.	4 in.
Width	24 in.	24 in.
Length	18 in.	12 in.
C_1/C_2 Number of Capacitors	6	6
C_{f1}/C_{f2} Number of Capacitors	12	6

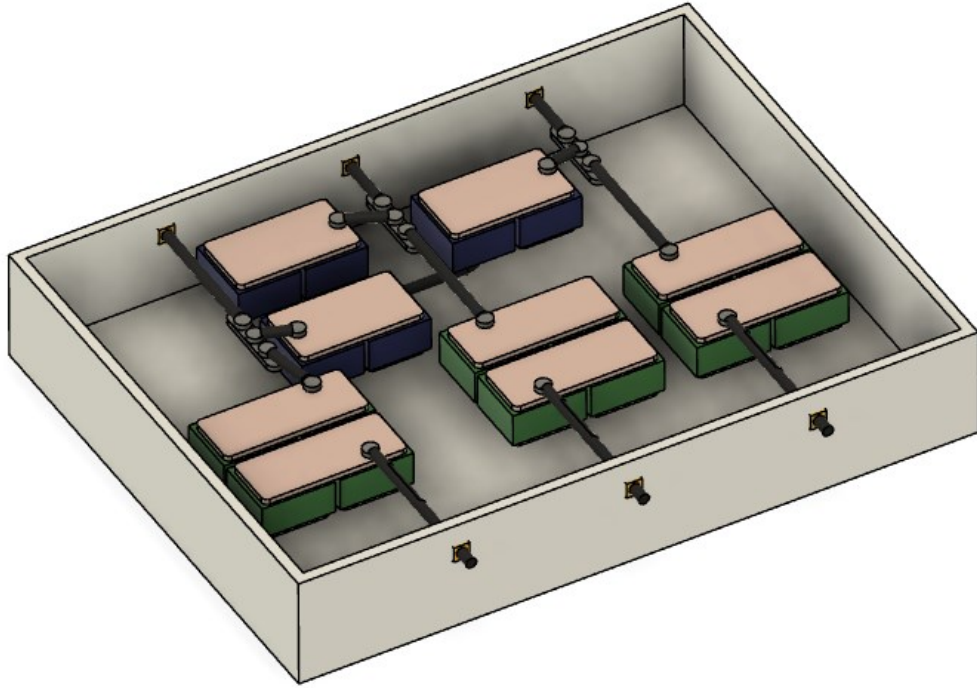


Figure 5.2: C_1 and C_{f1} Enclosure

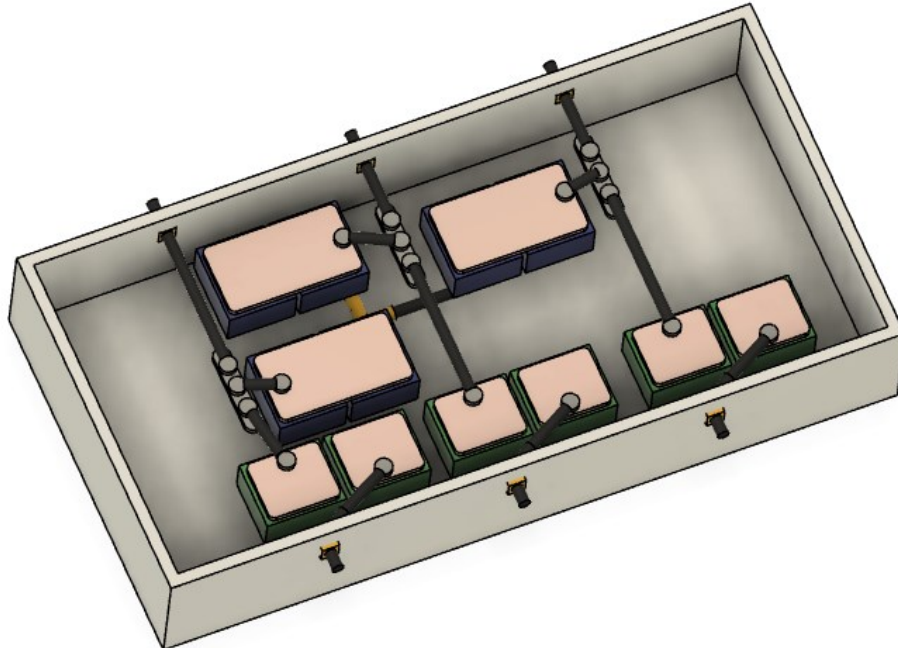


Figure 5.3: C_2 and C_{f2} Enclosure

The dimensions for the compensation inductors are listed in Table 5.3. It is noted that the same size inductor is used for both L_{f1} and L_{f2} , so only one set of dimensions is listed. The inductors for each phase are placed directly next to each other in the same orientation.

Table 5.3: Compensation Inductors Physical Parameters

Parameter	Value
Length	1.022 m
Core Outer Diameter	0.068 m
Core Inner Diameter	0.036 m

With the physical dimensions of the components for this DWPT system established, the layout of the system can be determined. The prospective placement of the components in the lab environment is depicted in Fig. 5.4. On the transmitter side, the compensation circuit components are placed on a neighboring bench, and the transmitter winding is extended from those components to reach the transmitter core which rests on the floor. The receiver is lifted by a wooden support structure with the receiver side components placed above the receiver core. Only the components between the inverter and rectifier are considered in this evaluation.

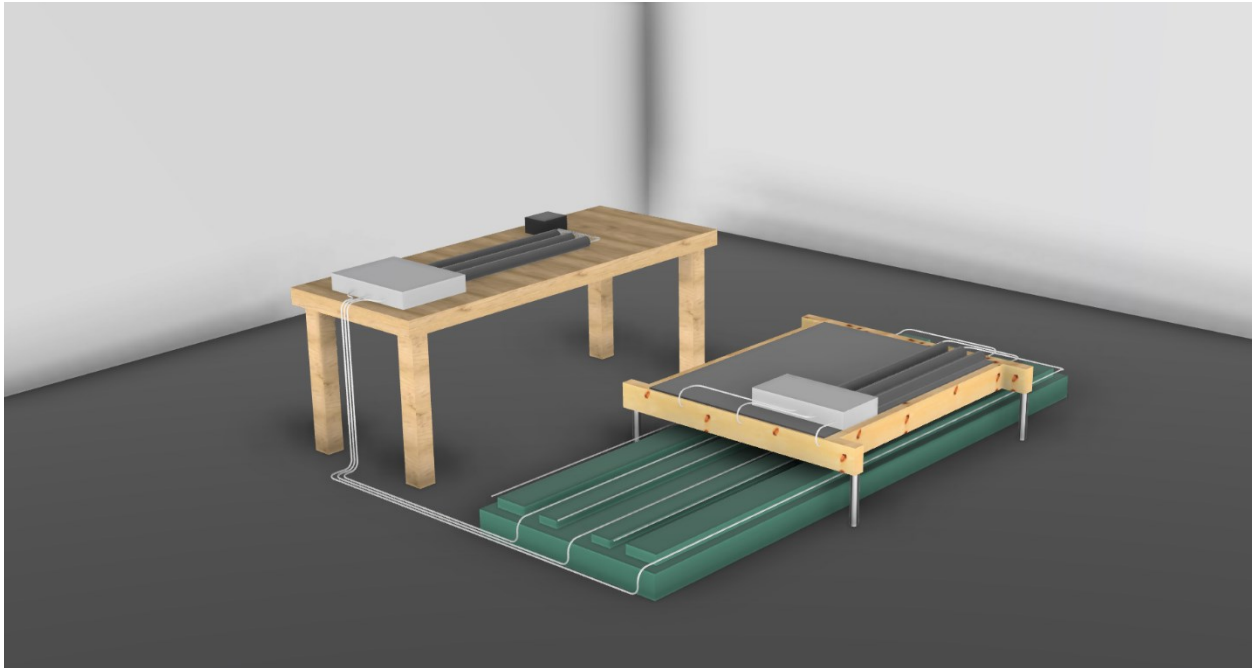


Figure 5.4: Prospective DWPT System Layout

5.1 System Simulations

To analyze the DWPT system in the proposed layout, simulations in Ansys Maxwell were created. The Q3D Extractor solution type was used, which computes the inductance and capacitance of the model through a combination of FEM and BEM. As described in [21], the Q3D Extractor solves Maxwell's equations in the frequency domain and involves a quasi-static approximation in which displacement currents are ignored. The settings for Capacitance and AC Inductance calculations are shown in Figs. 5.5a and 5.5b, with the solution frequency at 40 kHz. Multiple models of the DWPT system were analyzed which include the full system, the isolated transmitter and receiver, the transmitter and receiver with additional connections, and the compensation inductors. Since it is very difficult to model the compensation capacitors in this setting, they are not directly included in the Q3D simulations, and only the volume of their enclosure is accounted for.

The screenshot shows the 'Solver Settings' and 'Adaptive Solution' panels for a capacitance calculation. In the 'Solver Settings' panel, 'Automatically increase solution order' is checked, 'Solution Order' is set to 'High', 'Iterative Solver' is selected, 'Direct Solver' is unselected, and 'Compression Tolerance' is '1e-06'. In the 'Adaptive Solution' panel, the 'Maximum Number of Passes' is 20, 'Minimum Number of Passes' is 2, 'Minimum Converged Passes' is 2, 'Percent Error' is 1%, and 'Percent Refinement Per Pass' is 30%.

Parameter	Value
Maximum Number of Passes	20
Minimum Number of Passes	2
Minimum Converged Passes	2
Percent Error	1 %
Percent Refinement Per Pass	30 %

a) Capacitance Settings

The screenshot shows the 'Adaptive Solution' panel for an AC inductance calculation. The 'Maximum Number of Passes' is 20, 'Minimum Number of Passes' is 2, 'Minimum Converged Passes' is 2, 'Percent Error' is 1%, and 'Percent Refinement Per Pass' is 30%.

Parameter	Value
Maximum Number of Passes	20
Minimum Number of Passes	2
Minimum Converged Passes	2
Percent Error	1 %
Percent Refinement Per Pass	30 %

b) AC Inductance Settings

Figure 5.5: Q3D Solution Settings

5.1.1 Full System Simulation

The first model that is evaluated is the full system layout, which contains the compensation circuit inductors, the transmitter and receiver, and additional connections between the components that includes space for the compensation circuit capacitor enclosures. The model

used in Ansys is shown in Fig. 5.6. Although the system model depicts the transmitter and receiver connected directly in series with their respective compensation inductors, which is not accurate to the DWPT circuit, the full system simulation provides insight into potential parasitic capacitances and inductances that may occur due to the placement of some components.

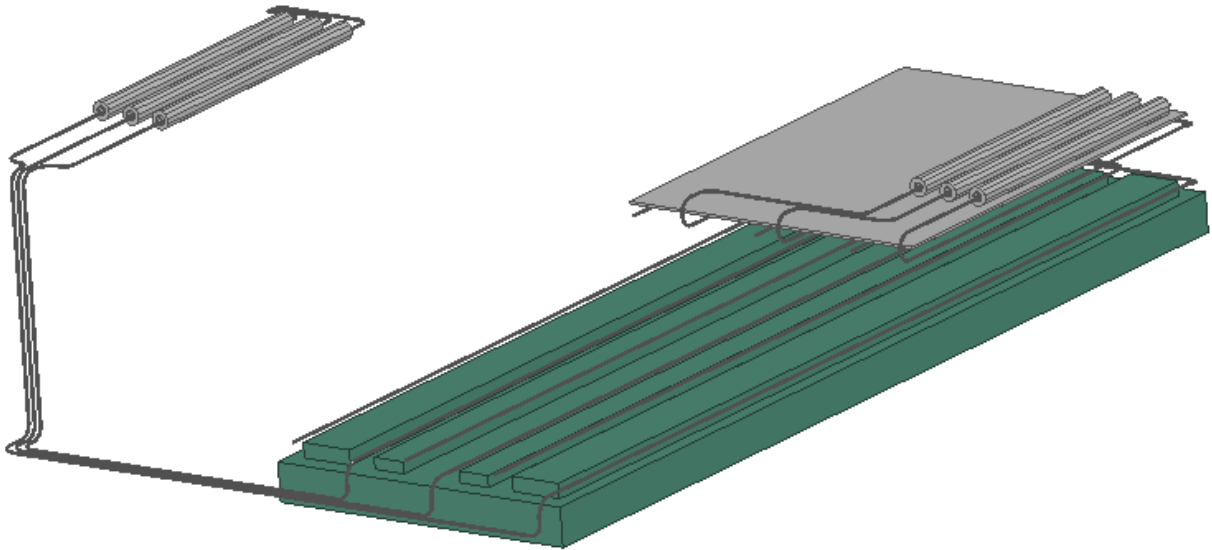


Figure 5.6: Q3D Model of Full System

The capacitance matrices calculated by the system simulation are shown in Tables 5.4a-5.4c. All capacitance values determined by the simulation are below 1 nF, which is negligible compared to the values of the compensation circuit capacitors. It is clear that there is no concern over parasitic capacitances between the conductors in this layout, and because the capacitance is so insignificant, it is not discussed in the proceeding models. However, it is noted that this simulation determines the capacitance between each of the transmitter and receiver phase conductors, which is not necessarily indicative of the parasitic capacitance to any external electrical grounds that may be present in the environment of an actualized DWPT system.

Table 5.4: DWPT System Capacitance Matrices

a) Tx Side Capacitances				b) Rx Side Capacitances			
	a	b	c		a	b	c
a	188.09 pF	-106.76 pF	-92.46 pF	a	89.73 pF	-26.02 pF	-16.38 pF
b	-106.76 pF	242.86 pF	-104.46 pF	b	-26.02 pF	89.32 pF	-13.81 pF
c	-92.46 pF	-104.46 pF	206.1 pF	c	-16.38 pF	-13.81 pF	72.53 pF

c) Tx/Rx Mutual Capacitances			
	a	b	c
a	-9.85 pF	-5.22 pF	-7.78 pF
b	-7.82 pF	-7.57 pF	-7.42 pF
c	-4.06 pF	-3.03 pF	-7.7 pF

The self-inductance matrices from the system Q3D simulation are shown in Table 5.5, which are the self-inductances of the combined transmitter/receiver and compensation circuit inductors. Although the system self-inductances are not particularly helpful for evaluating the proposed system layout, the mutual inductances can be used to verify the expected transmitter/receiver coupling. The mutual inductance values are listed in Table 5.6 for both the system Q3D simulation and the BEM approach used in the optimization. It is seen that the mutual inductance is hardly affected by the system layout since the system mutual inductance is very similar to the predicted isolated transmitter/receiver mutual inductance. One reason for this is the placement of the receiver side compensation inductors, which are placed above the receiver core. This helps to separate the receiver side inductor and connection conductors from the transmitter conductors, thereby reducing any large changes in coupling.

Table 5.5: DWPT System Self-Inductance Matrices

a) Tx Side Inductances				b) Rx Side Inductances			
	a	b	c		a	b	c
a	20.622 μ H	0.852 μ H	0.111 μ H	a	12.413 μ H	0.470 μ H	-0.647 μ H
b	0.852 μ H	21.188 μ H	2.255 μ H	b	0.470 μ H	11.805 μ H	-0.315 μ H
c	0.111 μ H	2.255 μ H	21.782 μ H	c	-0.647 μ H	-0.315 μ H	9.894 μ H

Table 5.6: DWPT System Mutual Inductance Comparison

a) Q3D Values				b) BEM Values			
	a	b	c		a	b	c
a	2.011 μH	-0.695 μH	-0.626 μH	a	2.058 μH	-0.849 μH	-0.848 μH
b	-1.010 μH	2.231 μH	-0.718 μH	b	-1.033 μH	2.203 μH	-0.858 μH
c	-1.187 μH	-0.788 μH	2.174 μH	c	-1.032 μH	-0.858 μH	2.203 μH

5.1.2 Isolated Transmitter and Receiver Simulation

To verify the transmitter and receiver inductances, a Q3D simulation of the isolated transmitter and receiver are utilized based on the model in Fig. 5.7. The additional connections are not included in the isolated model which allows the transmitter/receiver to be evaluated directly.

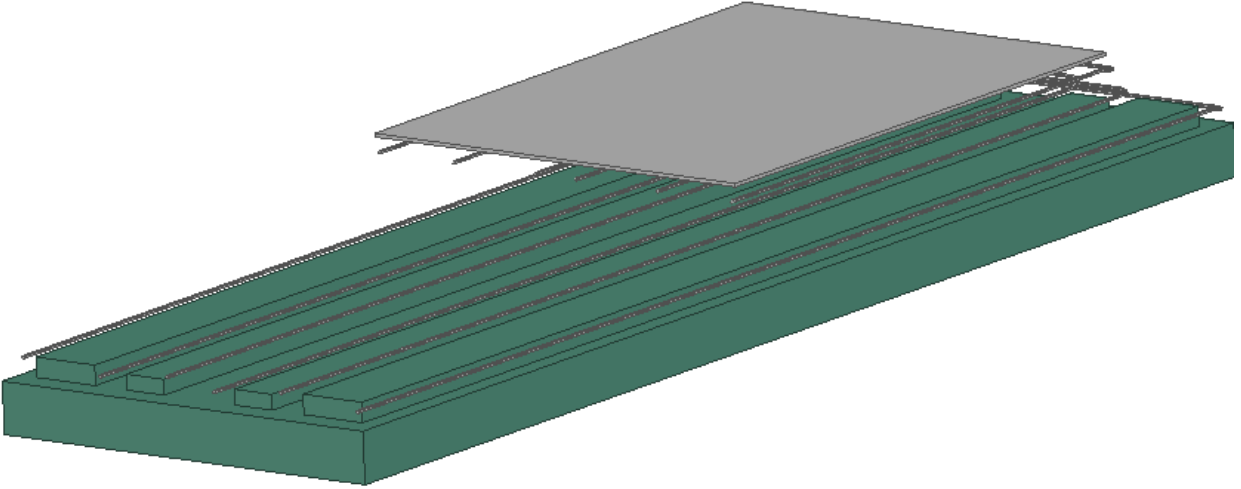


Figure 5.7: Q3D Model of Isolated Transmitter and Receiver

Compared to the BEM model of the optimization, the only noticeable changes to the transmitter and receiver are the end turns and the additional portion of the transmitter core that sits below the end turns. Fig. 5.8 provides a closer look at these characteristics in the Q3D model. The extra transmitter portion here extends only as far as the end turn, which is dictated by the minimum wire bend radius.

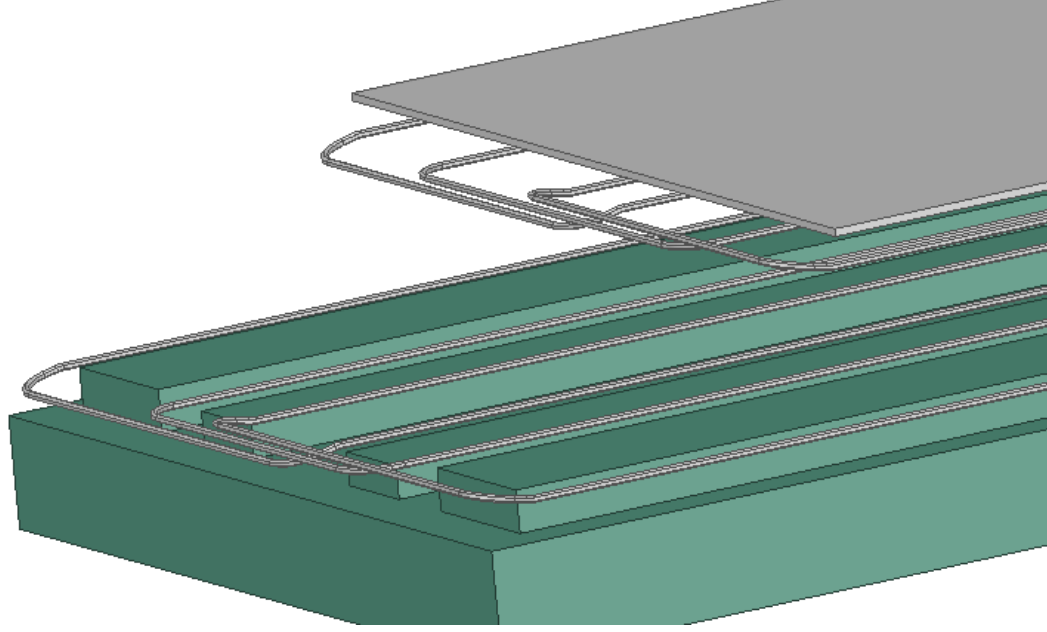


Figure 5.8: Transmitter and Receiver End Turns

The inductance results from this simulation can be directly compared to the values from the optimization. The transmitter self-inductance matrices are shown in Tables 5.7a and 5.7b, where it is seen that the Q3D simulation values slightly overestimate the BEM values, although they are very similar. The difference is more significant in the non-diagonal terms, but because these terms are smaller than the diagonal terms, this does not affect the effective inductance heavily. The receiver self-inductance matrices are shown in Tables 5.8a and 5.8b, and the mutual inductance terms in Tables 5.9a and 5.9b, where similar observations are made.

Table 5.7: Transmitter Self-Inductance Comparison

a) Q3D Values				b) BEM Values			
	a	b	c		a	b	c
a	11.786 μH	-2.208 μH	-2.249 μH	a	11.388 μH	-2.022 μH	-2.021 μH
b	-2.2077 μH	11.637 μH	-1.327 μH	b	-2.022 μH	11.112 μH	-1.452 μH
c	-2.2486 μH	-1.327 μH	11.638 μH	c	-2.021 μH	-1.452 μH	11.113 μH

Table 5.8: Receiver Self-Inductance Comparison

a) Q3D Values				b) BEM Values			
	a	b	c		a	b	c
a	5.634 μH	-1.270 μH	-1.341 μH	a	5.510 μH	-1.045 μH	-1.044 μH
b	-1.270 μH	5.515 μH	-0.857 μH	b	-1.045 μH	5.276 μH	-1.171 μH
c	-1.341 μH	-0.857 μH	5.350 μH	c	-1.044 μH	-1.171 μH	5.275 μH

Table 5.9: Mutual Inductance Comparison

a) Q3D Values				b) BEM Values			
	a	b	c		a	b	c
a	2.063 μH	-0.909 μH	-0.907 μH	a	2.058 μH	-0.849 μH	-0.848 μH
b	-1.065 μH	2.273 μH	-0.697 μH	b	-1.033 μH	2.203 μH	-0.858 μH
c	-1.125 μH	-0.770 μH	2.200 μH	c	-1.032 μH	-0.858 μH	2.203 μH

Because the effective inductance, which is described in Section 2, is used to determine the compensation circuit parameters and resulting system performance, these values must also be considered when evaluating the system. The effective inductance values are listed in Table 5.10 for the Q3D and BEM methods. As seen with the inductance matrices, the effective inductance values are very close, with slightly higher values from the Q3D simulation, and the difference between the two is below 5% for all effective values.

Table 5.10: Effective Inductance Comparison

	Q3D	BEM	Percent Difference
$L_{tx,eff}$	13.611 μH	13.036 μH	4.44%
$L_{rx,eff}$	6.656 μH	6.440 μH	3.35%
$L_{m,eff}$	3.091 μH	3.068 μH	0.77%

5.1.3 Simulation of Transmitter and Receiver with Terminal Connections

In addition to the isolated transmitter and receiver models, it is important to evaluate a model that includes the terminal connections. Although the results of the isolated model represent the predicted inductances in the optimization well, there is an inherent increase in inductance from

the terminals, especially for the transmitter in this layout. The model used in the following evaluation is depicted in Fig. 5.9, where the terminals connect from the transmitter or receiver to the respective capacitor enclosure locations.

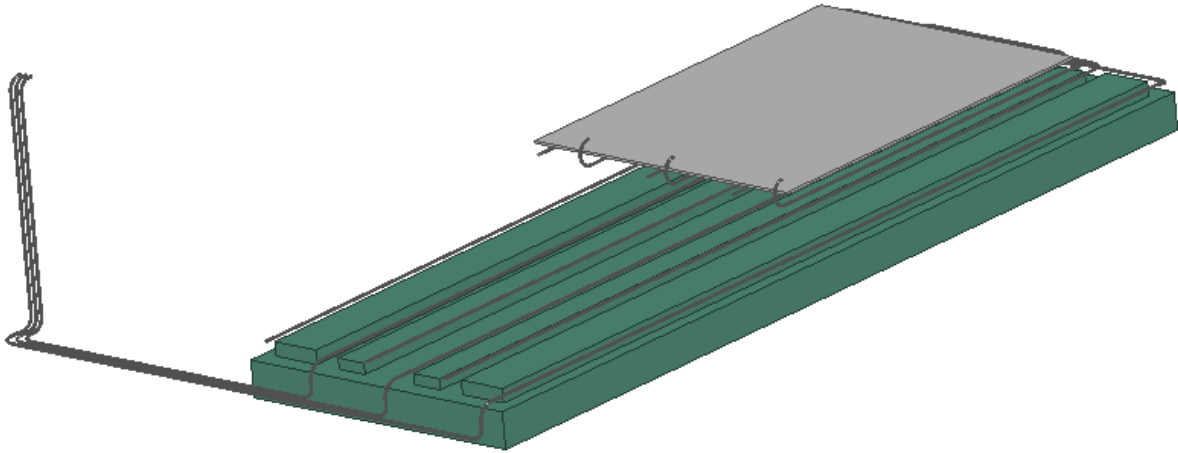


Figure 5.9: Q3D Model of Transmitter and Receiver with Terminals

The inductance matrices from the Q3D simulation are compared to the BEM inductance matrices from the optimization in the following tables. With the most noticeable increase, the transmitter self-inductance matrices are shown in Tables 5.11a and 5.11b. This is expected due to the longer connecting conductors between the transmitter and compensation circuit. For the receiver self-inductance matrices, shown in Tables 5.12a and 5.12b, there is a minimal change from the isolated model, and the Q3D simulation values are still relatively close to the BEM values. The same is true for the mutual inductance matrices, which are shown in Tables 5.13a and 5.13b. This is not surprising since the lack of change in the mutual inductance values was also noted in the system Q3D simulation.

Table 5.11: Transmitter Self-Inductance Comparison with Connections

a) Q3D Values				b) BEM Values			
	a	b	c		a	b	c
a	14.701 μH	-0.298 μH	-0.708 μH	a	11.388 μH	-2.022 μH	-2.021 μH
b	-0.298 μH	15.134 μH	0.961 μH	b	-2.022 μH	11.112 μH	-1.452 μH
c	-0.708 μH	0.961 μH	15.815 μH	c	-2.021 μH	-1.452 μH	11.113 μH

Table 5.12: Receiver Self-Inductance Comparison with Connections

a) Q3D Values				b) BEM Values			
	a	b	C		a	b	c
a	5.612 μH	-1.273 μH	-1.339 μH	a	5.510 μH	-1.045 μH	-1.044 μH
b	-1.273 μH	5.503 μH	-0.847 μH	b	-1.045 μH	5.276 μH	-1.171 μH
c	-1.339 μH	-0.847 μH	5.341 μH	c	-1.044 μH	-1.171 μH	5.275 μH

Table 5.13: Mutual Inductance Comparison with Connections

a) Q3D Values				b) BEM Values			
	a	b	c		a	b	c
a	2.086 μH	-0.923 μH	-0.927 μH	a	2.058 μH	-0.849 μH	-0.848 μH
b	-1.035 μH	2.251 μH	-0.716 μH	b	-1.033 μH	2.203 μH	-0.858 μH
c	-1.086 μH	-0.791 μH	2.166 μH	c	-1.032 μH	-0.858 μH	2.203 μH

The effective inductance values are also compared with the terminal connections added. These values are listed in Table 5.14, where the receiver and mutual inductances are still within 5% of the optimization values, but the transmitter inductance is much further away. The compensation circuit component values can also be recomputed for these transmitter and receiver inductances. Keeping the inverter and rectifier voltages and the transmitter current the same, the recomputed compensation circuit values are compared to the original values in Table 5.15. There is no change needed in most of the components, but C_1 and C_2 are both adjusted by around 0.4 μF , which would require replacing the capacitors.

Table 5.14: Effective Inductance Comparison

	Q3D	BEM	Percent Difference
L_{tx}	15.232 μH	13.036 μH	16.84%
L_{rx}	6.638 μH	6.440 μH	3.08%
L_m	3.081 μH	3.068 μH	0.43%

Table 5.15: Adjusted Compensation Circuit Component Values

	Adjusted	Original	Percent Change
L_{f1}	3.763 μH	3.763 μH	0.00%
C_{f1}	4.207 μF	4.207 μF	0.00%
C_1	1.380 μF	1.7073 μF	19.15%
C_2	5.537 μF	5.917 μF	6.36%
C_{f2}	4.189 μF	4.207 μF	0%
L_{f2}	3.779 μH	3.763 μH	0.43%

While changing the values of compensation circuit components is one solution to dealing with the added inductance on the transmitter, there are a variety of other ways to address the issue. A simple alternative would be to move the compensation circuit components closer to the transmitter; however, there are likely objections to doing this for a roadway implementation. Another possible avenue is to optimize DWPT system designs where the transmitter inductance includes calculations for extra terminal wire.

5.1.4 Inductor Simulation

The final section of the system simulation is the compensation circuit inductors, which are evaluated through the Q3D model depicted in Fig. 5.10. The presence of the transmitter and receiver cores is preserved to observe any effects on the compensation circuit inductances.

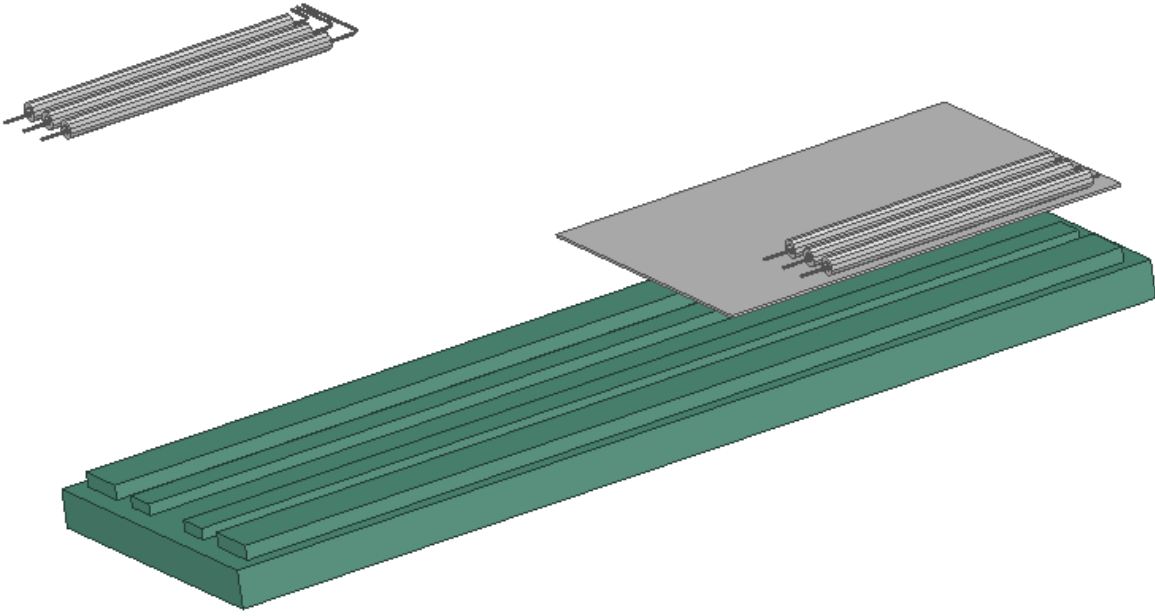


Figure 5.10: Q3D Model of Compensation Inductors

The inductance matrices for L_{f1} and L_{f2} from the Q3D simulations are shown in Tables 5.16a and 5.16b. Since the compensation circuit assumes balanced and non-coupled inductors, it is not immediately obvious if unbalanced values or coupling between the inductors will have a noticeable impact on the operation of the DWPT system. Attempting to equate the effective inductance values may mitigate any undesirable effects, though. The effective L_{f1} and L_{f2} are compared to the values from the optimization in Table 5.17. The Q3D values are significantly larger than the values from the system optimization.

Table 5.16: Compensation Inductor Inductance Matrices

a) L_{f1} Values

	a	b	c
a	5.320 μH	0.690 μH	0.412 μH
b	0.690 μH	5.166 μH	0.593 μH
c	0.412 μH	0.593 μH	5.004 μH

b) L_{f2} Values

	a	B	c
a	5.189 μH	0.802 μH	0.485 μH
b	0.802 μH	5.150 μH	0.679 μH
c	0.485 μH	0.679 μH	4.949 μH

Table 5.17: Effective Inductance Comparison

	Q3D	Optimization	Percent Difference
L_{f1}	4.596 μH	3.763 μH	22.13%
L_{f2}	4.441 μH	3.763 μH	18.01%

While it was more complicated to adjust the inductance increase in the transmitter, a more direct approach that is used for the inductors. By reducing the lengths of the inductors by the appropriate amount, the effective inductances of L_{f1} and L_{f2} can be adjusted towards the expected values. To determine the length to remove, the following equation is used:

$$l_{sub} = \frac{(L_{i,eff} - L_{exp})}{L_{exp}} l_0 \quad (5.1)$$

where $L_{i,eff}$ is the effective inductance from the Q3D simulation, L_{exp} is the expected inductance value, and l_0 is the original inductor length. The adjusted inductance matrix can be assumed to be the following:

$$\mathbf{L}_{adj} = \mathbf{L}_i - \mathbf{I} \cdot (L_{i,eff} - L_{exp}) \quad (5.2)$$

where \mathbf{L}_i is inductance matrix retrieved from the Q3D simulation.

Through these calculations, the adjusted inductance matrix is determined for L_{f2} and L_{f2} in Tables 5.18a and 5.18b. The effective inductance of the adjusted values is also calculated through (2.10) and shown in Table 5.19, where it can be seen that the effective inductance matches the expected inductance of the compensation circuit.

Table 5.18: Adjusted Inductance Matrices

a) L_{f1} Values				a) L_{f2} Values			
	a	b	c		a	b	c
a	4.487 μH	0.690 μH	0.412 μH	a	4.512 μH	0.802 μH	0.485 μH
b	0.690 μH	4.334 μH	0.593 μH	b	0.802 μH	4.473 μH	0.679 μH
c	0.412 μH	0.593 μH	4.172 μH	c	0.485 μH	0.679 μH	4.272 μH

Table 5.19: Adjusted Effective Inductance

	Q3D	Optimization	Percent Difference
$L_{f1,eff}$	3.763 μ H	3.763 μ H	0%
$L_{f2,eff}$	3.763 μ H	3.763 μ H	0%

6. CONCLUSION

This work proposes various models to be used within optimization of DWPT system. The design of AC inductors in the compensation circuit is presented, with derivations for the loss, volume, and mass. A model for the capacitor is also developed that capitalizes on high-power polypropylene capacitors to reduce loss and size. Furthermore, thermal models for single- and three-phase transmitter topologies are established through a TEC-based approach and validated through steady-state thermal FEA simulations. Incorporating these models, a system-level multi-objective optimization process is outlined and demonstrated, wherein comparisons of DWPT systems with Magment and non-magnetic transmitter cores as well as with 26 cm and 18 cm gaps are discussed in detail and dissected for all system components. These comparison studies can be used to inform design choices for potential DWPT systems. As a step to validate the DWPT system design, electromagnetic FEM/BEM simulations of the expected layout of the system in the laboratory are created. Methods for adjusting the system components are suggested in consideration of inductance increases caused by added connections between components.

Building on this work, further studies can be performed to assess the benefits and shortcomings of additional core materials, different transmitter and receiver topologies, different compensation circuit topologies, and variations in many other design characteristics. Adding objectives to the optimization is also a possible improvement. A cost model for each component could be developed, as seen in [4], to allow minimization of system cost, and an objective for stray magnetic field, as seen in [1]-[3] is also being developed for future optimizations. It is noted that it may be more difficult to reduce the stray field in high-power DWPT systems such as this, in contrast to the comparatively lower power levels of [1]-[4]. Considerations for lateral misalignment such as in [2] and [4] may be incorporated into the optimization in updated iterations, which is another factor that impacts the realistic feasibility of these systems. Finally, validation and testing of a physical DWPT system prototype is a critical effort that will be fulfilled in the future and will potentially open the door to a large-scale implementation of the proposed DWPT system.

REFERENCES

- [1] R. Bosshard and J. W. Kolar, "Multi-Objective Optimization of 50 kW/85 kHz IPT System for Public Transport," *IEEE Journal of Emerging and Selected Topics in Power Electronics*, vol. 4, no. 4, pp. 1370-1382, December 2016.
- [2] S. Bandyopadhyay, P. Venugopal, J. Dong and P. Bau, "Comparison of Magnetic Couplers for IPT-Based EV Charging Using Multi-Objective Optimization," *IEEE Transactions on Vehicular Technology*, vol. 68, no. 6, pp. 5416-5429, June 2019.
- [3] Z. Luo, X. Wei, M. G. S. Pearce and G. A. Covic, "Multiobjective Optimization of Inductive Power Transfer Double-D Pads for Electric Vehicles," *IEEE Transactions on Power Electronics*, vol. 36, no. 5, pp. 5135-5146, May 2021.
- [4] R. Tavakoli, E. M. Dede, C. Chou and Z. Pantic, "Cost-Efficiency Optimization of Ground Assemblies for Dynamic Wireless Charging of Electric Vehicles," *IEEE Transactions on Transportation Electrification*.
- [5] D. Aliprantis and A. D. Brovont, (*personal communication*) *Design of three-phase transmitter and its optimization*.
- [6] S. Li, W. Li, J. Deng, T. D. Nguyen and C. C. Mi, "A Double-Sided LCC Compensation Network and its Tuning Method for Wireless Power Transfer," *IEEE Transactions on Vehicular Technology*, vol. 64, no. 6, pp. 2261-2273, June 2015.
- [7] A. Prasad, *Multi-Objective Design of Dynamic Wireless Charging Systems for Heavy-Duty Vehicles*, 2020.
- [8] "Magnetic Concrete MC," [Online]. Available: <https://www.magment.de/en-magneticconcrete-mc>.
- [9] A. D. Brovont, "Exploring the boundary element method for optimization-based machine design," *2017 IEEE International Electric Machines and Drives Conference (EIMDC)*, pp. 1-7, 2017.
- [10] "Round Litz," New England Wire Technologies, [Online]. Available: http://litzwire.com/nepdfs/Round_Litz_Catalog.pdf.

- [11] "Powder Cores," Magnetics, [Online]. Available: <https://www.mag-inc.com/Media/Magnetics/File-Library/Product%20Literature/Powder%20Core%20Literature/Magnetics-Powder-Core-Catalog-2020.pdf>.
- [12] S. D. Sudhoff, *Power Magnetic Devices: A Multi-objective Design Approach*, Hoboken, NJ: John Wiley & Sons, 2014.
- [13] ANSYS, Inc., *Maxwell Help Release 2021 R2*, 2021.
- [14] "CSP 405A," CELEM Power Capacitors, [Online]. Available: https://www.celem.com/csp_405a.
- [15] S. Pekarek, (*personal communication*) *Modeling of power electronic converters*.
- [16] S. D. Sudhoff, *Thermal Equivalent Circuit Toolbox Version 2.0 (TEC 2.0)*, 2013.
- [17] J. McGuinness, "Standard Specifications," Indiana Department of Transportation, 2020.
- [18] IES, "Thermal Conductivity, Specific Heat Capacity, and Density," IES, 2018. [Online]. Available: https://help.iesve.com/ve2018/table_6_thermal_conductivity__specific_heat_capacity_and_density.htm.
- [19] S. D. Sudhoff, *Genetic Optimization System Engineering Tool (GOSET) Version 2.6*, 2014.
- [20] D. Aliprantis, A. D. Brovont and S. Pekarek, (*personal communication*) *Development of DWPT optimization settings*.
- [21] ANSYS, Inc., *Q3D Extractor Help, Release 2021 R2*, 2021.